CARDIFF SCHOOL OF BIOSCIENCES

THESIS PRESENTED TO CARDIFF UNIVERSITY FOR THE DEGREE OF
DOCTOR OF PHILOSOPHY

Fabrication and Quantitative Correlative Light-Electron Microscopy of Novel Plasmonic Nanoparticles

Author: Yisu Wang

Supervisors: Prof. Paola Borri and Prof. Wolfgang Langbein

CARDIFF
UNIVERSITY
PRIFYSGOL
CAERDYDD

OCTOBER 2018

Declaration and Statements

DECLARATION

This work has not been submitted in substance for any other degree or award at this or any other university or place of learning, nor is being submitted concurrently in candidature for any degree or other award.

Signed ………………………………………… Date …………………………

STATEMENT 1

This thesis is being submitted in partial fulfillment of the requirements for the degree of PhD

Signed ………………………………………… Date …………………………

STATEMENT 2

This thesis is the result of my own independent work/investigation, except where otherwise stated.

Other sources are acknowledged by explicit references. The views expressed are my own.

Signed ………………………………………… Date …………………………

STATEMENT 3

I hereby give consent for my thesis, if accepted, to be available online in the University’s Open Access repository and for inter-library loans after expiry of a bar on access previously approved by the Academic Standards & Quality Committee.

Signed ………………………………………… Date …………………………

Contents

Chapter 1 Introduction 1

1.2. Single NP studies and Correlative imaging 6
  1.2.1 Single NP measurements 6
  1.2.2 Correlative imaging 9

1.3. Silver Nano Dimers 12
1.4. NP fabrication 16
  1.4.1 Nucleation and Seeds formation 17
  1.4.2 Crystal growth 18
  1.4.3 Plasmon-mediated fabrication 20

Chapter 2. Setups, Materials and Methods 26

2.1 Procedures 26
  2.1.1 Dimer fabrication 26
  2.1.2 Plasmon mediated fabrication 27
  2.1.3 Glass functionalisation 30
  2.1.4 TEM grid functionalisation 31
  2.1.5 NP immobilisation via drop casting 31
  2.1.6 NP immobilisation via Settlement 32
  2.2.1. The Inverted Microscope 35
  2.2.2 Cuvette-based spectroscopy 36
  2.2.3 Dark Field microscopy 36
  2.2.4 Micro-spectroscopy 37

2.3 Analysis Methods 39
  2.3.1 Wide field extinction analysis 39
  2.3.2 Optical cross-section calculation 40
  2.3.3 TEM Coordinate Mapping 42

Chapter 3. Correlative Imaging Method 45

3.1 Light - electron microscopy correlative imaging of single nanoparticles 45
  3.1.1 Mounting Medium 45
  3.1.2 Mounting Geometry 46
  3.1.3 Grid functionalisation and NP immobilisation 49

3.1.4 NP density. 53

Chapter 4. Silver Nanocubes: Results and discussion 56

4.1 Correlative imaging of Ag-cubes...56
4.2 Data analysis with computational modelling 65

Chapter 5. Plasmon Mediated Fabrication 67

5.1 Plasmon Mediated fabrication and purification 67
5.2 Statistical analysis of AgNP populations 72
5.2.1 Pentagonal projection / decahedron...72
5.2.2 Triangular projection / Tetrahedron 73
5.2.3 Kite projection / Bitetrahedron 74

5.3. Correlative imaging 77
5.3.1 Single silver decahedra...80
5.3.2 Single silver tetrahedra 83
5.3.3. Single silver bi-tetrahedra 85

Chapter 6. Silver dimers 89

6.1 Fabrication of AgNP in aqueous solution via PEG-dithiol...89
6.2 NP immobilisation via settlement 96
6.3 P1000DT mediated dimer formation, statistical analysis 98
6.4 Correlative imaging 103
6.5 Dimers in changing media 110

Conclusion 120

Reference 123

List of Abbreviations

3D: three dimension

Abs: absorption

AgNC: silver nano-cube

AgNP: silver nanoparticle

APTES: (3-aminopropyl)triethoxysilane

AuNP: gold nanoparticle

BF: bright field

BG: background

BSPP: bis (p-sulfonatophenyl) phenylphosphine

DDA: discrete dipole approximation

DF: dark field

Diam: diameter

EM: electron magnetic

fcc: face centreed cubic

FDTD: finite-difference time-domain

FEM: finite element method

FRET: Förster resonance energy transfer

FWM: four wave mixing

HR: high resolution

IR: infrared

IIT: Istituto Italiano di Tecnologia

LED: light emitting diode

LSPR: localised surface plasmon resonance

MNP: metallic nanoparticle

MW: molecular weight

NA: numerical aperture

NIR: near infra-red

NP: nanoparticle

OD: optical density

PEG: polyethylene glycol

PVP: polyvinylpyrrolidone

PxDT: PEG-dithiol, x is the average molecular weight

Rcf: relative centrifugal field

Sca: scattering

SERS: enhancement of spectroscopic signals

STEM: scanning transmission electron microscopy

TEM: transmission electron microscopy

UV-Vis: ultraviolet–visible

Abstract

Metallic nanoparticles (MNPs) are attracting increasing interest for many applications in photonics, ranging from optoelectronic devices to bioimaging and biosensing. An advantage of these systems is that their optical properties, governed by their localised surface plasmon resonance, are widely tunable via the nanoparticle shape and size, which can be controlled via e.g. colloid synthesis. In that context, it is important to develop accurate experimental methods able to correlate the size and shape of an individual single MNP, measured with nanometric precision, with its individual optical properties.

In this thesis, three different MNP systems, namely i) commercially-available Ag nanocubes of 75 nm edge; ii) Ag tetrahedra, bi-tetrahedra and decahedra in the 25 - 50 nm size range which was fabricated in-house using a plasmon-mediated photochemistry method; iii) Ag nanodimers was fabricated in-house via controlled self-assembly of polymer linkers onto commercial nominally spherical Ag nanoparticles of 40 nm diameter. Beyond fabrication, a substantial part of the work reported in this thesis describes the experimental protocol for correlative optical and transmission electron microscopy, which was developed and optimised, comprising reproducible deposition of these silver nanoparticles onto TEM grids, their optical characterisation via polarisation-resolved high-resolution dark-field and extinction micro-spectroscopy, and subsequent high-resolution TEM of the same particle. As proof-of-concept, the same Ag nanocubes of 75 nm edge were characterised optically in different dielectric environments, using solvents of different refractive index n; specifically, anisole (n=1.52), water (n=1.33), and air (n=1). The MNP scattering and extinction cross-section was determined in absolute units using an in-house developed quantitative measurement protocol, and the results are compared with numerical simulations using the measured geometry.

These studies pave the way toward an in depth understanding of the relationship between geometrical and optical properties of MNPs of non-trivial shapes, which in turn have the potential to be exploited in innovative bioimaging and biosensing platforms.

Acknowledgements

I owe a deep sense of gratitude to my supervisors, Professor Paola Borri and Professor Wolfgang Langbein, without whom I would not have the opportunity for this great journey of my life. They have spent a lot of their time and efforts to make my PhD a fruitful piece of work. On the way, I have learnt some much from them. Their extensive knowledge and passion for science have set up a goal that I hope to match someday.

During my PhD, I benefited from a great deal of assistance from members of the Cardiff Biophotonics group. In particular thanks to Dr. Attilio Zili for teaching me everything about spectroscopy, Optical physics in general as well as Italian cultures. Thanks to Dr. Lukas Payne, who gave me the best instructions on taking beautiful images with the microscopy and using his image analysis software extract data from those images. Thanks to Dr. Iestyn Pope for his helps with all sort of problems I had in the lab as well as for helping me to design and assemble the irradiation chamber.

I would like to thank our external collaborators: Dr. Iwan Moreels and Dr. Anatoliy Polovitsyn at the Istituto Italiano di Tecnologia for teaching me plasmon mediated fabrications. Dr. Thomas Davies for his valuable advises on using transmission electron microscope.

Finally, I want to thank my parents, whom have been extremely supportive of me throughout this entire process, I always hope to make them proud. I also want to thank my wife Ziqing for her love and support.

Outline

In **Chapter 1**, background concepts and a literature overview is provided for the field covered by the experimental works in this thesis. In particular, a number of relevant topics were discussed: i) the optical cross-section of metallic nanoparticles (MNPs); ii) how individual nanoparticles can be measured optically and with correlative electron microscopy imaging; iii) the optical properties of nano-dimers and specifically their longitudinal surface plasmon resonance; iv) an overview of silver nanoparticle (AgNP) fabrication methods.

In **Chapter 2**, the materials, procedures and experimental set-ups for this work are presented. Specifically, details are provided on i) the dimer fabrication protocol; ii) the plasmon mediated fabrication; iii) the chemical protocols to activate and functionalise glass surfaces and TEM grids; iv) the procedures followed to immobilise NPs onto the sample surface. A detailed description of the hardware and procedures used for the micro-spectroscopy experiments is also provided. The quantitative analysis methods are described, with explicit formula given.

In **Chapter 3**, experimental data shows how the AgNPs were evenly immobilised onto the TEM grid via a novel settlement technique; and how anisole can be used as mounting medium to image the sample grid in a homogenous optical environment, allowing for its removal not affecting the subsequent characterisation with TEM.

In **Chapter 4**, as proof-of-concept, the correlative imaging method described in chapter 3 is implemented to study commercially-available 75 nm edge size Ag nanocubes. Quantitative experimental and numerical data (modelled with COMSOL using the cube geometry from TEM data) of the same individual Ag-nanocube in air or anisole are compared.

In **Chapter 5**, experimental data shows how Ag tetrahedra, bi-tetrahedra, decahedra can be fabricated via a. Results of the correlative optical/TEM studies for those AgNPs are also presented.

In **Chapter 6**, a number of experiments were designed to show that polymer linkers can be used to fabricate Ag dimers with various interparticle distances in solution. It was demonstrated that despite the range of inter-particle distances available when the dimers are in the reaction solution, mostly dimers with small interparticle distances (2 nm) can be found upon deposition on the TEM grid. Finally, correlative optical/TEM studies of dimers with small interparticle distances are presented.

Chapter 1 Introduction

Metal nanostructures have been intensively studied because of their unique optical properties at nanoscale, which offers probing and detecting possibilities in wavelength specific bioimaging and biosensing (Jain et al. 2008). The optical properties of MNP, such as silver nanoparticles (AgNP), strongly depend on the morphology of the NP; for example, a few nanometres increase in the size of an AgNP will cause significant red-shift of its absorption peak. Over the past two and half decades, a host of colloid methods have been developed for fabrication of MNPs with various shapes, sizes and compositions, which provide the possibilities of tuning the optical properties of MNP for one's specific application. However, due to the stochastic nature of colloid chemistry, the products always have a shape/size distribution. Therefore, to truly understand how the shape and size of MNPs affect their optical properties, one has to study them at single NP level, which requires correlating the optical measurements with geometrical measurements of the same NP. The research vision of this PhD project was to i) developing a flexible correlative imaging technique to study various MNP in different dielectric environments at single NP level; ii) fabricating AgNP with different shapes and sizes as well as AgNP dimers with various interparticle distances; iii) charactering the structural and optical properties of the fabricated NPs with the correlative imaging techniques; along with quantitative spectroscopy and computational modelling (previously developed in our Lab by Dr. Attilio Zilli) to provide a thorough understanding of the relationship between geometrical and optical properties of MNPs of non-trivial shapes. One of the potential applications of this study is to be able to characterise MNP from colloid synthesis with simple optical measurements to complement expensive and time-consuming electron microscopy, which can be a valuable tool for the MNP fabrication industry.

1.1. Optical properties of MNPs

Nanoparticles (NPs) are objects that have sizes in all three dimensions (3D) significantly smaller than a micrometer, and thus they have typically sizes smaller than the wavelength λ of visible light. When light, i.e. electromagnetic radiation, interacts with a NP, it can be scattered (elastically or inelastically) as well as absorbed by the NP and converted into heat and luminescence. These processes can be quantitatively defined by an optical cross-section. The optical cross section (σ), in general, is defined as the area given by the ratio between the incident irradiation power (P) removed by the process considered and the incident intensity (I_i):

$$\sigma \equiv P / I_i. \quad \textbf{(1.1)}$$

For NPs where inelastic (e.g. Raman) scattering and fluorescence can be neglected, such as those discussed in this thesis, one can limit the discussion to the scattering (σ_{sca}) and the absorption (σ_{abs}) cross-sections. The sum of these two processes is defined as extinction (σ_{ext}), and quantifies the total power removed by the NP from the incident intensity:

$$\sigma_{ext} = \sigma_{sca} + \sigma_{abs.}, \quad \textbf{(1.2)}$$

For a small spherical NP, in the so-called Rayleigh limit (diameter D << λ), the NP can be considered as a point dipole. The dynamical response of NP to an external electromagnetic field is determined by the polarisability of the NP (α), which is the proportionality constant between incident electrical field and induced dipole. It is dependent on the relative permittivities of the NP ε_{NP} and the surrounding medium ε_m, as well as the shape and size of the NP. The relative permeability is assumed to be unity, which is a good approximation for most materials in the visible spectral range. The polarisability of a spherical NP with diameter D << λ is given by (Dienerowitz *et al*. 2008. Griffiths and Owen 1983):

$$\alpha = \frac{\pi}{2} D^3 \frac{\varepsilon_{NP} - \varepsilon_m}{\varepsilon_{NP} + 2\,\varepsilon_m}. \quad \textbf{(1.3)}$$

Notably, there is an exact solution of Maxwell’s equations for a spherical NP of arbitrary size in a homogeneous medium, known as Mie theory; when only including the dipolar term (known as dipole approximation) the analytic solution for the optical cross-sections of the NP can be expressed as (Mie 1908):

$$\sigma_{sca} = \frac{2\pi^5}{3} \frac{D^6}{\lambda^4} \left| \frac{\varepsilon_{NP} - \varepsilon_m}{\varepsilon_{NP} + 2\,\varepsilon_m} \right|^2 = \frac{k^4}{6\pi} |\alpha|^2. \quad \textbf{(1.4)}$$

$$\sigma_{abs} = \pi^2 \frac{D^3}{\lambda} \operatorname{Im} \left| \frac{\varepsilon_{NP} - \varepsilon_m}{\varepsilon_{NP} + 2\,\varepsilon_m} \right| = k \operatorname{Im} \alpha. \quad \textbf{(1.5)}$$

MNPs such as AgNPs and gold nanoparticles (AuNPs) have been intensively studied because of their unique optical properties. Metallic objects have a fraction of their electrons that can freely move around the positively charged lattice. The electromagnetic field (EM) of the light drives the free electrons of the MNPs to undergo a collective coherent oscillation around the positive metallic lattice (Kreibig, Hilger *et al*. 1996). This process is resonant at a particular frequency of the incident light, known as localised surface plasmon resonance (LSPR) oscillation (Willets and Van Duyne 2007), as a results of the feedback action from the field originating from the charge displacement at the NP edges. The LSPR is defined to be the frequency at which the polarisability and in turn the scattering cross section is maximum. At the LSPR there is a strong EM field around the NP. The LSPR oscillation decays radiatively or non-radiatively, which results in the scattering and absorption effects respectively (Jain *et al*. 2006).

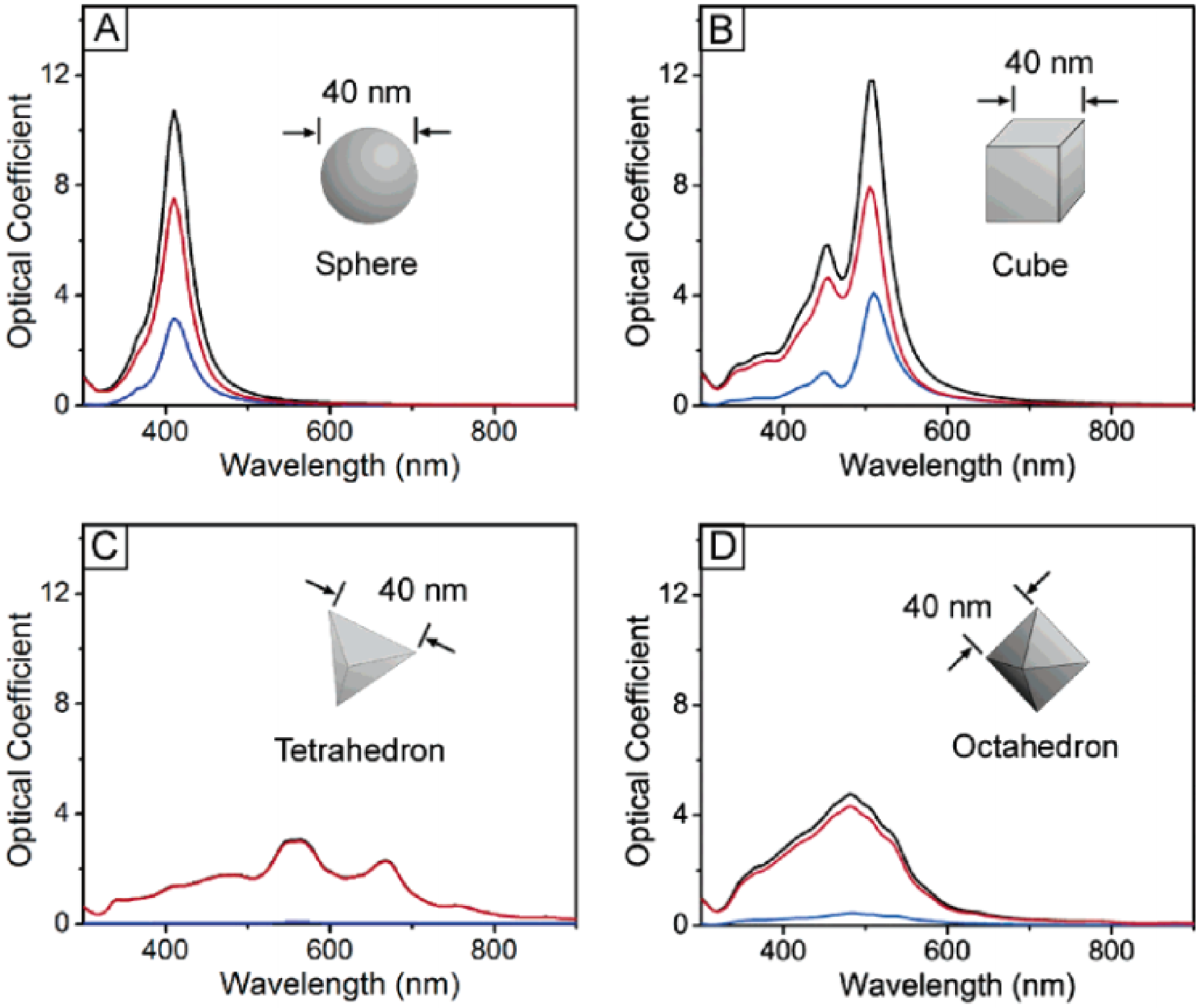

Figure 1.1 Calculated (DDA) absorption (red), extinction (black) and scattering (blue) spectra of 40 nm AgNP in water (n=1.33). Optical cross sections of the NP were calculated by divide by its geometrical cross-sectional area to give the dimensionless optical coefficients (**A**) spherical AgNP with isotropic shape has a single LSPR peak, AgNP with anisotropic shape such as cube (**B**) tetrahedron (**C**) and octahedron (**D**) have multiple, red-shifted LSPR peaks. Reproduced with permission from (Wiley *et al*. 2006) © 2006 American Chemical Society.

The shape, size, material of the MNP and its dielectric environment influence the LSPR peak position and the amplitude of the optical cross sections (Kreibig and Vollmer 1995). For example, eq. (**1.4**) and (**1.5**) show that the LSPR occurs when the denominator of α is minimum, namely for $\mathrm{Re}(\varepsilon_{NP}) = -2\varepsilon_m$, hence depending on the particle material permittivity and the dielectric constant of the environment. They also show that the absorption cross section scales with the NP volume (D^3) while the scattering cross section scales as D^6. How the NP shape influences the optical cross section is generally complicated (and beyond the spherical case in the dipole limit of eq. (**1.4**) and (**1.5**)). Its description requires to solve Maxwell's equations via EM simulations with computational tools. Notably, for the ellipsoid case in the dipole limit there is also an analytical formula of the NP polarisability (Ambjornsson *et al*. 2006), and in turn the optical cross sections, which links the ellipsoid geometry to the optical properties (Payne *et al*. 2015).

Both computational and experimental studies have demonstrated that the shape and structure of a AgNP determines the number of resonances (modes), the polarisation dependence, the spectral range and the intensity of the optical cross sections (Xiong *et al*. 2007a. Kottmann *et al*. 2001. El-Sayed 2001). A series of calculations using the discrete dipole approximation (DDA) (Laczik 1996. Wiley *et al*. 2006) (**Figure 1.1)** showed that, for a 40 nm size NP, which is beyond the dipole limit: i) the number of resonance frequencies exhibited by a NP is related to the symmetry of the nanostructure. For example, an isotropic sphere has optical-cross section spectra with a single resonance peak, whereas a cube has spectra with multiple red shifted resonance peaks; ii) The amplitude of the resonance peak depends on the symmetry of the nanoparticle. For example, MNPs with a cubic shape have corners on opposite sides of a line of symmetry, which will create a strong dipole and intense resonance peaks. MNPs with tetrahedral shape, on the other hand, have corners on opposite side of a face, which create a much weaker dipole and resonance peak; iii) Calculations of the relative field amplitude distribution around a triangular shaped particle showed that surface charges accumulate at sharp corners (Kottmann *et al*. 2001). Segregation of charges into corners is thought to increase charge separation, and in turn red-shift the resonance peak frequencies of the MNPs. This red-shift increases with increasing corner sharpness. For example, the tetrahedron has the more red-shifted resonance peaks than the cube and octahedron, because it has the sharpest corners. AgNPs with spherical (Pyatenko *et al*. 2007), tetrahedral (Zhou *et al*. 2008), cubic (Sun and Xia 2002) and octahedral (Gao *et al*. 2017) shape have been fabricated in large scale with colloid methods (**Section 1.4**). The spectra of the product solution (i.e. for a NP ensemble) in those reports qualitatively agreed with the calculated spectra in **Figure 1.1**. However, TEM/SEM micrographs presented in those report also showed NPs with irrelevant shapes and correlative studies at the individual NP level have not been reported with those shapes.

Both AuNP and AgNP have LSPR in the visible region of the light spectrum, which can be harnessed for various bio-imaging and bio-sensing application. AuNP is one of most widely used MNP for its optical properties, mainly because it can be fabricated easily with tuneable shape and size via colloid chemistry, and it is chemical inert and biocompatible. AgNP also has the fabrication advantage as AuNP; despite the fact that bare AgNP is less stable than bare AuNP, AgNP has a number of advantages over AuNP as a photonic tool: i) the onset of interband transitions from the d-band to the conduction band in gold is close to its LSPR frequency, which dampens the extinction cross-section and broadens the linewidth of its LSPR. Silver, on the other hand, does not have this interband absorption at the LSPR frequency, hence AgNP has stronger and sharper LSPR peak than that of AuNP; ii) The LSPR frequency of AgNP has greater dependence with its geometry than that of AuNP (van Dijk *et al* 2006, Gonzalez *et al.* 2014), this can be explained by Mie theory; iii) experimental data (Sonnichsen *et al*. 2005, Jain *et al*. 2007) have shown AgNP dimers has greater spectral changes than that of AuNP dimers per interparticle distance change, thus AgNP dimers provides more sensitivity as a plasmonic sensor, this is mainly because silver has greater permittivity than gold. In this thesis, the optical properties of AgNPs with various geometries such as nanospheres, nanodimers, nanocubes, nanoprisms were studied and their optical cross-section spectra were correlated with their geometrical parameters at the individual nanoparticle level. Although not investigated here, it should be mentioned that another method of tuning the LSPR is to use a metal nanoshell, namely a dielectric core with a metallic shell of nanometer thickness. By changing the shell thickness-to-core radius ratio, the LSPR of these NPs can be tuned over hundreds of nanometers in wavelength, across the visible and into NIR region of the spectrum (Oldenburg *et al*. 1998).

1.2. Single NP studies and Correlative imaging

The majority of MNPs used in bio-sensing and bio-imaging are fabricated by colloidal synthesis. The optical cross-sections of colloid synthesised MNPs are generally studied in an ensemble, most commonly by absorption spectroscopy of the colloidal solution. However, as discussed above, the plasmonic properties of MNPs are extremely sensitive to their size and shape; therefore, single particle spectroscopy techniques are needed to study how the LSPR of individual nanoparticles changes with small variations in their morphological features. Because there is always size and shape dispersion of the nanoparticles synthesised by colloid chemistry, an accurate correlation of the optical characteristics with the nanoparticle morphology can only be done at the single particle level (Slaughter *et al*. 2011).

1.2.1 Single NP measurements

Dark-field (DF) microscopy is a widely utilised technique for single NP micro-spectroscopy, because it is nominally background-free, offers high spatial resolution under a wide-field illumination, it is fairly simple to implement and is well suited to detect scattering from plasmonic MNPs. Various DF geometries have been devised. **Figure 1.2** shows the DF setup for all the DF imaging and scattering spectroscopy data obtained in my thesis. In general, a circular dark stop is placed in the back focal plane of the condenser lens, which blocks the centre part of the illumination so that a hollow cone of light illuminates the sample and the NPs are excited at a large incident angle using a high numerical aperture (NA) condenser lens. An objective lens with a lower NA is used, so that the excitation light transmitted unaltered by the sample is not transmitted through the objective. Only light scattered by the NP into the NA region of the objective is transmitted. Hence the resulting image has a dark background. When using white light illumination, individual MNPs scatter distinct colours depending on their LSPR, whereas dielectric debris and glass imperfections scatter rather independent of wavelength. Therefore, NPs can be identified as isolated coloured dots with dimensions given by the diffraction limit. For measuring the optical cross section spectra, typically the same microscope is coupled with a spectrometer and a charge coupled device (CCD) camera (Murphy and Davidson 2013) The scattered light collected by the objective is spectrally resolved by the spectrometer and recorded by the CCD camera. Notably, the absolute amplitude of σ_{sca} is difficult to obtain from these measurements. This is because the measured spectrum needs to be carefully normalised, according to the spectrum of the incident light. Moreover, one has also to account for the fact that only a fraction of the total scattering from NP is collected by the objective, which depends on the geometry and local environment of the NP, as well as on the angular ranges of detection and collection. Detailed calibrations are required for each specific excitation and collection geometry as well as for each type of NPs. A novel methodology (**Section 2.2.4**) has been developed by Dr. Attilio Zilli (Dr. Zilli PhD thesis and his unpublished work) in our host group which was applied in this work, and this allowed me to quantitatively determine the optical cross section of the imaged NP.

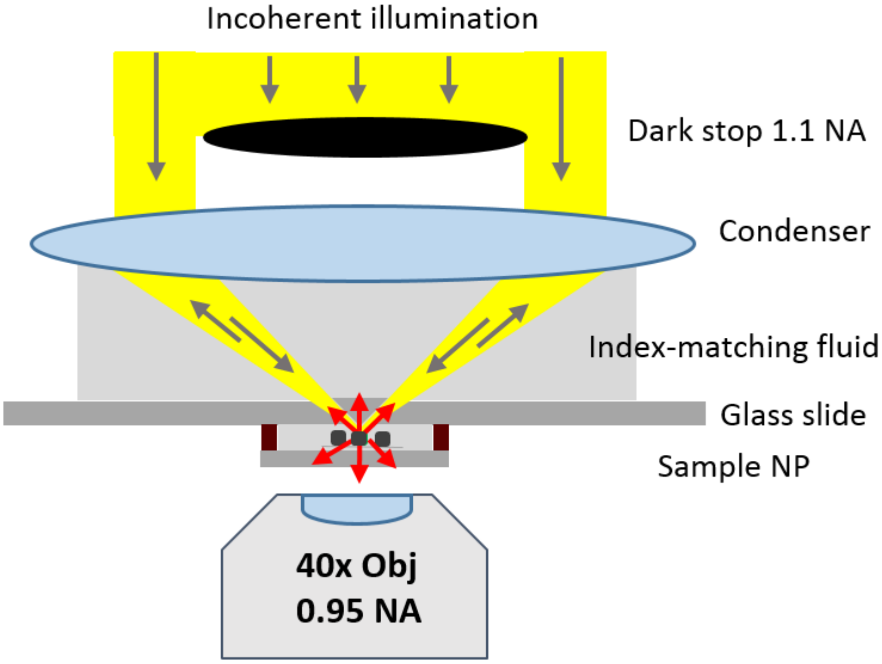

Figure 1.2: Schematic drawing of illumination and detection geometry we used for DF microscopy experiments with 40x objective. The grey arrows show the light path from the lamp, the red arrows show the scattered light from the NP.

For NPs with anisotropic shapes, different plasmon modes are typically polarised along specific directions of the NP which give rise to distinctive resonance peaks on the spectra of the NPs. In these cases, a polariser can be inserted either in the detection or excitation path of the DF microspectroscopy setup with a controllable polarisation angle. This allows the excitation/detection of individual plasmon modes of the NP as well as for probing the orientation of the NP on the substrate. For example, a 25 nm × 60 nm gold nanorod has a longitudinal plasmonic mode polarised along its long axis, which scatters red light at about 900 nm wavelength in water; and a transverse mode along its short axis, which scatters green light at about 600 nm. Sonnichsen and co-workers introduced a birefringent calcite crystal in the light path that can split 2 orthogonal polarisation directions for each Au nanorod into two spots on the same DF image. The scattering intensity (I_{sca}) of the Au nanorod in one particular polarisation direction is proportional to the square of the cosine of the angle θ between the rod and the polarisation direction. Thereby the orientation angle can be deduced backward from the measurement by $\theta = \sqrt{}$ [arccos(I_{sca})] (Sonnichsen and Alivisatos 2005). Polarisation resolved techniques were also used for studying nano-dimers (Rong *et al*. 2010), which have a similar polarisation response as a nanorod (more details in Chapter 6).

Bright-field (BF) imaging is another type of wide-field microscopy, where the transmitted or reflected light is directly collected (Murphy and Davidson 2013). Here, absorbing and/or scattering objects appear dark on a bright background. It can be used for measuring quantitatively the extinction cross section of microscopic objects (see for example Payne *et al*. 2018), as will be described also later in this thesis. Unlike DF microscopy, which is ultimately limited by the shot noise of the scattered light only, the detection limit of BF microscopy is limited by the shot noise of the transmitted light. In practice, however, the sensitivity of DF imaging is limited by the occurrence of a diffusive background due to other scatterers such as microscopic debris and the intrinsic roughness of the glass substrate. As a result, practical detection limits of MNPs in DF imaging on a clean glass surface are around D = 30 nm for gold spheres and D = 20 nm for silver spheres. Notably, since the scattering cross section scales as D^6 (see eq. (1.4)) the scattering contribution of small NPs becomes rapidly negligible compared to their absorption with decreasing size (van Dijk *et al* 2006). It is however also not trivial to measure small MNPs (e.g. AuNPs of less than 20 nm in size) via BF techniques.

All the MNP measured in this thesis have relatively large extinction cross section in the visible range, and we use the same optical set-up for both BF and DF imaging (except for different numerical aperture in illumination and detection). This allows us to easily find and align the NP of interest, and it is essential for our quantitative calculation of optical cross sections (**Section 2.2.4**). Notably, although not needed in this thesis, the technique used here can reach a detection sensitivity down to a single 2 nm AuNP, and could detect single 5 nm AuNPs in BF extinction (Payne *et al*. 2018).

1.2.2 Correlative imaging

The experimental data from single NP micro-spectroscopy are commonly interpreted with EM simulations using DDA (Laczik 1996), Finite-Difference Time-Domain (FDTD) (Taflove and Hagness 2005), or Finite Element Method (FEM) (Jin, 2002) methods. Due to the strong dependence of the optical properties on the size and shape, correlated structural information of the imaged MNPs is essential for meaningful numerical simulations. Transmission Electron Microscopy (TEM) is a standard technique for measuring the geometrical information of the individual MNP on a solid substrate with high resolution; sample NPs have be immobilised onto a substrate for TEM (usually a TEM sample grid with supporting non-absorbing film). TEM has stringent requirements concerning sample preparation. Optical measurements such as stimulated Raman scattering (Lombardi *et al*. 2012) and micro-spectroscopy, on the other hand, are easier to perform, and measurements with those techniques can be designed to adapt to the sample requirement for TEM; they can be carried out either before or after TEM.

A straightforward approach reported recently (Payne *et al*. 2015) consists of the following steps. 1) The sample is prepared on a TEM grid, usually by drop-casting; 2) images of the NPs of interest are acquired by an electron microscope; 3) the sample grid is retrieved after TEM measurement and subsequently mounted in a suitable medium (e.g. silicone oil) for optical measurements under a microscope. This approach allows one to directly select the shape/size/morphology of the NP of interest via the initial TEM analysis. Moreover, one can select NPs in regions with distinguishable morphological features/patterns (e.g. close to a number of other NPs), such that the imaged NPs can then be found easily under the optical microscope. Furthermore, this approach does not impose specific requirements on how the sample grid shall be mounted for the optical measurements. However, the issue with this approach is that for TEM, in order to achieve high spatial resolution and desirable signal-to-noise ratio, a high electron current density over the sample grid has to be applied during image acquisition, which leads to damage on the imaged NP as well as the surrounding substrate (**Figure 1.3**). This damage can significantly change the optical properties of the NP of interest, and also hamper the optical measurements; moreover, the damage is somewhat unpredictable. This becomes even more problematic when studying NPs with smaller size (Yang *et al*. 2008).

A)

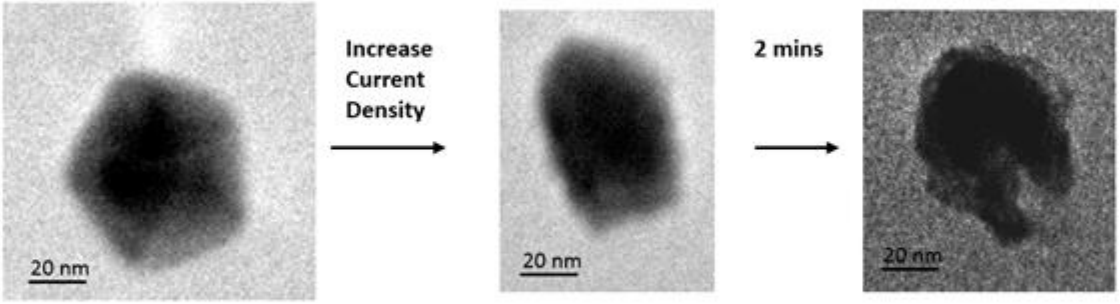

B) DF image before TEM DF image after TEM TEM

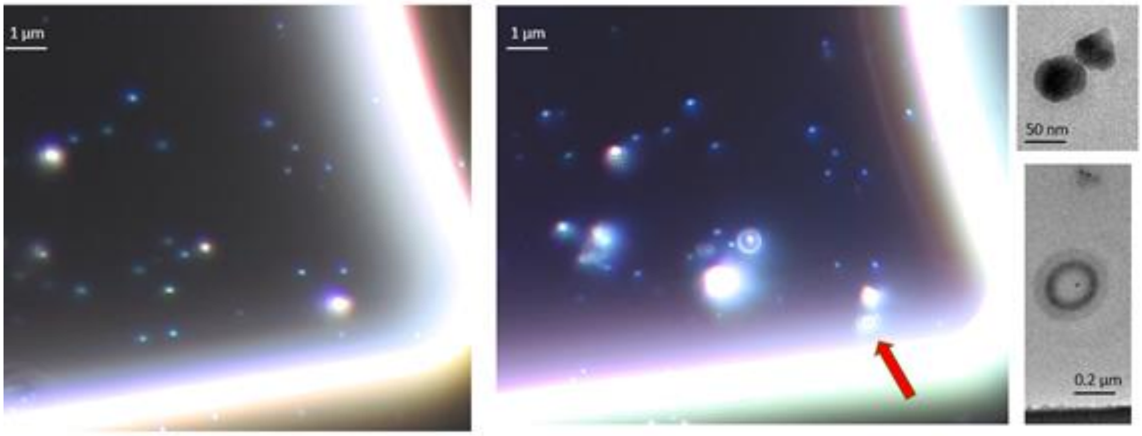

Figure 1.3 A) 50 nm edge size silver decahedrons were immobilised on the SiO_2 film via settlement (**Section 2.1.6**). The imaged NP had drastic morphological changes after the current density was increased from 40 pA/cm^2 to 60 pA/cm^2 (accelerating voltage 200 kV, beam current 101 μA) for 2 mins. **B)** Ag dimers (Ag-P1000DT, see **Chapter 6**) were immobilised on the SiO_2 film via drop-casting. After acquiring high resolution TEM imaging over the dimers, a near circular burn mark was visible in a low magnification TEM image of the same area (**right**). The burn mark was also visible on the DF image of the sample area as increased scattering (**left and mid**).

Alternatively, a commonly used approach (Davletshin *et al*. 2012a) is to carry out the optical measurements first, followed by TEM imaging; effectively swap the step 3 with step 2 of the procedure described above. This approach allows one to study the optical properties of undamaged NPs. However, TEM requires the imaged region on the sample grid to be extremely thin (< 200 nm) so that the electron beam can be transmitted without using high current density. Commercially available standard TEM grids are coated with either a carbon or silicon film as the substrate, usually below 50 nm in thickness; the substrates are extremely fragile. For this correlative approach to work, the sample grid has to be retrieved after optical measurements, and both the substrate and the NPs must stay intact for unambiguous correlation during TEM. This requirement limits how the sample can be mounted for optical measurements. For example, silicone oil (n = 1.52) is the most common mounting medium for refractive index matching during optical measurement. Silicone oil however is not compatible with this correlative approach because it was found to be impossible to completely remove the oil without damaging the TEM film and/or disturbing the NPs on the film; thick residual silicone oil coating on the NPs can absorb energy under the electron beam, and significantly affect the quality of the geometrical information obtained by high resolution TEM (HR-TEM). Another challenge for this approach is finding the same optically imaged NP with TEM. Most optical measurements require preparation of isolated NPs at relatively low density. NPs should be at least a few µm apart from each other to be well separated optically. Furthermore, since the TEM grid is very fragile, diluted MNPs in solution from colloid synthesis are directly deposited onto the substrate via drop-casting (instead of for example spin-coating), which usually concentrates NPs during drying (known coffee ring effect) and creates aggregates. Therefore, ultra-low concentrations are usually needed for drop-casting to avoid aggregations, and in turn result in a very low NP density on the substrate. As a drawback, these very low densities make it difficult to use the distribution patterns of neighboring NPs to confirm NP recognition for correlative imaging. This is further complicated by the fact that HR-TEM has a small field of view (a few µm^2 area) when imaging small NPs. Alternatively, instead of relying on NP pattern distribution, TEM grids with finder patterns are commercially available, for example a mesh can be mechanically produced on a copper grid with window size as small as 37 µm x 37 µm. However, the edges of the finder structure act as strong scatterers and limit the areas that can be imaged optically on the substrate (Nehl *et al*. 2004), especially for quantitative measurements. To overcome this problem, electron beam or photo lithography was used to etch small patterns (100 nm dots form various patterns) on a thin layer of chromium spin-coated on a silica substrate, which is visible with both DF imaging and TEM (Jin *et al*. 2005. Song *et al*. 2011). However, these marked grids are not available commercially and lithography is expensive and requires expertise (e.g. preparing the template for the etching patterns).

In this thesis, we report a novel correlative imaging technique based on carrying out the optical measurements first, followed by TEM imaging. We have developed a method which allows MNPs to be evenly distributed onto a common TEM grid with controlled density. The sample grid can be imaged in an index-matched environment and then safely retrieved and remains clean for HR-TEM.

1.3. Silver Nano Dimers

When two MNPs are in close proximity, a near field coupling occurs: the EM field near one nanoparticle is influenced by that of the neighbouring particle. The resulting EM field in the gap region is strongly enhanced (known as hotspot) (Petryayeva and Krull 2011). Moreover, the plasmon resonance frequency of the MNP pair is affected by this coupling, which red-shifts the frequency depending on the gap size between the MNPs (Nordlander *et al*. 2004).

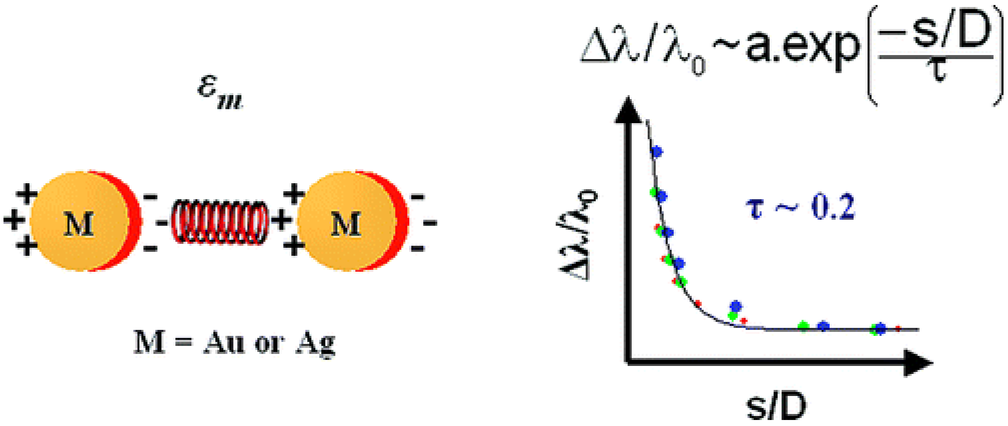

Figure 1.4 Near field coupling in MNP Pairs. **Left:** Illustration of the coupling effect of two MNPs in close proximity. The yellow circles represent the MNPs, and the red circles (behind the yellow circle) represent the NP electron clouds. The coupling between the particles acts to decrease the restoring force from the charge displacement, resulting in the red-shift of the LSPR. **Right:** nano-ruler equation used, and fit to the measured data: the fractional plasmon wavelength red-shift Dl/l_0 for light polarisation along the interparticle axis decays with the interparticle distance s, plotted as a normalised value relative to the NP diameter D. Reproduced with permission from (Jain *et al*. 2007) © 2007 American Chemical Society.

An array of Au nanodiscs (diameter of 88 nm and thickness of 25 nm) dimers with various interparticle distance was fabricated by electron lithography (Jain *et al*. 2007), Jain and coworkers systematically calibrated the plasmon shift of the dimers as a function of the interparticle distance. Two different polarisation directions of the incident light were used for microspectroscopy on individual dimers, i.e., one parallel to the interparticle axis of the dimer (referred as longitudinal polarisation) and the other perpendicular to the axis (referred as transverse polarisation), in order to investigate the LSPR mode of the dimers along the corresponding axis respectively. Under longitudinal polarisation, there is a very significant red-shift of the LSPR frequency as the interparticle distance decreases. Under transverse polarisation, in contrast, the LSPR frequency weakly blue-shifts with decreasing interparticle distance. A simple dipole-dipole coupling model was proposed for explaining the polarisation dependence (**Figure 1.4 left**). Under longitudinal polarisation, the dipole-dipole interaction is attractive, which results in the reduction of the resonance frequency of plasmon, while under transverse polarisation, this interaction is repulsive, and lead to an increase in the resonance frequency. Since the longitudinal mode of the LSPR is much more pronounced on the spectra of the dimers, longitudinal polarisation is generally used for studies the optical properties of dimers. Micro-absorption spectra of the Au dimer with various interparticle distance (gap s = 212, 27, 17, 12, 7, and 2 nm) showed a decay of the plasmonic shift of the longitudinal mode with interparticle distance, which was empirically described as an exponential decay, called ‘’plasmon ruler equation’’ (**Figure 1.4 right**). The discrete dipole approximation (DDA) method (Draine and Flatau 1994) was used to simulate the LSPR spectra of the Au nanodisc dimers, which agreed with the experimental data, and the ‘’plasmon ruler equation’’. Notably, the exponential decay does not have the correct limiting behaviour expected from the dipole-dipole coupling model (Jain *et al*. 2007). The dipole-dipole interaction is more appropriately described by $(d/D)^{-3}$ where d is the centre-to-centre distance. This equation relates the potential due to the interparticle coupling, which is proportional to d^{-3} to that of the single NP restoring potential, proportional to the inverse NP volume ie $1/(D^3)$.

Similar studies were carried out on lithography fabricated array of Ag nanodiscs, which showed that the red-shifts of the LSPR frequency for these Ag dimers under longitudinal polarisation were much stronger than for Au nanodisc dimers with the same interparticle distances (Gunnarsson *et al*. 2005). Yang, Reinhard and co-worker fabricated spherical AgNPs dimers in aqueous solution (Yang *et al*. 2010). Two batches of 40 nm AgNPs were first coated separately by two types of thiol functionalised oligonucleotides each with a complementary sequence. The NPs were also passivated and stabilised by assembling a monolayer of short polyethylene glycol (PEG) molecules on the particle surface, mixed with a small percentage of biotinylated PEGs to enable efficient immobilisation on Neutravidin functionalised surfaces. DNA mediated self-assembly took place upon mixing those two batches of AgNPs. The dimers were isolated from other aggregates via gel-electrophoresis. The dimers were then drop-casted onto a Neutravidin functionalised TEM grid. The spectral response of individual dimers was measured by Rayleigh scattering micro-spectroscopy, and the structural information of the imaged dimers were obtained through HR-TEM. The correlative data of dimers with various interparticle distances showed that for dimers with larger interparticle distance (>2 nm), the plasmon resonance of the longitudinal mode (E_{res}) red-shifts continuously with decreasing centre-to-centre distance (L) until the L to diameter (D) ratio reaches a value of $L/D \approx 1.05$. Interestingly, for dimers with small interparticle distance (<2 nm), the slope of E_{res} (L/D) levels off, and E_{res} become broadly distributed. This can be explained by theoretical studies using the time dependent local density approximation (TDLDA), which showed that for a metallic dimer with interparticle distance below 1 nm, quantum mechanical, effects such as electron tunneling across the dimer junction and screening greatly alter the optical properties and reduce the field enhancements relative to classical predictions (Zuloaga *et al*. 2009). By fitting these data, a plasmon ruler equation for DNA tethered AgNPs dimers was proposed:

$$E^{fit}_{res} = (2.77-457.36e^{-(L/D)k})\text{ eV. with } k = 0.16 \pm 0.03. \quad (\mathbf{1.6})$$

The analysis also showed that the dynamic range of $E_{res}(L/D)$ is larger for Ag than for Au dimers, (Reinhard *et al*. 2005) and that the Ag plasmon ruler has a greater sensitivity for detecting small distance changes. As already mentioned, however, the plasmon ruler equation is only an empirical formula; the observed data have a large variance around the fitted curve (Yang *et al*. 2010), which limits the application of this equation in quantitative measurements.

The near-field coupling of MNP pairs, sometime referred to as plasmon coupling phenomenon, has been exploited for biosensing. Sonnichsen and co-workers (Sonnichsen *et al*. 2005) using DF microscopy demonstrated that this effect can be used to monitor distances between single pairs of gold or silver nanoparticles that are linked via a single stranded DNA molecule (**Figure 1.5**). A single DNA hybridisation event caused stiffening of the linker DNA and thereby increased the interparticle distance of the dimer which was observed as colour change (blue-shift) of the scattered light from the dimer under DF illumination. Later on, a similar technique was used for ensemble kinetic measurements of the cleavage of DNA linker by the restriction enzyme EcoRV (Reinhard *et al*. 2007). 40 nm AuNP dimers linked a double strand DNA that contains a binding sequence for EcoRV were immobilised on a glass surface; only binding of the restriction enzyme to the specific sequence causes bending of the DNA linker before cleavage (Kostrewa and Winkler 1995) and decreases the interparticle distance of the dimers. This event can be monitored by the intensity of the scattered light from the dimer at its red-shifted frequency. Those binding events are transient (< 1 sec) and stochastic; they are hard to be captured with fluorescent techniques. Thanks to the scattering cross-section of the Au dimers, these experiments allowed 1,000 individual dsDNA enzyme substrates to be monitored simultaneously for hours with great temporal resolution (240 Hz). More recently, Rong, Reinhard and co-workers used polymer tethered Ag dimers as a probe in polarisation-resolved DF microscopy to monitor the spatial organisation of the plasma membrane of lysed HeLa cells: the translational and rotational motions as well as the extension of individual dimers diffusing on the plasma membrane causes the colour change of their scattered light as well as the change in polarisation angle of their longitudinal LSPR mode (Rong *et al*. 2010).

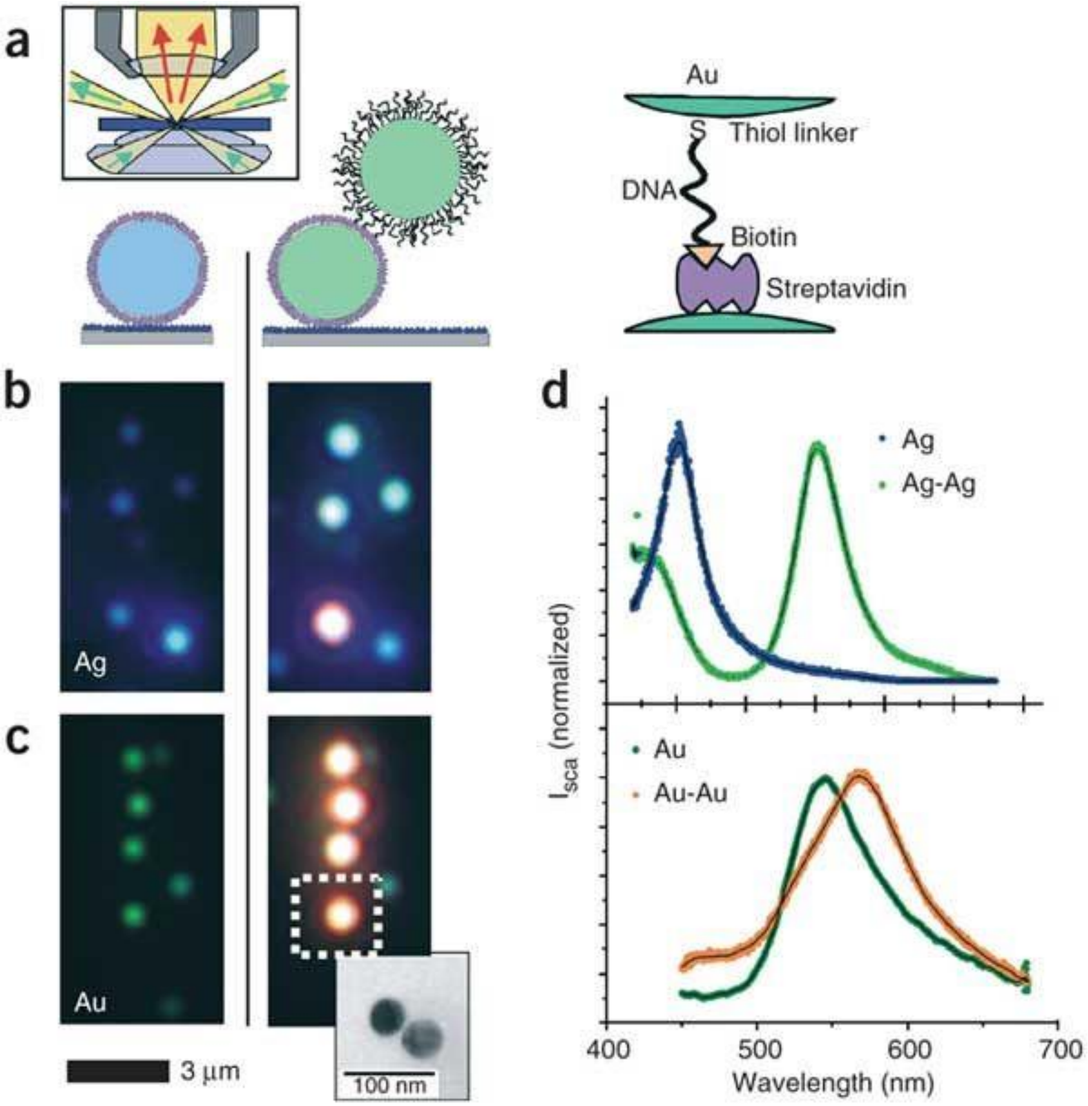

Figure 1.5 Molecular ruler based on plasmon coupling of AuNPs and AgNPs. **a**) The first MNP was immobilised onto a glass substrate via biotin-streptavidin binding (left), then, a second MNP is attached to the first particle (centre), again via biotin-streptavidin binding (right). The biotin on the second MNP is covalently bound to single strand DNA (ssDNA) via a thiol group at the 5' end. Inset: illustration of transmission DF microscopy. (**b**) Individual 40 nm AgNPs appear blue (left) and AgNPs dimer appear

blue-green (right). The orange dot in the bottom comes from an aggregate of more than two AgNPs. (**c**) Individual 40 nm AuNPs appears green (left), AuNP dimers appears orange (right). Inset: representative TEM micrograph of a dimer that cannot be separated optically. (**d**) Representative scattering spectra of single NPs and dimers for silver (top) and gold (bottom). AgNP dimers exhibit a larger red-shift (102 nm) than AuNP dimers (23 nm), stronger light scattering and a smaller plasmon line width. Reproduced with permission from (Sonnichsen *et al*. 2005) © 205 American Chemical Society

Plasmonic nanodimers offer several advantages over the current fluorescence based nano-scale distant sensing techniques such as Förster Resonance Energy Transfer (FRET) microscopy. For example a MNP is photo-stable and does not blink, which gives a more reliable readout. A plasmon ruler also offers a much larger distance range detection (up to 70 nm) than FRET (2-8 nm) (Weiss 1999). So far, the plasmon ruler concept has mostly been applied as a qualitative, rather than quantitative sensing tool. Notably, experimental measurements reported in the literature have focused on the LSPR frequency red-shift of the longitudinal mode upon dimer formation, and did not address the quantitative readout of the scattering and absorption cross-sections and their change with interparticle distance.

In this thesis (**Chapter 6**), Ag dimers were fabricated with various interparticle distances and used the in-house developed micro-spectroscopy extinction technique together with correlative TEM imaging to study the optical property of these Ag dimers, and in particular to provide a quantitative measure of their extinction cross-section.

1.4. NP fabrication

MNPs have been synthesised for more than 2000 years in different media such as stained glass and water. Over the past two and half decades, there has been enormous progress in the fabrication of AuNPs and AgNPs of various shapes and sizes. Two most common ways for fabricating MNPs are lithography and colloid synthesis. Lithography is a top-down approach, it begins with a pattern (e.g. array of discs or pyramids) generated on a larger scale (e.g. Ag or Au film with millimeters to micrometers thickness), then reduced to nanoscale via e.g. directed electron beam writing. Lithography allows precisely defining of the shape (resolution is limited to about 10 nm), size and position of MNPs on a solid-phase. However, it only can fabricate MNPs with very simple 3D shapes in extremely small scale (zeptomoles), this makes the products to have limited applications. Furthermore, the implementation of this technique is very expensive and complex (Corbierre *et al*. 2005). Colloid synthesis, on the other hand, is a bottom-up approach that starts with metal atoms and builds up to large nanostructures. This approach provides much more versatility; it has produced MNPs with a range of 3D structures from simple spherical shape to nanostar and core-shell structures with good size control.

Unlike organic synthesis, where countless possibilities of molecular structures can be designed and synthesised with a range of well-developed tools and methodologies, controlling the assemblies of metal atoms is still at an early stage of development. Fabrication of MNPs remains an art rather than a science as the detailed mechanisms of crystal evolution at atomic level during fabrication procedures are still not well understood, due to lack of experimental tools to capture and monitor individual crystal formation. For the last 30 years, a number of methodologies were developed empirically for fabricating monodisperse MNP samples with different shapes and sizes, and myriads of publications in recent years greatly helped us to gain some reasonable understanding on shape controlled synthesis of MNPs (Xia *et al*. 2009). This section mainly focus on the fabrication of AgNPs. The vast majority of colloid synthesis is based on a two-step process known as "seed-mediated growth" (Grzelczak *et al*. 2008).

1.4.1 Nucleation and Seeds formation

In step one, precursor molecules undergo nucleation to form small nanocluster "seeds". This nucleation process can take different pathways depend on the supply of metal atoms. For the decomposite route, the precursors are slowly decomposed from heat or sonication, which leads to the concentration of the metal atom gradually increasing with time. Once the concentration reaches supersaturation level, the metal atoms start to form small clusters (known as nuclei) via aggregation. The nuclei rapidly grow and the free metal atoms become depleted; the nucleation then stops (Hornstein and Finke 2004). For the reduction route, the precursor, in its higher oxidation state, is converted into the atomic species (zero-valent) usually via rapid addition of a strong reducing reagent such as sodium borohydride; it is still unclear if the sites of nucleation are formed before or after the reduction started. The structures of nuclei play vital roles in directing the growth of nanocrystals toward their final morphologies. Mass-spectrometry studies showed that 27% (molar) of the total Ag in aqueous silver nitrate ($AgNO_3$) solution are in the form of trimeric Ag clusters (Xiong *et al*. 2007b). Those trimeric atom-clusters have a stronger affinity for electrons than Ag^+ (Fayet *et al*. 1985). Thus, they are more favorable sites for nucleation after the reduction reaction started. It was then proposed that trimeric clusters favor the growth of nuclei into triangular nanoplates in the presence of poly(vinyl pyrrolidone) (PVP) as SEM/TEM images showed the presence of triangular Ag nanoplates in various fabrication procedures using PVP and aqueous $AgNO_3$ solution (Xiong *et al*. 2007b, Jin *et al*. 2003, Langille *et al*. 2013). Once a nucleus has grown past a critical size, it becomes locked into a well-defined structure as structural fluctuations become energetically unfavorable. Face centreed cubic (fcc) metal such as Ag and Au have the tendency to form twin defects because the energy penalty for forming twin defects is very low for these systems. In a typical colloid synthesis, the seeds solutions usually contain various amount of single-crystals, singly twinned and multiply twinned seeds. The distribution of different types of seeds can be manipulated via kinetic control. For example the kinetics of seeds formation can be controlled by using weak reducing agent such as PVP (Washio *et al*. 2006) or slowing down the precursor decomposition by using lower temperature (Xiong *et al*. 2007c). When the kinetics of metal atom generation is slow, there will be more multiply twinned seeds. This is because the formation of multiply twinned seeds requires slow expansion for maximising the surface coverage with {111} facets to compensate the extra strain energy caused by twinning (Ajayan and Marks 1988. Xiong *et al*. 2007c). The structure distribution of the seeds can also be controlled by oxidative etching: The defect zones on the surface of twinned seeds are much higher in energy relative to the single-crystal regions, and they are most susceptible to oxidation that convert zero-valent metal atoms back to ions and diffused into the solution. Single-crystal seeds, in contrast, have no twin boundary defects on the surface, so they are more resistant to oxidative etching. For example, a trace amount of chloride ions was added to the polyol (PVP) synthesis of AgNPs to selective etch and dissolute the twined seeds. As a result, single crystal AgNPs (truncated cubes and tetrahedrons) were obtained at high yields (Wiley *et al*. 2004).

1.4.2 Crystal growth

In step two, each type of seed is thought to preferentially pursuit specific growth pathways that result in specific 3D shapes of the product crystals under typical experimental conditions**.** **Figure 1.6** summarises the correlation that has been established between the structure of the seeds and the morphologies of the product crystals (Xia *et al*. 2009). According to simulations, the size window that favors Ag decahedra and icosahedra is much broader than for other fcc metals (Baletto and Ferrando 2005). As a result, under most reaction conditions, multiply twinned Ag seeds dominate. Ag also has the lowest energy barriers for incorporating stacking faults among the fcc metals; this explains that fact that Ag hexagonal or triangular plates can be easily obtained via different reaction conditions (Swarnavalli *et al*. 2011. Jin *et al*. 2003).

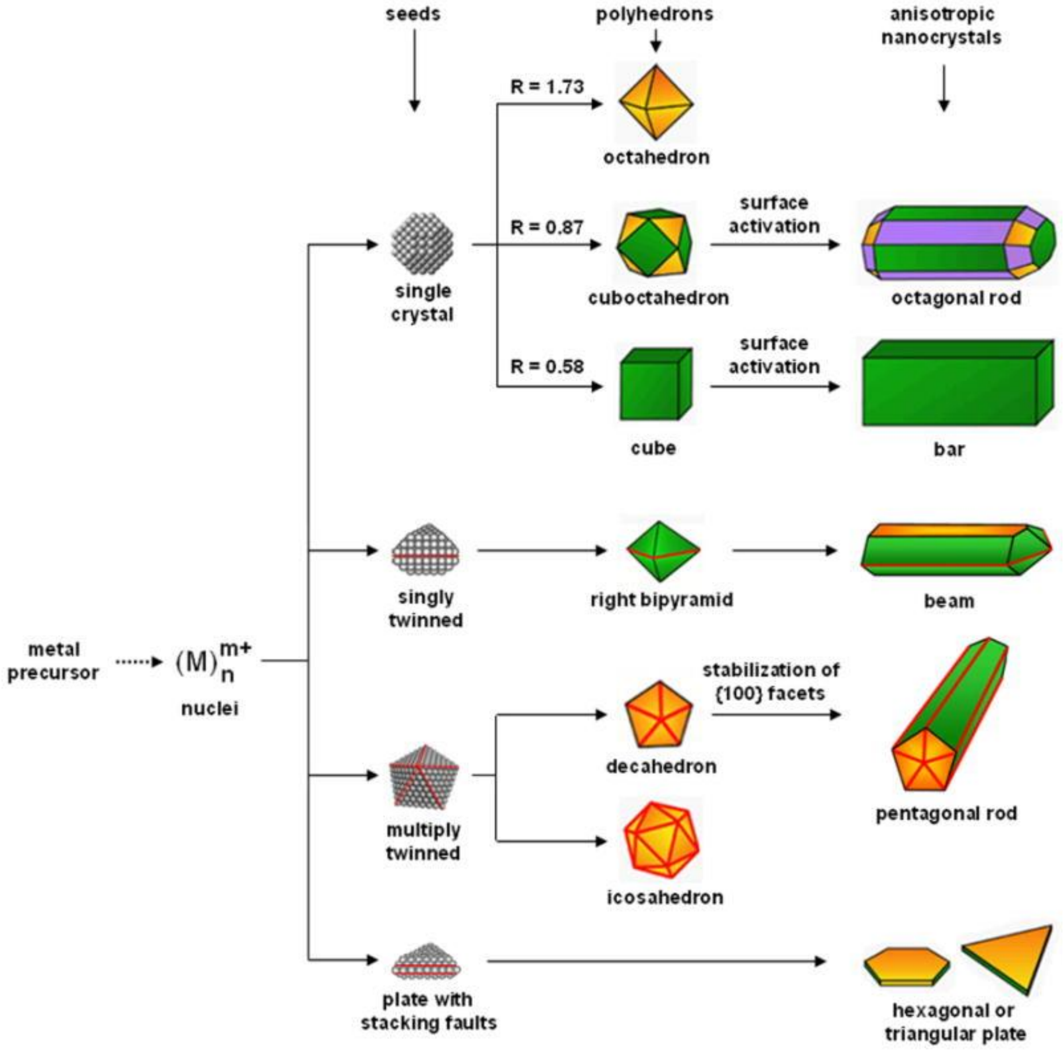

Figure 1.6 Illustration of the crystal growth pathways of fcc metal nanocrystals. Precursors are first reduced or decomposed to form the small clusters (nuclei). Once the clusters have grown past a certain size, they become seeds with a single-crystal, singly twinned, or multiply twinned structure. If stacking faults are introduced, the plate-like seeds will be formed. The purple, orange, and green colours represent the {110}, {111}, and {100} facets respectively. Red lines represent the twin planes. The parameter R is defined as the ratio between the growth rates along the ⟨100⟩ and ⟨111⟩ directions (modified with permission from (Xia *et al*. 2009), copyright 2007 Wiley-VCH).

The evolution of the seeds can be directed by selective capping agents, different capping agents preferentially bind to a specific surface on the metal crystal surface, which changes the order of free energies for different crystallographic planes, thereby altering the relative rate of growth on different surfaces. For example, it has been shown that PVP and Br- ions can selectively bind to Ag {100} facets to slow down their growth rate, resulting in the formation of nanocubes (Wiley *et al*. 2007). Sodium citrate, on the other hand, binds more strongly to Ag {111} facet than {100} facet, resulting in the formation of Ag octahedrons and decahedrons enclosed by {111} facets (Zeng *et al*. 2010. Xia *et al*. 2013).

1.4.3 Plasmon-mediated fabrication

Plasmon-mediated NP synthesis has been an attractive topic since the first discovery by Mirkin's group (Jin *et al*. 2001). They showed that that 5 nm spherical AgNPs could undergo a light-induced conversion into a triangular prism shape that has an average 100 nm edge-size and 16 nm thickness. In their report, the solution of AgNP seeds was prepared like a typical colloid synthesis: a sodium hydroborate solution was injected into an aqueous solution of $AgNO_3$ that contains sodium citrate. A bis(p-sulfonatophenyl) phenylphosphine dihydrate dipotassium salt solution (BSPP) was then added as a particle stabilising agent. In step two, this mixture was subsequently irradiated with a conventional 40-W fluorescent light (multiple sharp emission bands at 546 nm and 440 nm). Time-dependent UV-Vis spectra showed that the seeds solution turned from light yellow colour (absorption peak at about 400 nm) to blue colour with three new absorption peak at 335 (weak), 470 (medium), and 670 nm (strong) after 70 hours irradiation. Those absorption peaks were thought to be the out-of-plane quadrupole resonance, out-of-plane dipole resonance and in-plane dipole plasmon resonance respectively. Time-dependent TEM micrographs showed that both the size and population of the Ag prisms increased with time, whereas the number of seeds decreased with time.

A number of works (Langille *et al*. 2013. Xue *et al*. 2008. Zhang *et al*. 2010) tried to understand the chemical and physical factors that drive structural selection. It has been established that a source of Ag^+, citrate, plasmonic seeds and visible light are four essential components for plasmon mediated fabrication. (Xue *et al*. 2008) proposed that during the irradiated growth steps, the weak reducing reagent citrate itself is inefficient for the NP growth, however, the light activated small AgNP serves as photocatalysts that facilitates Ag^+ reduction by citrate onto the crystalline faces of the AgNP with strong electric field. Thereby, the plasmon excitation (shape dependent) induces ultrafast charge separation on the nanoparticle surface. This likely leads to face-selective Ag^+ reduction, and causes anisotropic crystal growth. (Jin *et al*. 2003) showed irradiation of the seeds solution with a narrowband light source (Xenon lamp with a bandpass filter that has 550 nm centre wavelength, and 40 nm width). The product solution consists of two different size distributions of nanoprisms that have edge lengths of 70 ± 12 nm (referred as type-1) and 150 ± 16 nm (referred as type-2). Because the absorption peak of type-2 (at 1065 nm) was formed after that of type-1 (at 640 nm), and type-2 is twice the edge-size of type-1, each type-2 prism was thought to be the product of an edge-to-edge fusion process of four type-1 prisms. However, the molecular mechanism of this fusion process remains unclear. Interesting, the introduction of a secondary irradiation beam with wavelength that coincides with only the quadrupole resonance (450 nm), but not the dipole resonance (640 nm) of the type-1 prisms, can inhibit the formation of type-2 prisms. It was proposed that the excitation of the dipole surface plasmon resonance redistributes high local fields to the tips of the type-1 prisms, facilitating an edge-to-edge fusion process; the dipole resonance causes ligand dissociation at the particle edges, which would also help the fusion process to occur. In contrast, excitation of the quadrupole surface plasmon resonance inhibits the fusion process due to high local fields generated on the prism edges. The group also showed that when a different primary irradiation wavelength was used, the resulting prisms had an edge-size that increased linearly with the irradiation wavelength, and the absorption peak of the production solutions red-shift further. By monitoring the Ag^+ concentration in solution (via UV-Vis spectra) and the morphological change of the crystal during the irradiation step (Rocha *et al*. 2007) showed that when using a monochromatic light source (Xe lamp with different bandpass filters) for irradiation of the growth solution, the initial rate of Ag deposition was very slow. As crystals gradually grew larger, the absorption wavelength of the growth solution began to speed up approaching the irradiation wavelength the Ag deposition. After the absorption wavelength passed the irradiation wavelength, Ag deposition decreased significantly. The longer the irradiation wavelength, the slower the initial growth rate and the greater the final edge-size of the prisms. A mechanism of size control of nanoprisms during the irradiation step was proposed (Langille *et al*. 2013): smaller crystals that strongly absorb light will continue to grow rapidly. At the same time, larger crystals have LSPRs that are redshifted from the irradiation wavelength, causing their absorption to drop off significantly, and lead to slowed growth. Overall, this process has a size-focusing effect. Like thermal mediated colloid synthesis described in

Section 1.4.2, the shape of the product crystal is determined by the crystallographic features of the seed and its growth kinetics. Much of studies were focused on how triangular prisms were formed during plasmon mediated fabrication: Ag seeds very often contain twin planes and stacking faults, which introduce high-energy surface sites where Ag^+ reduction are more favorable, hence those sites are the origin of anisotropic growth (Xia *et al*. 2009). Electron diffraction and electron energy loss spectroscopy showed that the product nanoprisms fabricated in (Jin *et al*. 2001) are bound on the top and bottom planar faces by {111} surface facets, which are the lowest energy surface facets for fcc metal. Sodium citrate is known to bind more strongly to Ag {111} facet than {100} facet (Zeng *et al*. 2010). Because the top and bottom planar faces of the crystal have much weaker EM field under irradiation, sodium citrate on the {111} surface facets serves as capping agent instead of reducing agent. Therefore growth in the lateral direction (on the tip and edge of the crystal) is much faster than on the planar faces. For both thermal and plasmon mediated fabrication (Rocha *et al*. 2007. Zhang *et al*. 2010), kinetic control requires slow rates of Ag^+ reduction, which favors deposition of Ag onto the highest energy locations of a nanostructure. In the case of the nanoprisms, this occurs on their edges and results in lateral growth. This explain the fact that silver nanoprism formation required irradiation with long wavelength (<500 nm), which is further away from the absorption frequency of the seeds. It is important to understand that the photoexcitation itself does not direct shape formation, but the structure of the seeds and specific reaction conditions for that drive and direct crystal growth. TEM micrograph showed that small silver nanoprisms were form before the absorption peak of the reaction solution came close to the irradiation wavelength (Rocha *et al*. 2007). Photoexcitation is just one of the ways to affect the kinetics of Ag deposition and the size of the nanostructures.

Since the first paper published nearly 20 years ago, AgNPs with various shapes and sizes were fabricated using plasmon mediated methods. A number of publications have shown plasmon-mediated synthesis of silver cubes (Personick *et al*. 2013), decahedron (Zheng *et al*. 2009. Pietrobon and Kitaev 2008), tetrahedron (Zhou *et al*. 2008b). nanorods (Zhang *et al*. 2011) and bi-pyramid (Zhang *et al*. 2009). The underlying published procedures for those syntheses are strikingly similar: small silver seeds (<5 nm) were first fabricated by reduction of silver ions (silver nitrate) with a strong reducing reagent (sodium borohydride) as well as sodium citrate. The seed solution was then grown under intensive irradiation with visible light for at least 7 hours, which resulted in large AgNPs with 3-D polygonic shapes.

120 nm edge-length Ag nanocrystals with tetrahedral shapes and {111} faces were fabricated via the two steps plasmon-mediated method by (Zhou *et al*. 2008). Ag seeds solution was initially irradiated with a sodium lamp; tartrate was added to the solution in the beginning, which is thought to assist the nucleation of small Ag seeds into tiny tetrahedra through face selective adsorption. After 9 hours irradiation; citrate was added to the solution which is thought to assist the growth of tetrahedra by selectively capping {111} facets. The mixture was then irradiated with the same light source for 20 hours to form 90% regular tetrahedra. Like the plasmon mediated fabrication of bipyramids described above (Zhang *et al*. 2010), slow growth rates is the key to control Ag deposition onto the {111} facets. HR-TEM micrographs showed that the product Ag tetrahedra have single crystalline NPs and presumably originate from single crystal seeds.

Like triangular prisms, right triangular bipyramids contain twin planes and/or stacking faults that bisect the structure along the {111} plane. However, unlike prisms, right triangular bipyramids are not bound by flat {111} facets, but they are consist of two right tetrahedra symmetrically joined at their bases, resulting in six {100} facets. Jian Zhang and coworker have fabricated right triangular bipyramids (Zhang *et al*. 2010) via plasmon mediated methods (a 150-W halogen lamp coupled with an optical band-pass filter 550±20 nm, BSPP was added to chelate with the Ag^+ in solution). The coordination of BSPP to Ag^+ moderates the concentration of aqueous Ag^+, thereby affecting the Ag^+ reduction rate. The reducing ability of citrate was also controlled by the pH of the reaction solution. At higher rate of Ag^+ reduction (higher pH, and lower [BSPP] / [Ag^+]), Ag preferential deposited onto {111} facets of planar-twinned seeds, which led to monodisperse right triangular bipyramids. Conversely, at lower rate of Ag^+ reduction (lower pH, and higher [BSPP] / [Ag^+]), Ag preferentially deposited on {100} facets of planar-twinned seeds, which led to increasing amount of Ag plates. Without BSPP, the Ag^+ concentration in the reaction solution rapidly decreases so as the reaction rate, which changes the preferred facet for silver deposition. At the beginning of the reaction, Ag only deposits on {111} facets and results in the formation of right triangular bipyramids, which only have {100} facets. As the reaction rate decreases with the concentration of Ag^+, the facet deposition preference changes from {111} to {100} and results in the formation of truncated right bipyramid, with {111} facets (**Figure 1.7**).

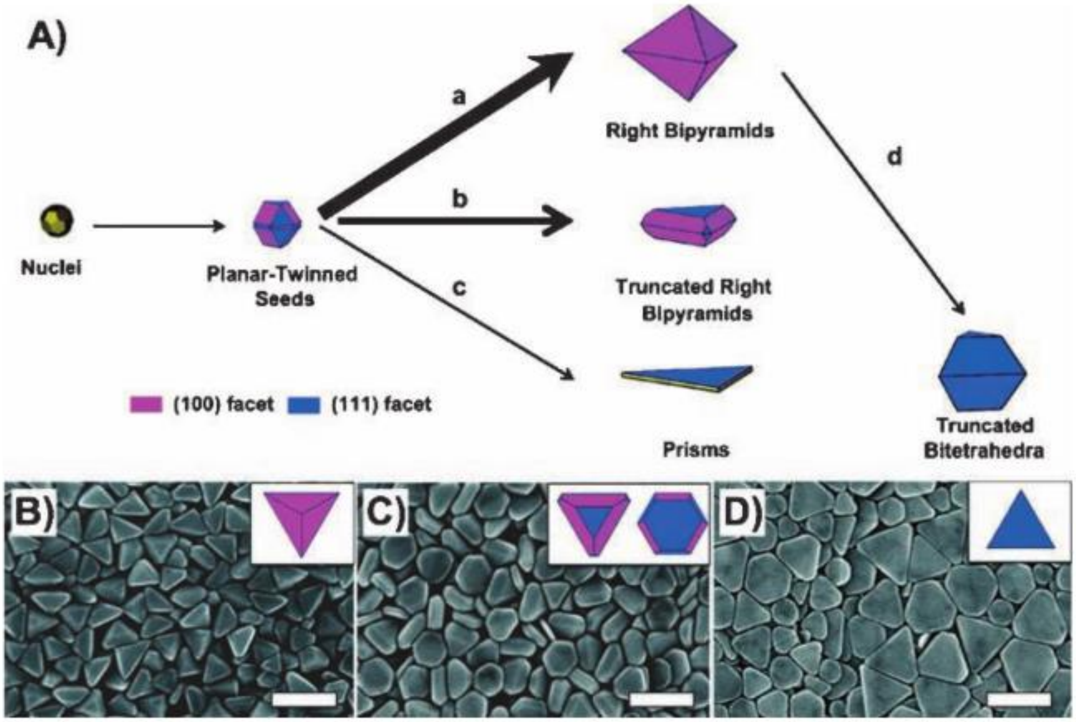

Figure 1.7 A) proposed scheme of the growth pathways for twinned silver nanoparticles seeds. The purple and blue colours represent the {100} and {111} facets, respectively. The thickness of the arrow indicates the relative rates of the reactions with a thicker arrow indicating a faster reaction rate. SEM images of B) right triangular bipyramids, C) truncated bipyramids, and D) triangular nanoprisms generated from reactions having a solution pH of 11, 9, and 7, respectively ([BSPP]/[Ag$^+$] = 1). Reproduced with permission from (Zhang *et al*. 2010) Copyright © 2010 American Chemical Society.

Ag decahedra were first obtained as a minor product (less than 50%) from irradiating Ag seeds with 476.5 nm laser excitation (Zheng *et al*. 2007). TEM micrographs showed that the product solution also contained triangular plates and 3D particles with trapezoid-shaped, kite-shaped and truncated-kite-shaped projections. Later on, by adding L- Arginine to the seeds solution and using blue light (metal halide lamp with a LS-500-R-HS07 Corion filter) for irradiation, Pietrobon and Kitaev were able to fabricate 35 nm Ag decahedra with high yield. Arginine was thought to accelerate the photochemical transformation of the seeds to decahedra by limiting the growth of platelets. However, 3D particles with trapezoid-shaped, kite-shaped and truncated-kite-shaped projections were still found on the TEM micrograph as minor byproducts; the edges of the decahedra started becoming rounded after prolonged irradiation (>10 hours). The group also showed that larger decahedra, up to 120 nm edge-size, can be produced by regrowing the 35 nm decahedra with additional Ag seeds solution under blue light (380 nm to

510 nm) irradiation. Analysing TEM micrographs at different stages of the photoinduced growth process, Zheng, Lombardi and co-workers (Zheng *et al*. 2009) proposed that Ag decahedra crystals are evolved from penta-twinned seeds. Small amount of tetrahedra, bipyramids, and tripyramids are also present in the solution. The authors also proposed that some decahedra were formed by a step-wise aggregation process of tetrahedron (**Figure 1.8**).

In conclusion, plasmon mediated fabrication is a simple but versatile technique, It provides high degree of crystallinity, great structural control and tuneable LSPRs of product NPs. Notably, the optical properties of individual AgNPs from plasmon mediated fabrication have not yet been studied in the literature. In this thesis, Ag decahedrons were fabricated and studied the extinction cross-section and spectra of individual particles immobilised on the solid phase with quantitative wide-field extinction and correlative imaging (see **Chapter 5**). This study not only facilitates a better understanding of how the shape and size of Ag crystals determine their optical properties, but also provides new insights on the plasmon mediated fabrication in terms of how the light interacts with the NPs to influence the growth pathways of the crystals.

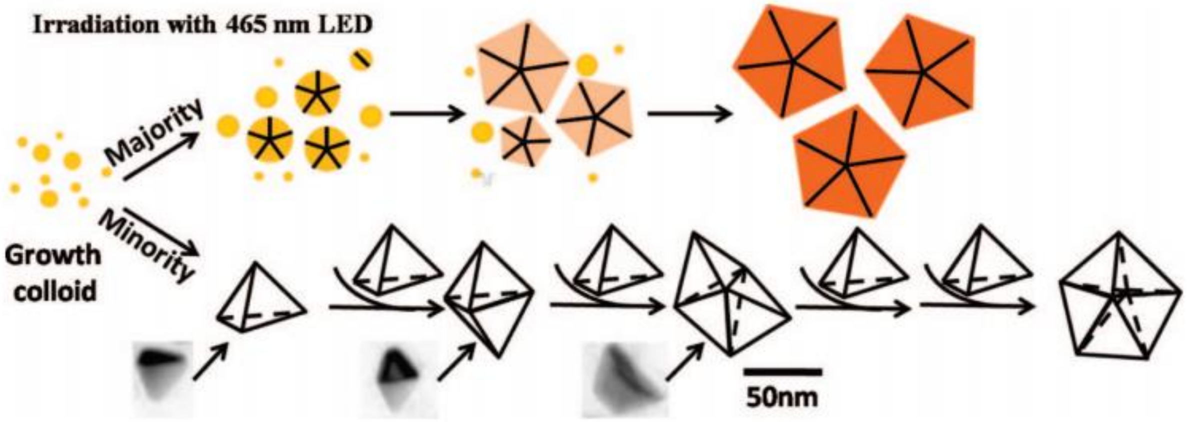

Figure. 1.8 Proposed mechanism on formation of silver decahedron during plasmon mediated fabrications. Reproduced with permission from (Zheng *et al*. 2009) Copyright © 2010 American Chemical Society.

Chapter 2. Setups, Materials and Methods

2.1 Procedures

2.1.1 Dimer fabrication

Details on developing this novel NP dimerisation methodology is described in **Chapter 6**, which includes data and hypothesis of the dimerisation reaction via PxDT with various length. Here, a general protocol is presented for preparing the stable dimers with average 7.35 nm interparticle distance in aqueous solution.

For the dimerisation reactions shown in this thesis, 25 μL sodium citrate (2 mM) stabilised AgNP stock (40 nm diameter, $OD_{400nm} = 4$, equivalent to 7.7×10^{10} particle/mL, supplied by BBI solution) was first diluted with 425 μL deionised water. The AgNP solution was briefly vortexed then sonicated for 10 mins. the polymer P1000DT (Sigma Aldrich) was warmed up in its bottle on a hotplate at 40℃ until it melt from solid to liquid; 4 mM (or 10 times of whatever final concentration used) stock solution of the polymer was prepared with deionised water, and 50 μL of this stock solution was mixed with the AgNP solution and briefly vortexed then transferred into a polystyrene cuvette (path length = 1 cm) for UV-Vis spectroscopy; the reaction was stopped by diluting (at least 1 in 5) the reaction solution with water then immediately immobilise the NPs onto a substrate (coverslip or TEM grid). To prepare stable dimers in aqueous solution, AgNPs were first mixed with 0.4 mM P1000DT and kept for 30 mins at room temperature. 50 μL of 50 mM N-ethylmaleimide (NEM) (Sigma Aldrich) in water was added to the reaction solution and kept for 30 mins at room temperature to quench the free thiol groups. The reaction solution was then transferred into a clean dialysis tube (Slide-A-Lyzer™ MINI Dialysis Devices, 7K MWCO, Fisher Scientific). The dialysis tube was capped and incubated in 50 mL deionised water with mild stir for 4 hours, the dialysate was replaced with freshly deionised water every 30 mins to speed up the removal of the polymers.

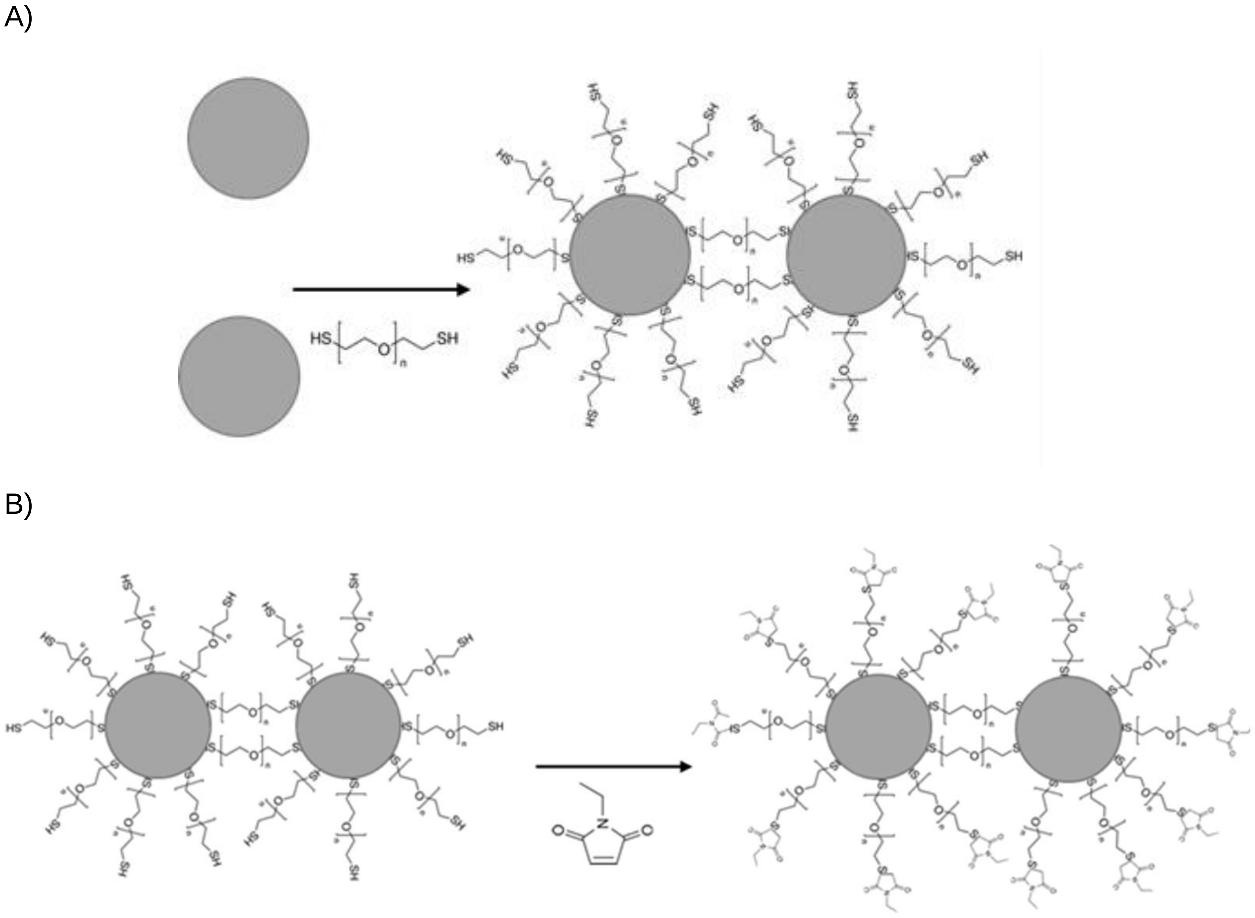

Scheme 2.1 Fabrication of stable AgNP dimers in solution. **A**) PxDT induced dimerisation **B**) Further aggregation can be prevented by capping the thiol groups with NEM.

2.1.2 Plasmon mediated fabrication

Plasmon mediated fabrication is known to produce AgNP with various shapes and sizes (**Chapter 5**). The protocol used is based on (Zheng *et al*. 2009. Pietrobon and Kitaev 2008). The seeds were fabricated by reduction of silver nitrate ($AgNO_3$) in an aqueous solution, which was then irradiated via a LED light source. The end products were dependent on the wavelength of the LED used.

To prepare 8 mL seeds solution, mix 0.5 µM of silver nitrate (Sigma Aldrich), 6.25 µM PVP (Mw ~ 10k) (Sigma Aldrich); 3 mM trisodium citrate ($Na_3C_6H_5O_7$) (Sigma Aldrich) and 0.65 µM of sodium hydroborate ($NaBH_4$) (Sigma Aldrich) with vigorous stir for 3 mins at room temperature. The seeds solution can be stored in the dark at 4 °C for up to 4 weeks.

A)

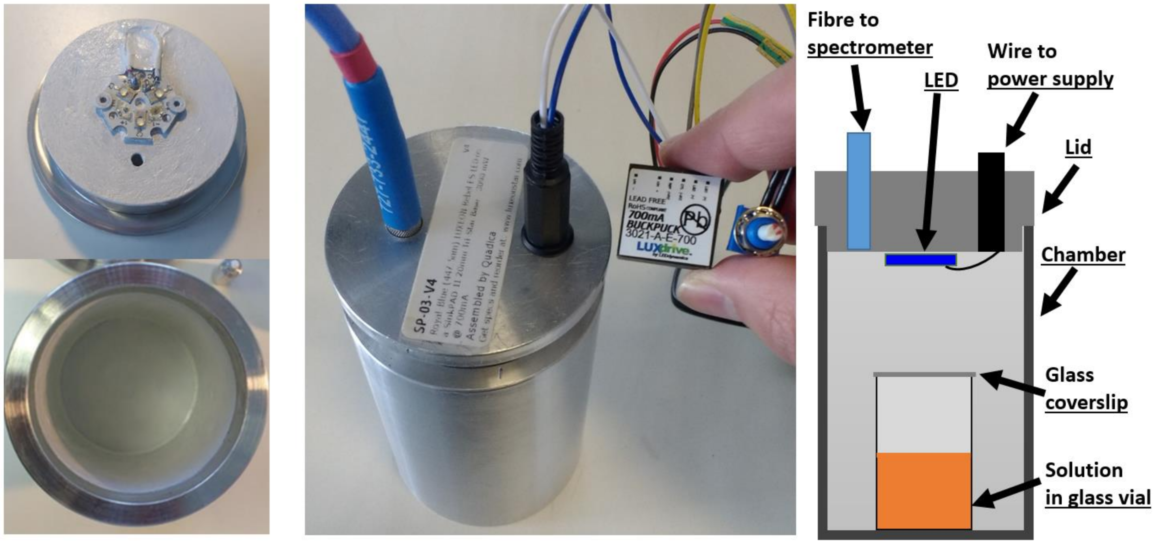

B)

Nominal Wavelength	Measured mean wavelength of reflected (nm)**	measured Max Output (mW)*
Royal-Blue (447.5 nm) LUXEON Rebel ES LED on a SinkPAD-II 20 mm Tri-Star Base - 3.09 W	446.9	710
Blue (470 nm) LUXEON Rebel LED on a SinkPAD-II 20 mm Tri-Star Base - 2.1 W	479.0	382
Cyan (505 nm) LUXEON Rebel LED on a SinkPAD-II 20 mm Tri-Star Base - 1.53 W	500.0	285
Green (530 nm) LUXEON Rebel LED on a SinkPAD-II 20 mm Tri-Star Base - 0.79 W	523.94	190
Lime (567 nm) LUXEON Rebel ES LED on a SinkPAD-II 20 mm Tri-Star Base - 1.44 W	536.21	365
Red-Orange (617 nm) LUXEON Rebel LED on a SinkPAD-II 20 mm Tri-Star Base - 1.68 W	621.56	316
Deep Red (655 nm) LUXEON Rebel LED on a SinkPAD-II 20 mm Tri-Star Base - 1.92 W	654.71	440

C)

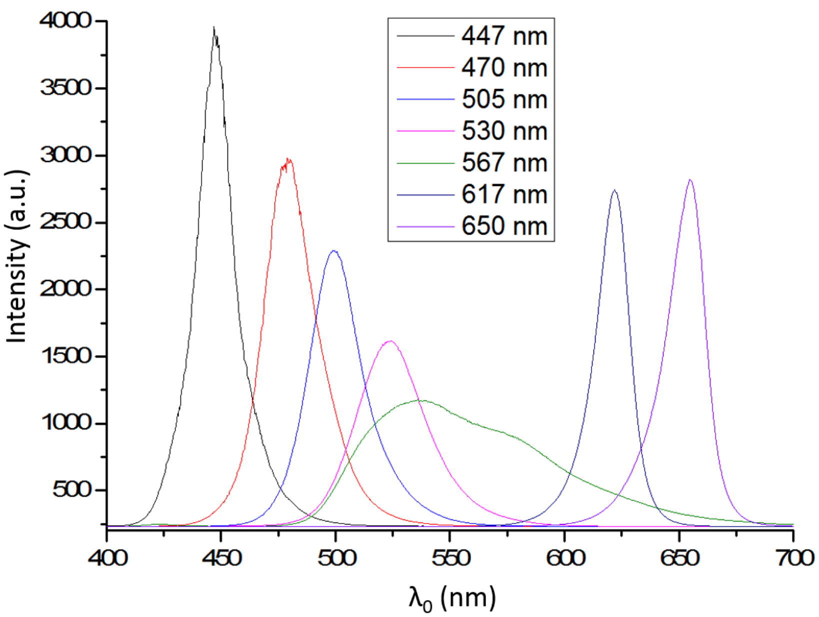

Figure 2.1 A) Irradiation chamber for plasmon mediated fabrication in the lab (Prof Borri and Langbein group, School of Biosciences). **Left**) the inner surface of the irradiation chamber was painted to provide light reflective surface. **Middle**) Photo of the chamber during the irradiation. The LED was powered through the black coloured plug and blue/black cable to the driver and power brick, the reflected output was guided to a spectrometer via the blue fibre. **Right**) Schematic cross-section of the chamber during irradiation. **B**) A table listing all the available LEDs purchased and mounted. ***:** The max output power was measured by placing the power-meter directly in front of the mounted LED on 700 mA. **: The empty painted irradiation chamber was illuminated separately with each LED at different An optic-fibre guided the light in the chamber to the Ocean-Optics Modular spectrometer, and the spectra were taken. **C**) The spectra of the reflected light in the empty chamber from each LEDs

Irradiation protocol used during my internship at the Istituto Italiano di Tecnologia (IIT): a ThorLabs Mounted LED (Blue: M455LP1, Green: M505L3 or red: M625L3) was linked on a ThorLabs SM2 lens Tube (3” thread Depth) which serves as the irradiation chamber. The internal surface of the chamber was wrapped with aluminium foil to maximise the irradiation intensity to the seeds solution. The seeds solution was contained in a glass vial (Fisherbrand™, Type 1 Class A Borosilicate Glass) that was placed in the irradiation chamber. The LED was powered by the ThorLabs T-cube LEDD1B, (1200 mA), which can drive the red, green or blue LED to their maximum output power of 900 mW, 400 mW or 700 mW respectively. To monitor the reaction during the irradiation, the LED was paused and the solution was taken out and sampled for UV-Vis spectroscopy, then put back to continue the irradiation.

Irradiation step at Cardiff University (Prof Borri and Langbein lab, School of Biosciences): the irradiation chamber (inner volume: diam.53 mm x height.95 mm, made of aluminium) was custom built by the mechanical workshop at Cardiff University, School of Physics and Astronomy (**Figure 2.1 A**). The inner surface of the chamber was painted first with a white primer (GLOWTECH, UK) then by a reflective varnish (GLOWTECH, UK) to maximise the irradiation intensity to the seeds solution. 7 high power LEDs each mounted on a heat sink were purchased from LuxeonStarLEDs (**Figure 2.1 B**). Each LED was mounted onto a custom built lid for the irradiation chamber. The Inner side of the lid was also painted in white and coated with varnish. The mounted LED on the lid was powered by a 700 mA LED Power Modules (3021 BuckPuck from LUXdrive^{TM}). During the irradiation step, a small fraction of the light from the chamber was guided to an OceanOptics spectrometer (see **Section 2.2.2**) for monitoring the spectral change of the seeds during irradiation without disturbing the solution. The spectra of the collected light from each LED (without sample inside) are shown in (**Figure 2.1 C**)

2.1.3 Glass functionalisation

To activate the glass surface, the coverslips (agar scientific No 1.5) were fully immersed in Piranha solution (98% H_2SO_4:30% H_2O_2 mixed in 3:1 (v/v) ratio) (both from Sigma Aldrich) in a beaker at 90°C for 60 mins (**Scheme 2.2**), then rinsed in pure water for 3 times and dried by a stream of nitrogen. These activated coverslips were then stored at 4°C under nitrogen for no more than 2 weeks.

The activated coverslips were fully immersed in 1% (v/v) (3-aminopropyl) triethoxysilane (APTES) in pure ethanol for 30 mins, then washed with ethanol and water 3 times. They are dried in a stream of nitrogen before cured at 120 °C for 1 hour in an oven (**Scheme 2.3**). The coverslips were stored at 4°C under nitrogen for no more than 2 weeks.

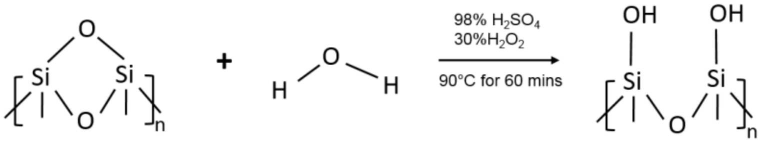

Scheme 2.2 Acid catalysed hydrolysis of the siloxane bond on silicate surface.

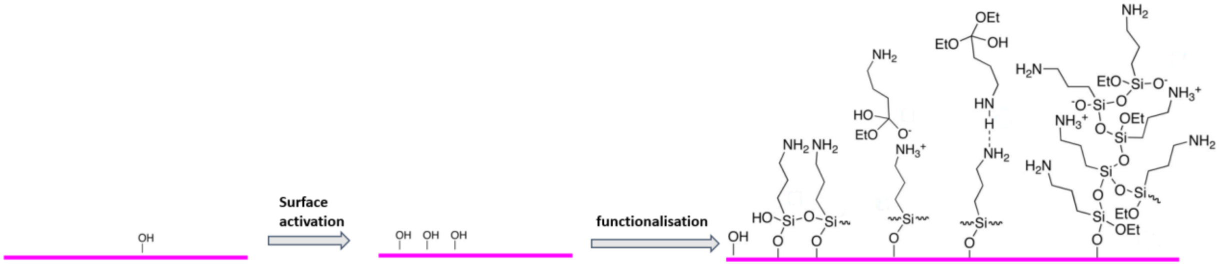

Scheme 2.3. 2 step chemical modification of the SiO_2/glass substrate: step 1: acid activation, and step 2: APTES functionalisation of the 40 nm thick SiO_2 film (purple line) on the silicon grid.

2.1.4 TEM grid functionalisation

Details on developing this novel NP immobilisation technique is described in **Chapter 3**, which includes the rationale on recipe of reaction solution. Here, a general protocol is presented for preparing the substrate for **Section 2.1.5**.

1. A silicon TEM grid with a 40 nm thick SiO_2 film on a silicon nitride mesh (TED PELLA, INC.) was washed in the following sequence: deionised water, acetone, anisole then ethanol. This was repeated twice, then the grid was dried in air
2. A Teflon coated reverse action tweezer was used to hold the grid in the following steps. The grid was incubated in 10 mL etching solution: 500 µL H_2SO_4 (98%) diluted in 9.5 mL of 30% H_2O_2 at 55 °C for 1 hour. The grid was then washed 3 times in water, followed by 3 times in ethanol.
3. 200 µL of (3 aminopropyl) triethoxysilane (APTES) (Sigma Aldrich) was centrifuged at 20k rcf for 20 mins to spin down any large debris, 100 µL of this APTES stock was then diluted in 9.9 mL ethanol (absolute, for HPLC, ≥99.8%, Sigma Aldrich) to make 1% (v/v) APTES solution. The activated TEM grid was incubated in 1% of APTES solution for 1 hour (**Scheme 2.3**). The grid was then washed 3 times in ethanol followed by 3 times in water.
4. The functionalised grid was dried in air at 55 °C for 30 mins and stored at 4 °C for no longer than 2 weeks.

2.1.5 NP immobilisation via drop casting

A) On glass

A glass coverslip (agar scientific No 1.5) was first cleaned with Piranha solution (see **Section 2.1**). One side of the coverslip was marked with the letter ‘C’ for identifying the face of the coverslip in the following steps. The coverslip was placed on a piece of non-scratching tissue (Cleanroom grade wipe) in a Petri dish with the unmarked side facing up. The Petri dish was placed onto a hotplate set at 60°C in a fume hood. 50 μL of diluted AgNP solution (final $OD_{400nm} = 3 \times 10^{-3}$) was dropped onto the surface of the coverslip, the Petri dish was partially covered to minimise dust. The drop of the AgNP solution dried out after one hour. Then the coverslip was immediately mounted in silicone oil (n = 1.52). The mounted sample slides were stored at 4°C for no more than 4 weeks.

B) On SiO_2 TEM grid

A TEM grid with 40 nm silicon dioxide (SiO_2) Support Films (TED PELLA, INC.) was washed with water, acetone then water and let dry in air. The cleaned grid was then placed on a piece non-scratching tissue (Cleanroom grade wipe) in a Petri dish with the dull side facing up. The Petri dish was placed onto a hot-plate set at 60°C in a fume hood. 9 μL of diluted AgNP solution (final $OD_{400nm} = 3 \times 10^{-3}$) was dropped onto the surface of the grid. The AgNP solution on the coverslip dried out after half hour. The grid was then mounted immediately for imaging. After imaging. The sample grid was stored in a 76 mm x 25 mm grid holder box. The grid holder box was kept in the sealed container that is filled with nitrogen gas and stored at 4°C for no more than 2 weeks.

2.1.6 NP immobilisation via Settlement

Details on developing this novel NP immobilisation technique is described in **Chapter 3** (On grid) and **Chapter 6** (On glass) which includes how NP density on the substrate can be controlled. Here, a general protocol is presented which is suitable for most metal NP suspended in water.

A) On glass

A glass coverslip (Agar Scientific No 1.5) was first cleaned with Piranha solution and functionalised with 1% of APTES (**Section 2.1.3**). One side of the coverslip was marked with the letter ‘C’ for identifying the facing of the coverslip in the following steps. The coverslip was placed on a piece non-scratching tissue (Cleanroom grade wipe) in a Petri dish with the unmarked side facing up. For the AgNP-P1000DT dimer sample, the reaction solution was first diluted 20 times with water (final $OD_{400nm} = 6 \times 10^{-3}$), and 300 μL of this diluted reaction solution was dropped onto the coverslips. The Petri dish with coverslip was placed next to a tissue towel soaked with water and both were covered by a large glass beaker to prevent evaporation and dust. After 10 mins incubation time, the diluted AgNP solution on the coverslip was removed, and the coverslip was washed 3 times in water and dried under nitrogen gas, then it was stored in a 50 mL centrifuge tube filled with nitrogen gas at 4ºC for no longer than 2 weeks.

B) On SiO_2 TEM grid

To immobilise NPs onto a functionalised silicon dioxide grid, the absorption spectrum of the NP stock solution was taken to calculate the factor of dilutions for the desirable NP density. **Figure 3.4** exemplifies this characterisation, where 9 μL of 75 nm edge size Ag-cube solution with $OD_{515nm} = 0.1$ (absorbance of the solution at 515 nm wavelength, which is directly proportional to the molar concentration of the NPs) produced 95.0×10^{-3} per μm^2 NP density. The APTES functionalised grid in the grid holder (kept in a sealed container) was first equilibrated to room temperature and washed in water, then briefly let to dry off the excess amount of water on its the surface. A steel reverse action tweezers was used to firmly hold the grid on a flat surface (see **Figure 2.2**). For the AgNP-P1000DT dimer sample, the reaction solution was first diluted 20 times with water (final $OD_{400nm} = 6 \times 10^{-3}$), 9 μL of this diluted reaction solution was carefully dropped onto the dull side of the grid (facing upward), and the whole tweezers was placed next to a tissue towel soaked with water and both were covered by a large glass beaker to prevent evaporation and dust. The grid was incubated with the NP solution for at least 10 mins (at low room humidity, the NP solution had to be topped-up). Finally, the grid was washed 3 times in water and dried under nitrogen gas, then it was stored in a standard grid storage box in nitrogen gas at 4 ºC for no longer than 2 weeks.

Figure 2.2 A photo shot showing the NP settlement step: a steel reverse action tweezers was lying flat in a glass container, the tip of the tweezers held the frame of the sample grid with 9 μL NP solution covering the top surface of the grid.

2.1.7 TEM sample grid mounting

Details on developing this novel mounting techniques is described in **Chapter 3**, which includes the rationale on the choices of the mounting geometry and medium. Here, a general protocol is presented for repeating the same or similar measurements shown in this thesis.

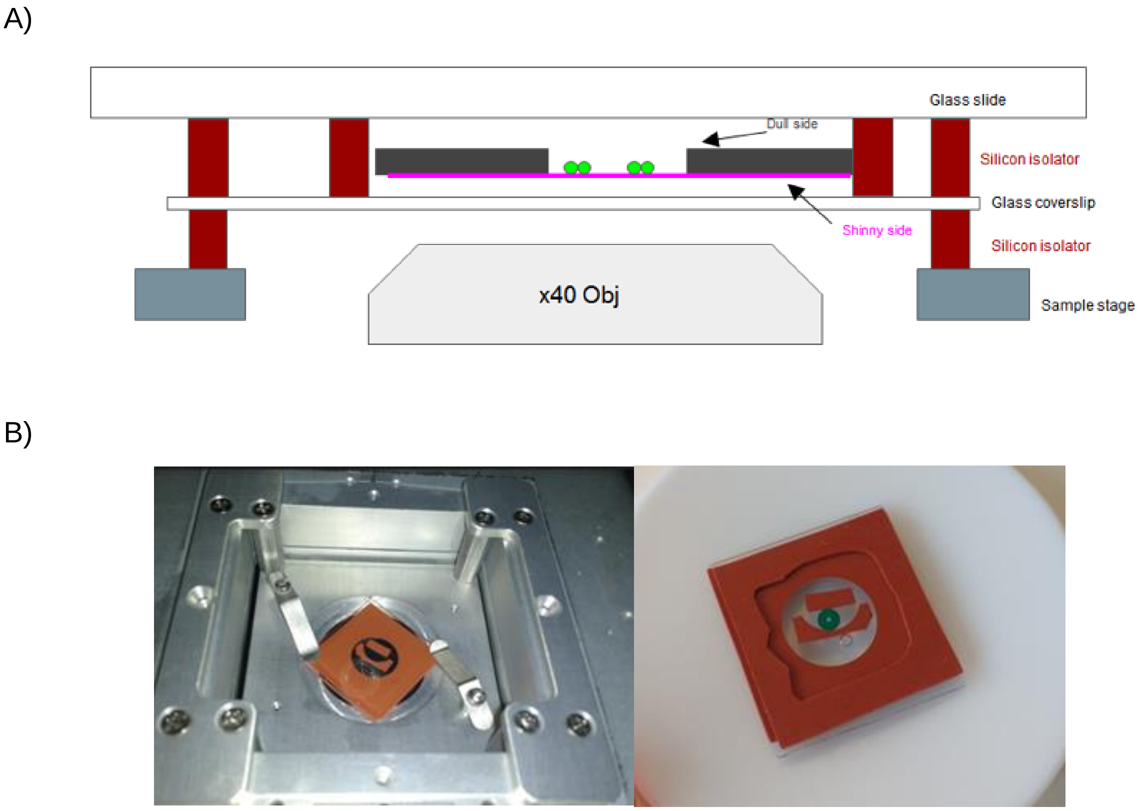

Figure 2.3. A) Schematic drawing of the mounted sample grid on the nano-positioning stage of the microscope. **B) Left**: photo of the positioned sample slide on the stage, ready for imaging. **Right**: prepared sample slide.

To mount the sample, the APTES functionalised grid was first equilibrated in its container to room temperature (if it is from a fridge). Standard sized 25 x 75 mm glass slides (Menzel Gläser) were cleaved into 2.5 cm x 2.5 cm shape to fit into a specialised sample stage used for nanometric position accuracy on the inverted microscope stand (**Figure 2.3 B**), see also **Section 2.2**. The glass coverslips (Agar Scientific No 1.5, 2.5 cm x 2.5 cm) and the cleaved glass slides are first wiped with non-scratching tissue (Cleanroom grade wipe) soaked with acetone, then rinsed with acetone and deionised water and dried by a stream of nitrogen. A piece of *Press-to-Seal* silicone isolators (Grace^{TM}, Bio-Labs, 13 mm inner diameter x 0.5 mm depth, 25 mm x 25 mm outer size for mounting in anisole, 20 mm inner diameter x 0.5 mm depth, 25 mm x 25 mm outer size for mounting in air) was placed on the cleaned coverslip as a gasket. Another piece of silicone isolator was cut into an oval-shaped cage, which was then placed on the coverslip, in the well region formed by the gasket. 200 µL of anisole was pipetted into the well, and the sample grid was placed within the cage and immersed in the anisole. The shiny side of the grid was facing the coverslip. Finally, the glass slide was placed on the top of the gasket to seal the space containing the sample grid (**Figure 2.3 B right**). Another piece of silicone isolator was sandwiched between the sample slide and the stage to absorb pressure from above and protect the coverslip. The clamp of the sample stage of the microscope provided pressure between the glass slide and coverslip for sealing the chamber filled with anisole during measurements (**Figure 2.3 B Left**).

2.2 Experimental setups

2.2.1. The Inverted Microscope

The main microscopy set-up is built around an inverted microscope stand (Nikon Ti-U) equipped with an 100 W halogen white-light illumination of adjustable intensity, a Nikon neutral colour balance (NCB) filter, or a light balancing LB200 optical blue Hoya filter, an oil condenser of 1.34 numerical aperture (NA) with a removable home-built dark-field illumination of 1.1-1.34 NA, and a choice between a 40x 0.95 NA dry objective, a 20x 0.75 NA dry objective, and a 100x 1.45 NA oil objective. Two interchangeable tube lenses were available, providing a 1x or 1.5x magnification of the intermediate image. The sample position was finely controlled, by a xyz-piezoelectric stage (nanostage). The nanostage (Mad City Laboratory model NanoLP200) had 3 nm positioning precision and 200 µm range. A consumer Canon EOS 40D colour camera, with a 14-bit CMOS detector, containing 2592 x 3888 pixels (10.1 megapixel), of 5.7 µm pixel pitch, and full-well capacity $N_{fw} = 4x10^4$, was attached to the left port of the microscope. A PCO Edge 5.5 scientific-CMOS camera, low noise (1.1 electron read noise), capable of 100 frames per second (FPS) for full sensor, grayscale (b/w), water-cooled to +5 ºC, with 2560 x 2160 pixels (5.5 megapixel), of 6.5 µm pixel pitch, and $N_{fw} = 3 \times 10^4$ was attached to the eye-piece side port.

2.2.2 Cuvette-based spectroscopy

A modular spectroscopy setup was set in the lab to measure the absorption of samples in solution contained in cuvettes. The setup consists of a 7 W lamp, a cuvette holder for 1 cm path length, and a USB spectrometer, all of which are fibre-coupled. All devices, components and software are from OceanOptics. The spectrometer is model USB2000-FLG, with fixed slit-width W_s = 200 µm, a 600 lines/mm grating blazed at 500 nm, ~10 nm spectral resolution, and a built-in Sony ILX511 linear 12-bit CCD array detector with 2048 pixels of pitch W_p = 14 µm. The spectrometer is connected to a PC by USB. The lamp is the model HL2000-FHSA with fixed power setting, manual attenuator, controllable shutter, and wavelength range (360-2400) nm. A LB200 filter was used for all the absorption experiments. Data is collected and analysed with the SpectraSuite software. The absorbance is calculated as:

$A = -\log_{10}(\frac{P_t}{P_i})$**.** Where: P_i is incident power and P_t is transmitted power (**2.1**)

Integration time for all work in this report is 3ms, and we average 1000 measurements in 3 s.

The following concentrations (from the supplier nanoComposix website) of NP were used to estimate the concentration of NP in the solution from the spectral data,

- For 75 nm Ag-cube in water: OD_{515nm} = 1 is equivalent to about 0.36 x10^{10} NP/mL
- For 40 nm spherical AgNP in water: OD_{400nm} = 1 is equivalent to about 1.93 x10^{10} NP/mL

2.2.3 Dark Field microscopy

Figure 1.2 in **Section 1.2.1** shows a scheme of the setup that has been utilised for all the measurements under DF illumination in this thesis. A set of circular stop discs (anodised aluminum film, black colour) corresponding each to a specific microscope objective numerical aperture (NA) have been hand-cut to block the low numerical aperture illumination range and prevent light from the illumination beam path being transmitted into the objective lens. A disc blocking up to 1.1 NA was used for the 40x 0.95 NA dry objective, and a disc blocking up to 0.8 NA was used for the 20x 0.75 NA dry objective; the condenser aperture was closed to 1.3 NA and 0.9 NA respectively to reduce the diffuse scattering background.

For the polarisation-resolved Dark-Field (DF) analysis, a servo-mounted linear polariser in the illumination path before the condenser permitted accurate polarisation control of the excitation. The polariser can be rotated to achieve polarisations in steps of 15° from 0° to 180°. The DF images were taken at each polarisation angle by a colour Canon camera (as described above in **2.2.1**) and saved as JPG files 'L' format for other purposes (3888 x 2592 pixels).

2.2.4 Micro-spectroscopy

The right port of the microscope stand is optically coupled to a Czerny-Turner type imaging spectrometer (Horiba Jobin-Yvon iHR550), with a 1:1 magnification from the intermediate image plane to the input slit. The spectrometer is equipped with a 76 x 76 mm grating having 100 grooves/mm. Attached to the spectrometer output port is a scientific charge-coupled device camera (Andor Newton DU-971N) with a 1600 x 400 pixel sensor, of pixel pitch W_p = 16 μm, peltier-cooled to -60 °C. A 1:1 magnification from the spectrometer entrance slit to the camera implies that the intermediate image plane is imaged on the sensor with a magnification of 1. The CCD sensor has a 1.5 $\times 10^5$ e^- pixel full well capacity.

After focusing the sample via the imaging mode of the CCD camera (Andor Newton DU-971N) on the inverted microscope stand with darkfield illumination, the spectrometer grating was set to the zero order of diffraction, to act as a mirror, in order to identify the NP position and centre it in the middle of the spectrometer slit via the Andor camera two-dimensional live readout. The grating was then rotated to the first diffraction order. To obtain the spectrum of the centred AgNP, different objectives were used depending on the mounting medium:

- For imaging NPs in anisole (Sigma-Aldrich, ReagentPlus®, n = 1.51), silicone oil (Sigma-Aldrich, AP 150 Wacker, n = 1.52) or deionised water (n = 1.33), the 40x 0.95 NA dry objective was used, the slit was closed to W = 60 μm for 100 grooves/mm grating (corresponding to 1.7nm spectral resolution); the vertical size is defined by a 4 pixel vertical binning corresponding to 4 x 16 μm = 64 μm. With a 60x magnification (40x objective and 1.5x tube lens), this corresponds to ca. 1 μm^2 square area on the sample, which is slightly larger than the first dark ring of the Airy point-spread-function to be less sensitive to NP displacements by drifts. The field iris was opened to 500 μm, DF illumination range was 1.1 to 1.3 NA, and BF illumination range 0 to 0.95 NA
- For imaging NPs in air (n = 1.00), the 20x 0.75 NA dry objective was used, the slit was closed to W = 50 μm for 100 grooves/mm grating (corresponding to 1.1 nm spectral resolution); the vertical size is defined by a 3 pixel vertical binning corresponding to 3 x 16 μm = 48 μm. With a 30x magnification (20x objective and 1.5x tube lens), this

corresponds to ca 1.9 μm^2 square area on the sample, which is slightly larger than the first dark ring (0.8 NA disc) of the Airy point-spread-function to be less sensitive to NP displacements by thermal drifts. The field iris was opened to 1 mm, DF illumination range was 0.8 to 0.9 NA, and BF illumination range 0 to 0.75 NA

The exposure times for the DF spectra were chosen depending on the scattering signal intensity of the imaged NP: a longer exposure time is preferable to exploit the full dynamic range of the camera. However, it should not cause any pixel to be overexposed (more than 90% of the sensor's readout saturation) or excess 30s (NPs start to drift away from the alignment). For bright field illumination, spectra were averaged over 300 readouts, each with an exposure time of 0.1 s.

For each imaged NP at each polarisation angle (or using unpolarised light), different kinds of signal S were acquired for calculating the spectra of the imaged NP (see **Section 2.3.2**):
The NP was first focus in the detected region.

- $S_{DF} = eP_{DF}$: Signal scattered from the region with NP in focus under DF illumination
- $S_{BF} = eP_{BF}$: Signal transmitted from the region with NP in focus under BF illumination

Sample nano-positioning stage was then laterally shifted by 3 μm and it was checked with the Andor camera that there was no NP or debris in the detected region after the shift. The following signal were taken from the empty region for spectral referencing.

- $S_{back} = eP_{back}$: Signal scattered from an empty region close to the NP under DF illumination
- $S_{lamp} = eP_{lamp}$: Signal transmitted from an empty region close to the NP under BF illumination
- $S_{dark} = eP_{dark}$: Camera reading with no light impinging on the sensor (digitiser offset + dark current)

Where an overall optical efficiency e were induced that links the measured signal S (in count s/s) to the power P (in J/s, radiated due to transmission and scattering) emitted by the detected region. Optical efficiency e is specific to the optical setup, all spectra for the same NP must be acquired under the same experimental conditions (illumination intensity, slit width, etc.), e is cancelled out during the calculation of σ_{sca}^{DF} and σ_{sca}^{DF}, therefore, no calibration for e is required.

2.3 Analysis Methods

2.3.1 Wide field extinction analysis

Bright-Field extinction measurements and analysis are based on (Payne *et al*. 2013). After placing the sample slide on the microscope stage, in focus and under Köhler illumination, the intensity of the lamp was adjusted to achieve the full-well capacity of the pixels of the PCO camera N_{fw} = 30 000 electrons (this was monitored on the PCO software) with an exposure time in the order of 10ms. For each field of view, two BF images were taken (all with the same exposure time, between 1 ms and 10 ms); one with the NP in focus, and another with the sample nano-positioning stage laterally shifted by 3 µm. Dark images were also taken for blocked illumination, and background subtraction was performed by the ImageJ calculator. This provided the background-corrected transmitted intensity of the BF image with NP in focus, called I_f, and the background-corrected transmitted intensity image with the shifted NP called I_o which is used as reference, to calculate the NP differential transmission. The extinction cross-section of a NP located within the area A_i in the BF image can be expressed as:

$$\sigma_{ext} = \int_{A_i} \Delta dA \text{ where } \Delta = \frac{(I_o - I_f)}{I_o} \quad \textbf{(2.2)}$$

To account for a possible mismatch between I_0 and I_f (i.e. non perfect referencing), a local background procedure was used as follows. A radius r_i approximately at the second Airy ring of the objective point-spread function (3l/(2 NA) was chosen. In the area between the radius r_i and $2r_i$, a local background extinction was calculated:

$$\Delta_b = A_b^{-1} \int_{A_b} \Delta dA \quad \textbf{(2.3)}$$

The background-corrected extinction of the NP is then:

$$\sigma_{ext} = \int_{A_i} (\Delta - \Delta_b) dA \quad \textbf{(2.4)}$$

Different colour filters can be placed into the illumination, to obtain σ_{ext} in different colour bands. This provides a coarse spectroscopy functionality together with a wide-field imaging modality of many NPs simultaneously, as opposed to the method in **section 2.2.3** which gives the spectrum of one individual particle at a time.

An image analysis programme written in ImageJ macro language was developed by Dr. Lukas Paynes in the Borri/Langbein Lab for high throughput automated extinction image analysis; the details are discussed in (Payne *et al*. 2013). The programme is able to produce an extinction image (**Figure 3.3. right**) that gives high-contrast for visualising NPs in the imaged field of view. A single NP in the extinction image appears as two spots, one bright and one dark, due to the referencing via lateral shifting. NPs in the centre of extinction image were selected and labelled and their extinction cross-sections were calculated as described above. The resulting data were listed in an Excel file for statistical analysis.

2.3.2 Optical cross-section calculation

The following formulas were derived by Dr. Attilio Zilli in our group for quantitatively determining (in absolute unit) the optical cross-section spectrum of a NP obtained with the methods described above (**Sections 2.2.4** and **2.3.1**). They are quoted here for clarity and completeness, instead of referring to Dr. Zilli PhD thesis and his (yet unpublished) work.

As mentioned in **Section 2.2.4**, the sensor of the CCD camera measures a detected signal *S* (in counts/s) proportional to the power *P* (in J/s) emitted by the detected region *A* (also as a function of frequency *ω*). *A* is calculated as:

$$A = \Delta x \times \Delta y = \left(\frac{W}{\mu}\right) \times \left(\frac{bL_y}{\mu}\right). \quad (\mathbf{2.5})$$

Where: μ is the magnification factor from the sample to the sensor, W is the horizontal width of the spectrometer input slit, b is the number of pixels binned in the vertical direction, Ly is the pixel size in the vertical direction. For an imaging device, *A* is the area where the integration is carried over during analysis. If *A* encloses only one single nano-object and no other comparable absorbers/scatterers, then the signal from the area can be equated to the signal from the NP.

The optical cross-sections are defined by the relations between incident intensity and power (see **Chapter 1**):

$$\sigma_{sca}^{DF} \equiv \frac{P_{sca}^{DF}}{I_{exc}^{DF}}. \quad (\mathbf{2.6}) \qquad \sigma_{abs}^{BF} \equiv \frac{P_{abs}^{BF}}{I_{exc}^{BF}}. \quad (\mathbf{2.7})$$

Where P_{sca} and P_{abs} are the total power scattered and absorbed by the NP, respectively, and I_{exc} is the excitation intensity. The BF or DF superscript on the physical quantities indicates the corresponding illumination configuration. Under the assumption that the microscope illumination is homogeneous over the imaged area A≃1μm we have:

$$P_{exc}(\omega) = \int_A I_{exc}(x,y,\omega)\,\mathrm{d}x\mathrm{d}y = AI_{exc}(\omega). \quad \textbf{(2.8)}$$

Both under BF and DF illumination. The cross-sections can therefore be rewritten as:

$$\sigma_{sca}^{DF} = A\frac{P_{sca}^{DF}}{P_{exc}^{DF}}. \quad \textbf{(2.9)} \qquad \sigma_{abs}^{BF} = A\frac{P_{abs}^{BF}}{P_{exc}^{BF}}. \quad \textbf{(2.10)}$$

Because only a fraction *f* of the total scattered light is eventually collected, the powers in terms of the measured signals are expressed as:

- $P_{coll}^{DF} = f_{DF}P_{sca}^{DF}$, scattered power collected under DF illumination
- $P_{coll}^{BF} = f_{BF}P_{sca}^{BF}$, scattered power collected under BF illumination

The total scattered power is:

$$P_{sca}^{DF} = \frac{P_{coll}^{DF}}{f_{DF}} = \frac{(P_{DF} - P_{bg})}{f_{DF}}. \quad \text{where } P_{bg} \text{ is the background signal} \quad \textbf{(2.11)}$$

The total extinguished power is:

$$P_{ext}^{BF} = P_{lamp} - P_{BF} + P_{coll}^{BF}. \quad \textbf{(2.12)}$$

Assuming that all other optical interactions are negligible, scattering and absorption account for the complete extinction $P_{ext}^{BF} = P_{sca}^{BF} + P_{abs}^{BF}$. We can thus derive the total absorbed power as:

$$P_{abs}^{BF} = P_{lamp} - P_{BF} + P_{coll}^{BF} - P_{sca}^{BF} = P_{lamp} - P_{BF} - \zeta\frac{1-f_{BF}}{f_{DF}}(P_{DF} - P_{bg}).$$

(**2.13**)

where we have introduced the parameter $\zeta = P_{sca}^{BF} / P_{sca}^{DF}$ as the BF to DF total scattered power ratio (which depends on the geometry of the NP scatterer).

The excitation power is:

$$P_{exc}^{BF} = P_{lamp} - P_{dark}. \quad \textbf{(2.14)}$$

$$P_{exc}^{DF} = \frac{(P_{lamp} - P_{dark})}{\xi}. \quad \textbf{(2.15)}$$

where the parameter $\xi \equiv P_{exc}^{BF} / P_{exc}^{DF}$ has been introduced in the second equation (see Section below). By substituting the expressions above in the definition of the cross-sections we have:

$$\sigma_{sca}^{DF} = A \, \frac{\xi}{f_{DF}} \, \frac{P_{DF} - P_{bg}}{P_{lamp} - P_{dark}} \, . \quad (\mathbf{2.16})$$

$$\sigma_{abs}^{BF} = A \, \frac{P_{lamp} - P_{BF} - \zeta \frac{1 - f_{BF}}{f_{DF}} (P_{DF} - P_{bg})}{P_{lamp} - P_{dark}} \, . \quad (\mathbf{2.17})$$

All experimental spectra (**Section 2.2.4**) are expressed in counts/s (dividing by their exposure time), so that they can substitute the powers on the right hand side since the e factors cancel out. MATLAB codes have been written by Dr Attilio Zilli for the parameters f_{BF}, f_{DF}, and ζ defined by the relations above, and can be estimated analytically in the dipole limit for particles of a simple shape in an isotropic optical environment.

2.3.3 TEM Coordinate Mapping

For correlative imaging (**see Section 3.1**), coloured DF images of the sample grid were taken (see Dark Field microscopy **Section 2.2.3.)** after the optical measurements, to serve as a map. The actual distance (D) and angle ($\angle NP_{DF}$) between the particles of interest were measured from the DF map by ImageJ.

The sample grid was first equilibrated to room temperature before being mounted onto an EM-21010/21020 sample holder (Jeol 2100-JEM) with the dull side facing toward the filament of the TEM microscope. The holder was then inserted into the TEM microscope (Jeol 2100-JEM) for imaging. After aligning the illumination and the image forming system, low magnification was used to identify the SiO_2 window that contained NPs of interest as well as the orientation of the grid in comparison with the DF map. The pattern of local NP distribution was used to correlate the DF map with the TEM imaging display of the attached CCD camera, thereby NPs of interest on the DF map were found on the TEM imaging display.

In order to move the field of view of the CCD camera between the NPs of interest, the coordinates (D, $\angle NP_{DF}$) measured on the DF map were correlated with the sample holder stage controller (**Figure 2.4**): the angle between the edge of the SiO_2 window and the X-axis of the TEM imaging display (∠map-monitor) was measured by an angle ruler (placed on the screen of the PC monitor with the TEM image on display). Since the angle between the X-Axis of the sample holder control (operated on the controller software) and the X-Axis of the TEM imaging display is fixed (∠holder-monitor = 56°), the DF coordinates (D, $\angle NP_{DF}$) were adjusted to guide the controller for moving the sample holder, as follows:

∠(map-holder) = ∠map-monitor - ∠holder-monitor

Move along X-axis = D x cos ($\angle NP_{DF}$ + ∠(map-holder))

Move along y-axis = D x sin ($\angle NP_{DF}$ + ∠(map-holder))

A)

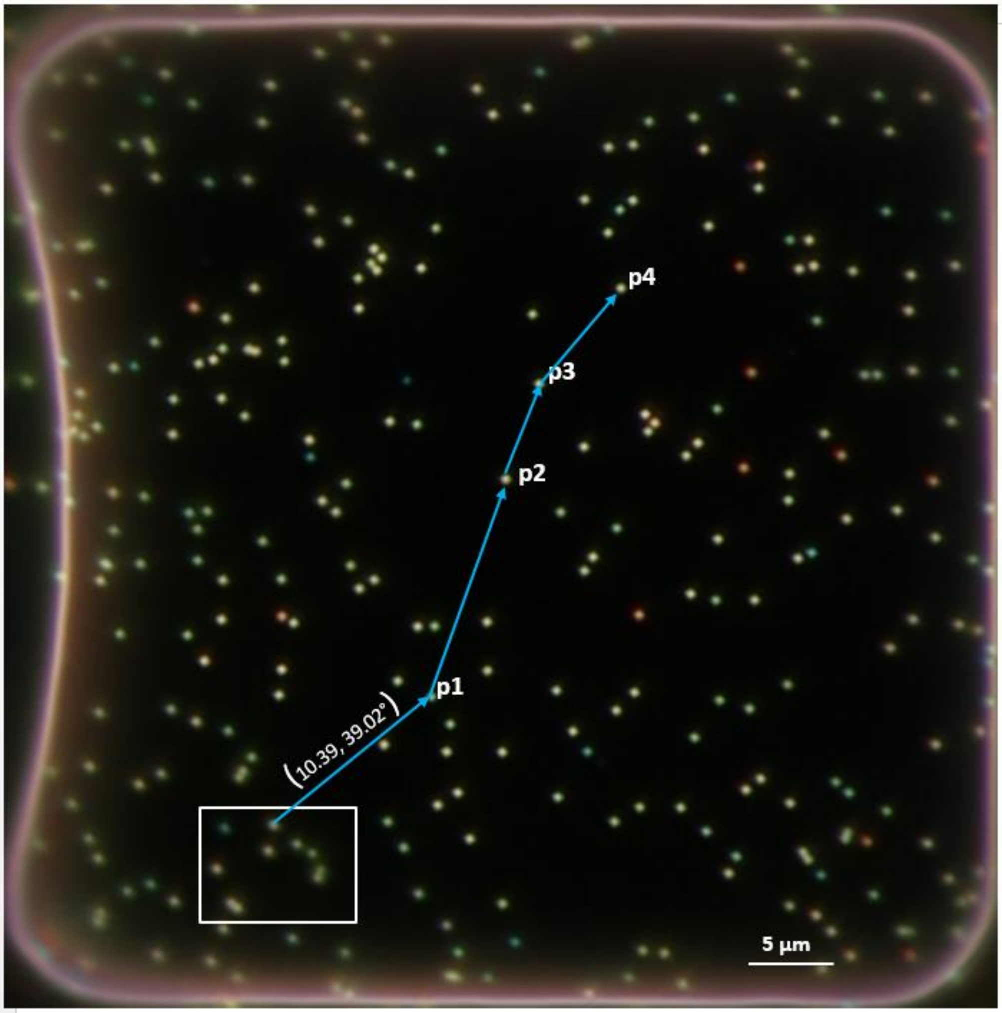

B)

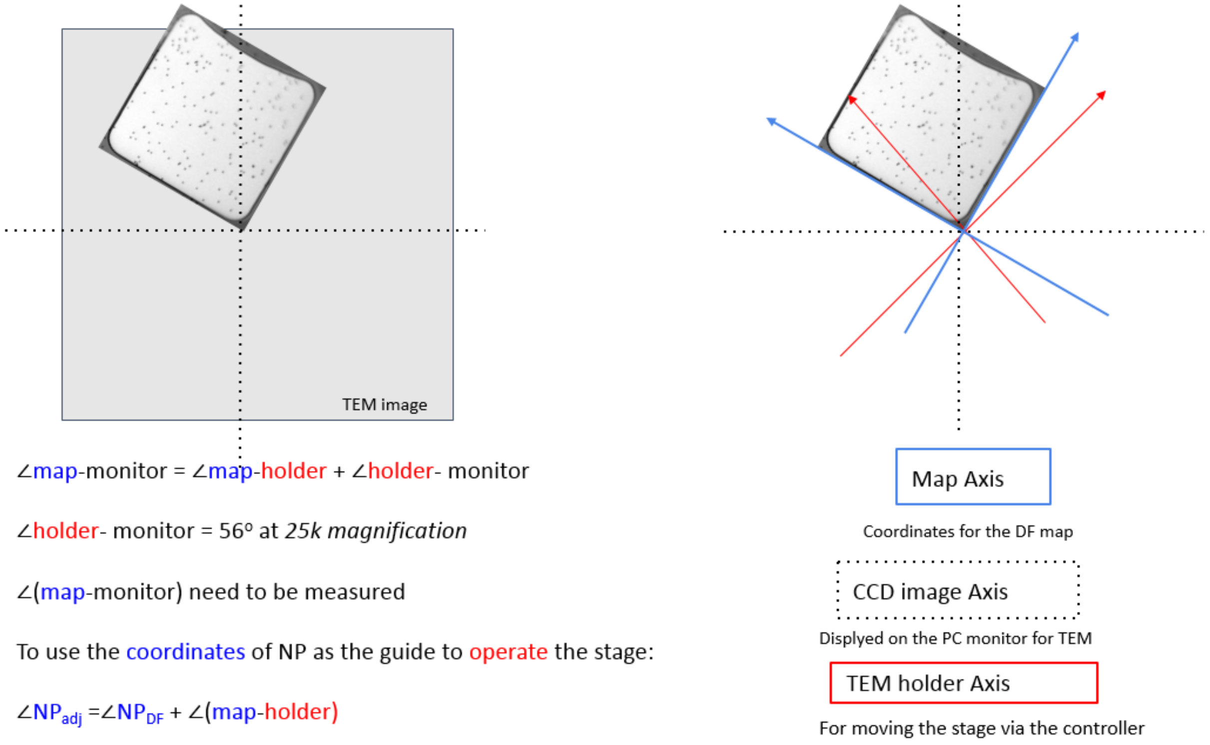

∠map-monitor = ∠map-holder + ∠holder- monitor

∠holder- monitor = 56° at *25k magnification*

∠(map-monitor) need to be measured

To use the coordinates of NP as the guide to operate the stage:

$\angle NP_{adj} = \angle NP_{DF} + \angle(\text{map-holder})$

Figure 2.4: **A)** DF image of the sample grid after optical measurement. The image was rotated so that the curve edge was always aligned with the left edge of the image (defined as 90° for the coordinates). The distance and the angle (blue line arrow) between the NPs of interest were measured as the DF coordinates (white numbers over the blue line). **B)** Alignment of the TEM sample holder with the DF coordinates (see text).

The movement of the sample holder is monitored and operated by the attached control PC. This mapping is only accurate for small movements of the sample holder, each step should be no more than 20 μm. The NP of interest should always be checked by the distribution pattern of surrounding NPs before taking images.

Chapter 3. Correlative Imaging Method

3.1 Light - electron microscopy correlative imaging of single nanoparticles

In this chapter, a novel correlative imaging methodology are developed, which allows one to retrieve the sample TEM grid after optical imaging of the NPs of interest in a homogeneous refractive index environment, followed by complete removal of the mounting medium, allowing to subsequently image the sample by HR-TEM.

3.1.1 Mounting Medium

Methoxybenzene (anisole) was chosen as the mounting medium for several reasons: i) Anisole has a refractive index of 1.516 (Sigma-Aldrich database), closely matching the one of microscope glass, allowing for optical measurements using an oil immersion high resolution objective; ii) The boiling point of this liquid solvent is 154 °C (The Merck Index, 12th ed., Entry# 707.), making it not too volatile for use. However, in a preliminary test (data not shown), a 20 μL drop of anisole on a coverslip evaporated much faster than a 20 μL water drop on a 65 °C hotplate; 20 μL anisole completely evaporated within 5 mins, without leaving any residue mark on the coverslip. This indicates that anisole is more volatile than water at 65 °C, and as a mounting medium it can be completely removed within a relatively short time; iii) After NPs immobilisation via either drop-casting or settlement, the grid must be completely dried to fix the NPs on the substrate before directly mounting it in a nonpolar medium such as silicone oil. In this way, there is no water layer trapped on the surface of the grid, which will interfere with any optical measurement. Since the TEM grid is very small and fragile, it is hard to handle it in a glove box. Therefore this step requires long exposure of AgNP to air, which can cause oxidation of the AgNPs. Anisole is a rather non-polar solvent, and it is insoluble in water. However, it is miscible with ethanol and acetone (**Table 3.1**). This property allows easy phase-transfer of the grid from water to anisole, by first exchanging water with ethanol, and then ethanol with anisole, without long exposure to air, as well as complete removal of water on the surface of the NPs. v) Anisole is non-toxic, it has been used in the production of perfumes.

Miscibility of anisole

(Relative polarity*)	Water	Ethanol	Acetone	Anisole
Water (1)	■	miscible	miscible	Non-miscible
Ethanol (0.654)	miscible	■	miscible	miscible
Acetone (0.355)	miscible	miscible	■	miscible
Anisole (0.198)	Non-miscible	miscible	miscible	■

Table 3.1: Miscibility of anisole with commonly used solvents at room temperature. * The values for relative polarity are normalized from measurements of solvent shifts of absorption spectra and were extracted from (Reichardt. 2003).

3.1.2 Mounting Geometry

There are a number of practical issues with using anisole as a mounting medium. First, anisole readily dissolves the polymer film (e.g. Formvar) on the commonly used TEM sample grids. Silicon dioxide (SiO_2) and silicon nitride (Si_3N_4), on the other hand, are insoluble in anisole.

We therefore decided to use the SiO_2 grids. One of the difficulties for correlative imaging is that the commercially available grids with large aperture are supported by a holder and mesh with 4-fold rotational symmetry (square shape) (**Figure 3.1**), which makes it hard to determine the orientation of the grid when mounting it into a TEM sample holder. Furthermore, the grid is very flat and lacks any gross morphological features that can be easily recognised under TEM or a light microscope. A way to determine the orientation of the grid on the TEM holder is to recognise the distribution pattern of 3 or 4 NPs on the TEM imaging display, which usually has a maximum field of view of no more than 25 μm^2 at the lowest magnification for searching NPs below 100 nm in size. The optical measurements, on the other hand, usually require NPs on the substrate to be at a certain distance from each other, usually larger than 4 or 5 μm. These requirements make searching for the NPs of interest on the SiO_2 film difficult. In fact, this is a common problem of searching small objects of interest under TEM. In other reports (Song *et* *al*. 2011) grid finder or lithographic etched markers were used to aid this correlation process, which requires treatments on the TEM grid with specialised equipment. In our work, the SiO_2 film on the TEM grid was functionalised to avoid detachment of NPs and to preserve the distribution pattern. Immobilisation via settlement helped to control the NPs density on the film. Furthermore, coloured DF images of the sample grid and coordinates of the NPs measured on the DF images also help the correlation (as detailed below, see also **Chapter 2**).

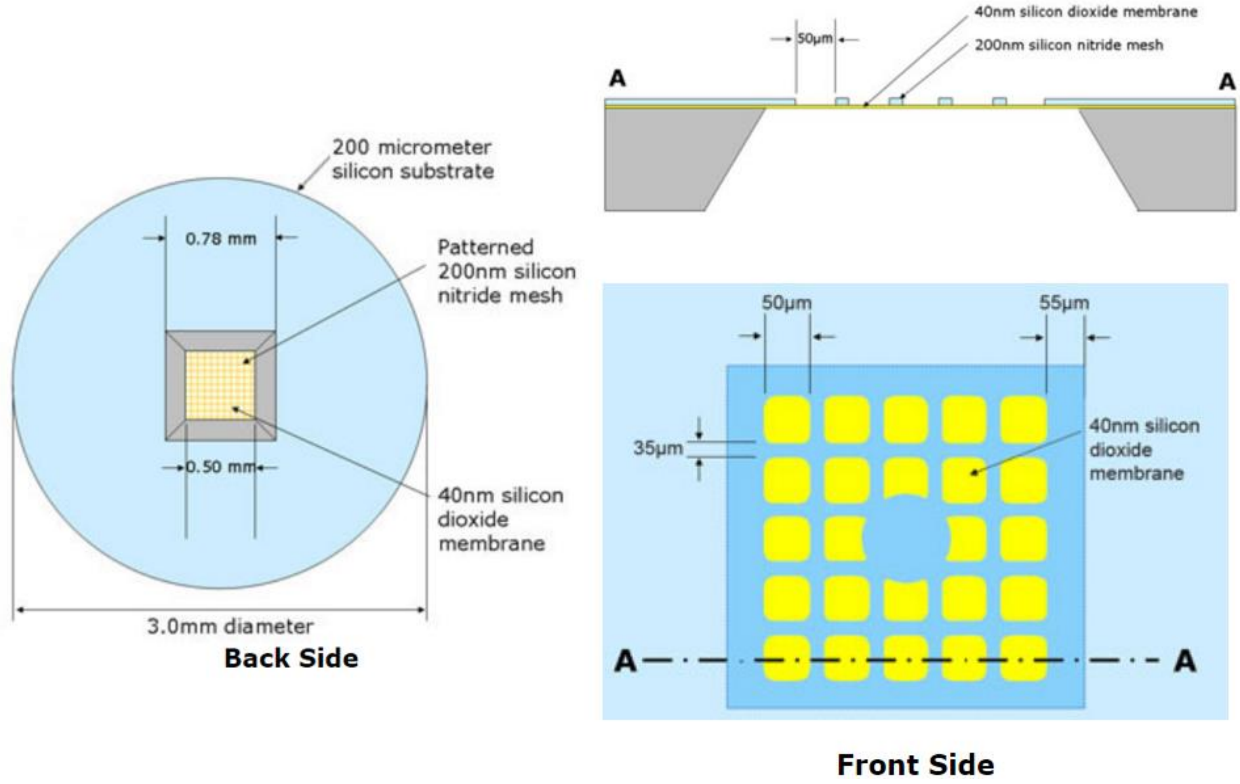

Figure 3.1 Schematic drawing of the silicon grid with silicon dioxide films (taken from the supplier TED PELLA, INC.)

The mounting medium anisole is relatively volatile at room temperature, as mentioned before. A small volume, typically <50 µL, used for mounting each sample slide can evaporate within an hour in air, while the optical measurements often take 4 to 5 hours. Hence, the sample grid has to be mounted and sealed in an airtight compartment. After optical measurements, the sample should be safely retrieved and dried without too much disturbance. For this purpose, a number of sealants were tested. Anisole was dissolving nail varnish and the glue on all of the duct tape tested. Solidified silicone sealant was insoluble in anisole, however, anisole could still evaporate from the slide sealed with such sealant possibly via the small pores on the solidified silicone sealant. Furthermore, it was hard to open the slide with this sealant without causing damage. Finally, a "*press-to-seal*" silicone isolator was used as a spacer to create a sealed chamber between the coverslip and the glass for accommodating the sample grid during the optical measurements. The isolator is insoluble in anisole. After soaking it in anisole for several hours and drying it completely, there were no changes in weight of the isolator, nor was any deformation of the isolator observed. Also no residual marks were noted, all of which indicates that the isolator is chemically stable in anisole. The isolator was cut to form a gasket, and sandwiched between a clean glass slide and coverslip to create a sealed chamber (**Figure 2.3. A**). There is no chemical adhesive on the isolator, instead, the isolator has an extremely flat surface to allow it to stick to a flat glass surface via van-der-Waals forces (weak, short-range electrostatic attractive forces between uncharged molecules). The overall adhesion force can be enhanced/reduced by increasing/decreasing the contact area between the glass and the isolator. Thereby, one can adjust the adhesiveness of the sealant by the size of the isolator used. Because the isolator is slightly elastic, any air bubble between the isolator and the glass surface can be removed upon pressing the glass against the isolator. Preliminary test (data not shown) showed that by simply laying down a mounted sample slide flat without applying any pressure over it, 90 μL anisole could remain in the sealed chamber for about an hour. After that, air bubbles started to grow within the chamber, as the anisole evaporated and leaked out through small passage between the isolator and the glass. In contrast, with applied pressure (by putting weight on the mounted sample slide), the anisole could remain in the chamber much longer, and there was no air bubble in the chamber observed after an overnight interval. All the optical measurements in this thesis used an oil condenser, which has to be in oil contact with the sample slide. The specimen clips on the sample stage limit the distances that the stage can move in the direction of the clips, prior to touching the condenser. Two small pieces of cleaved silicone isolator were also used to form a cage in the centre of the sample slide, to limit the movement of the sample grid during optical measurement (see **Section 2.1.7**).

A sample holder was designed to hold the sample slide with silicone isolator during the optical measurements (**Figure 2.3.B**). A standard glass slide (25 mm x 75 mm, Menzel Gläser) is cleaved into 25 mm x 25 mm square shape, to fit with an isolator (25 mm x 25 mm) and the coverslip (24 mm x 24 mm, Menzel Gläser). The mounted sample slide was placed in the centre of the sample holder over the circular stage opening, and a pair of specimen clips were used to press the sample slide against the edge of the stage opening, not only holding the slide in position during the measurements, but also helping to prevent the evaporation of the mounting medium; air bubbles started to form usually 3 to 4 hours after the start of the measurement. It is important to notice that the sample slide has to be placed right in the centre of the holder, the 4 corners of the sample slide need to be equally in contact with the metal recesses around the stage opening so that the pressure from the specimen clips is distributed evenly. Another silicon isolator was placed between the sample holder and the coverslip (**Figure 2.3 A**), which helped to protect the coverslip as well as to distribute the pressure from above. After mounting the sample holder with the slide onto the microscope, it usually takes 30 to 60 mins for the grid to settle down. Anisole has much less viscosity than silicone oil, therefore small mechanic vibrations on the sample stage can move the grid. It is important to make sure that there is no disturbance during the image acquisition.

After the optical measurements have been performed, the isolator with standard size can be easily peeled off from the sample slide. For mounting the sample grid in air, an isolator with smaller glass-contact-area should be used, this is because the lack of liquid solvent in the contact areas between the isolator and the glass can significantly increase the van der Waals force. The grid can then be taken off from the coverslip, dried in air and stored in a grid holder box in nitrogen gas. This mounting technique is also suitable for imaging samples deposited on a glass coverslip, rather than on a TEM grid, and allows imaging the same region on the coverslip in different mounting media (**Figure 6.19** in **Section 6.5**).

3.1.3 Grid functionalisation and NP immobilisation

Since all of the commercially available TEM grids have extremely thin and fragile films, drop casting is the most common and straightforward technique to immobilise NPs on a TEM grid (Michen *et al*. 2015). In this method, a small drop of NP solution is deposited onto a TEM grid, then the grid is dried in air and all the solutes are left on the grid afterward. There are a number of problems with using drop-casting in our correlative approach, as detailed in the following:

1) The commercially available carbon film or silicone film of TEM grids only bind the NPs weakly via limited number of hydrogen bonding (via methylenedioxy group and silanol group respectively). As described above, only silicone grid is compatible with anisole, and the availability of silanol group on the unmodified SiO_2 films is unlikely to be high. This is evidenced by the fact that a very small volume of water deposited onto a newly purchased silicone grid did not spread over the surface. Instead, it formed a droplet with large contact angle (data not shown). This indicates that the surface of the SiO_2 grid is very hydrophobic, which limits the interaction between the SiO_2 film and the NPs with a hydrophilic coating. The binding force for immobilising NPs on the unmodified SiO_2 film might be sufficient for TEM, as the electron beam can push the NPs against the film. However, when mounted in a liquid medium with low viscosity, such as anisole, NPs can easily detach from the film or change position, particularly during the drying steps as the capillary action can drag the weakly attached NPs. Since the distribution pattern of 3 to 4 NPs on the TEM imaging display is used for correlating the position on the DF map, it is crucial to retain the positions of the NPs on films throughout the whole experiment.

2) Drop-casting is likely to create large number of aggregates as well as debris from the solutes onto the grid. During the optical measurement step, a DF image of the grid was used to identify the NPs of interest. However, there is no geometrical information of each light scattering object on the grid available a priori (since TEM is performed afterwards), and isolated spots on the DF images are not necessarily correspond to a single NP. Small NP aggregates as well as a few NPs in close proximity, or small crystals attached to a large NP, might be smaller than the diffraction limit thus all appear as a single spot of the same size as for a single NP. This makes it more likely to select irrelevant aggregates or scattering objects during the micro-spectroscopy measurement of single NPs. This drawback is exacerbated if the NPs are not firmly attached to the film, and can lead to false correlation of TEM data with the spectroscopy data. Furthermore, the aggregates and debris also create a background when analysing the extinction images of the grid.

To overcome the above mentioned problems and firmly immobilise AgNPs on the SiO_2 film, the film was functionalised with APTES. The two-step reaction used was the same as the one used to functionalise a glass surface with silane (**Scheme 2.3**.) (Marques *et al*. 2013). In the first step the grid was incubated with an etching solution made of 5% (v/v) H_2SO_4 (diluted with 30% H_2O_2) at 65°C, to activate the silica surface by increasing the number of silanol groups on the SiO_2 film. Only 5% (v/v) of H_2SO_4 is used here since H_2SO_4 is a strong oxidative reagent and it is a viscous and sticky liquid at room temperature. Any residual H_2SO_4 on the film can readily oxidise AgNPs. Unlike a glass coverslip that can be vigorously washed with water then purged from the residual liquid with a stream of nitrogen gas after the etching step, a silicon grid can only be washed by serial dilution without stirring to lower the concentration of residual H_2SO_4 step-by-step. The lower is the concentration of H_2SO_4 used from the start, the easier is to remove it completely. The temperature was also reduced to avoid rupture and deformation of the SiO_2 film. In the 2nd step, the acid activated grid was incubated in 1% (v/v) of APTES in ethanol. It is important that fresh APTES is used (newly purchased or properly stored in a sealed anhydrous condition), because APTES can readily polymerise upon contact with water, forming large aggregates. Since the refractive index of APTES is close to anisole, they are hardly noticeable during optical measurements with anisole immersion, but they are highly disturbing in subsequent TEM imaging. Therefore, APTES stock must be centrifuged at high speed to precipitate the debris before it is dissolved in ethanol for functionalisation.

AgNPs were immobilised onto the APTES functionalised grid via settlement: A small drop (9 μL) of AgNP solution was carefully deposited on the grid, which was then placed in a sealed container with a humid tissue to reduce evaporation. After 15 mins incubation, the AgNP solution droplet was removed, and the grid was washed in water then dried in air under nitrogen gas, and ready to be mounted in the medium of choice. (**Figure 3.2 left**) compares DF images from an unmodified sample grid with drop cast silver dimers (from the AgNP-P1000DT solution, see **Section 2.1.1**), with dimers immobilised on an APTES functionalised silicone grid via settlement.

In the DF image of an unmodified sample grid with drop casted polymer-coated silver dimers, the majority of the spots appeared to be bright cyan and green in colour and formed clusters, suggesting that there are large numbers of small aggregates onto the substrate. Since the grid was not washed after the drop-casting step (to prevent detachment of the immobilised NPs), it is very likely that NPs are heavily coated with polymers (see **Section 6.1** for details on the dimer fabrication and polymer coating) that not only caused red-shifted of the NPs' plasmon resonance, but also prevented the NPs from getting too close to each other and form aggregates with very strong red-shift (the red dots on the DF image). The clusters might be the result of capillary action during drying of the grid. All these features make this sample grid unsuitable for optical measurements. In contrast, the DF image of AgNP-P1000DT immobilised on a APTES functionalised silicone grid via settlement (**Figure 3.2 right**) showed a much more even distribution of the spots, and there was a variety of colours, with the majority of spots appearing to be blue, suggest that they are isolated AgNPs. Since the grid was washed in water for 3 times, most of weakly bound solute/NPs on the grid were washed away and there was no coating over these NPs; the remaining immobilised NPs were stable through 5 hours measurement session. The washing step might remove some of the polymer coating and make the AgNP more prone to oxidation in air, so it is advisable to finish all the optical measurements in one session after mounting the sample grid onto the microscope. However, we did not observe significant spectral changes after re-mounting the sample grid which was stored under nitrogen at 4°C for 2 weeks; perhaps the strong Ag-thiol bonding retained a layer of polymers that was sufficient to prevent oxidation of the AgNPs.

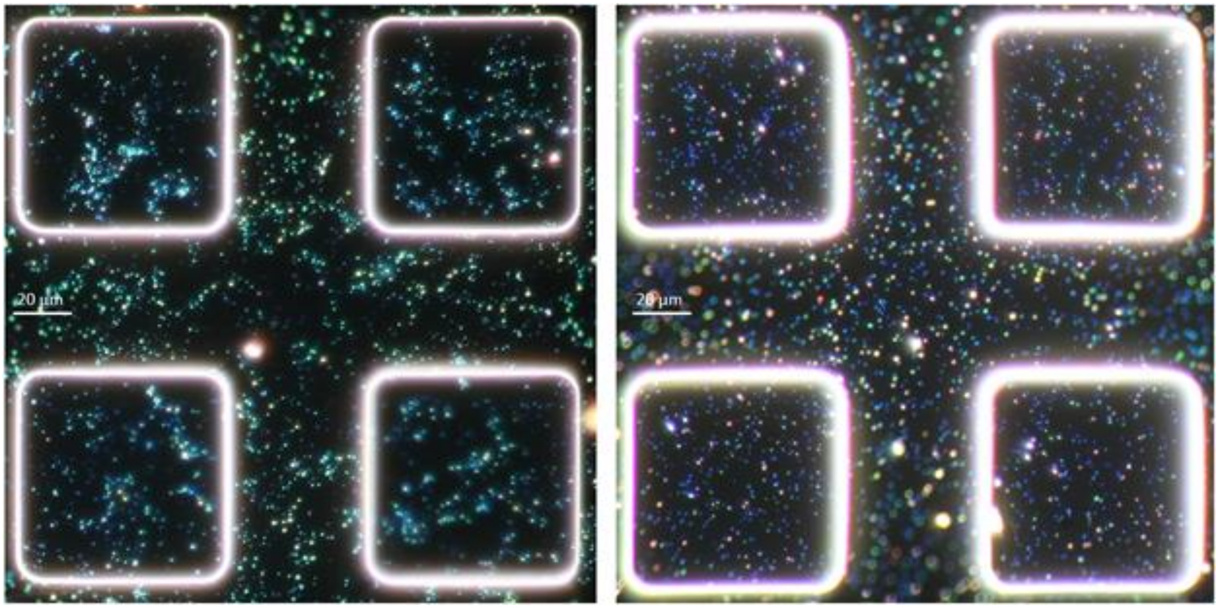

Figure 3.2 DF images of the sample grid prepared with different NP immobilisation methods and mounted in anisole after drying. **Left)** 9 µL of OD_{400nm} = 1 x 10^{-2} AgNP-P1000DT reaction solution was drop-casted onto an unmodified SiO_2 grid. **Right)** NPs in 9 µL of OD_{400nm} = 3 x 10^{-2} the AgNP-P1000DT reaction solution were settled onto an APTES functionalised silicon grid.

As further example shown in (**Figure 3.3**) the BF images of the 75 nm Ag cubes (described in Chapter 4) on an APTES functionalised silicone grid, before (**Figure 3.3 left**) and after (**Figure 3.3 mid**) TEM measurement. Both images were acquired with the sample immersed in anisole. Every light absorbing NP in this field of view remained in its position before and after TEM measurements, even for the NPs imaged with high current density under TEM (NP with the burn mark). There were a small number of extra light absorbing objects that appeared after acquisition of the first image, those are likely to be dust/dirt deposited on the film after first BF image, and they were easily recognisable under TEM.

The developed APTES functionalisation and the immobilisation-by-settlement technique of the substrate thus not only helps to improve sample conditions (since the status of the NPs more closely resemble that in solution, in comparison with mounting by drop-coasting), but also ensures that the immobilised NPs remain in their position on the grid throughout the correlative imaging procedure.

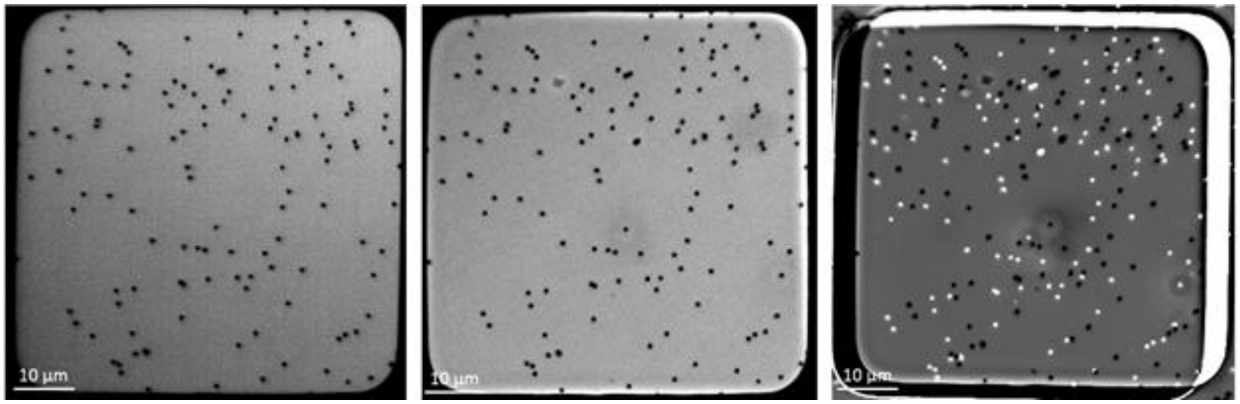

Figure 3.3 BF images of the 75 nm Ag cubes settled on an APTES functionalised silicone grid. Before (**left**), after (**mid**) TEM measurement and the extinction image after TEM (**right**). The sample grid was mounted in anisole.

3.1.4 NP density.

Using the immobilisation-by-settlement technique, a good control of the NP density on the SiO_2 film is achieved, which is critical for any correlative imaging approach. The density of the NPs on the film is determined by multiple factors, such as the concentration as well as volume of the incubating NP solution, the chemistry of the coating of the NPs as well as the temperature and the length of incubation time. Although we did not test how the NP density change with the incubation time, 10 min should be sufficient for strong interactions between most of NP and the substrate to take place, since only small volume (9 µL) of diluted NP solution were used over a 0.25 mm^2 area of substrate. The NPs immobilised with weak binding force should be washed away in the subsequent steps. **Figure 3.4** shows that, while keeping other factors constant, the NP surface density increases linearly with the NP volume concentration of the incubating solution.

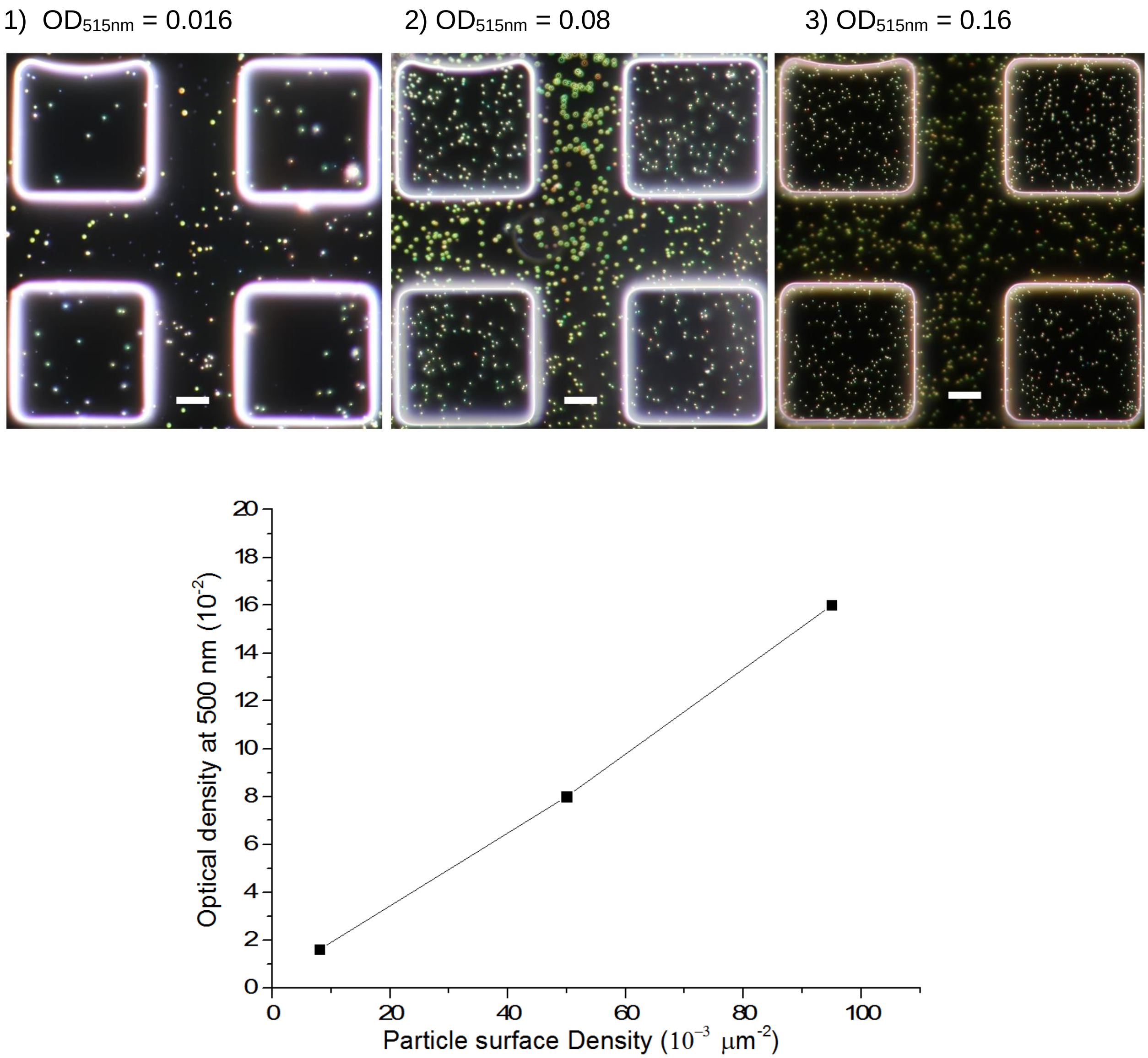

1) OD_{515nm} = 0.016 2) OD_{515nm} = 0.08 3) OD_{515nm} = 0.16

Figure 3.4: Upper panel: DF images (anisole as mounting medium) of the functionalised sample grids prepared with various concentration of 75 nm Ag-cube incubating solution for settlement in water: **1)** 9 μL of OD_{515nm} = 0.016 (5.8 x 10^7 NP/mL) **2)** 9 μL of OD_{515nm} = 0.08, (2.9 x 10^8 NP/mL) **3)** 9 μL of OD_{515nm} = 0.16. (5.8 x 10^8 NP/mL)The number of NPs in each SiO_2 cell (A = 2.5 x 10^3 μm^2) were counted by imageJ and the density was calculated as **1)** 8.3 x 10^{-3} μm^{-2}, **2)** 50.1 x 10^{-3} μm^{-2} **3)** 95.0 x 10^{-3} μm^{-2} and plotted in the figure shown in the lower panel. Scale bar: 20 μm

Our methodology for quantitative micro-spectroscopy (**section 2.2.4**) requires to integrate the transmitted light intensity over an area A = 1 μm^2 for the 40x objective and A = 2 μm^2 for the 20x objective. For referencing it also requires an empty area of similar size close to the NPs of interest. Each NP therefore should be in isolation within a minimum area of 2 μm^2 for the 40x objective and a minimum area of 4 μm^2 for 20x objective, i.e. the maximum NP density that can be used is 500 $x10^{-3}$ μm^{-2} for 40x objective and 250 x 10^{-3} μm^{-2} for 20x objective if all NPs were evenly spaced. Ideally, a NP density about a quarter of these values should be used to avoid any interference from adjacent NPs, namely $125x10^{-3}$ μm^{-2} for 40x objective and $83x10^{-3}$ μm^{-2} for 20x objective. On the other hand, for TEM imaging, 2500x is the minimum magnification required to see the 75 nm Ag-cube on the imaging display (the field of view of the attached CCD camera) without using a too long exposure (which causes delay while moving the grid) or high current intensity (which causes damage). The size of the TEM image at this magnification is 79.2 μm^2 (**Figure 3.5 left**). Ideally 3 or 4 NPs should be present in the same field of view at this size, whose distribution pattern was used to identify NPs of interest. Therefore, for this requirement of searching NPs on TEM, the minimum NPs density is (1/79.2) x 3 = $37.9x10^{-3}$ μm^{-2}. In practice, also considering that the distribution of NPs on the grid is not perfectly even, a NP density of $95x10^{-3}$ μm^{-2} was used for the correlative approach, which satisfies both requirements of NP density sufficiently low for optical imaging of isolated NPs and sufficiently high to provide enough NPs in the TEM field of view for pattern recognition.

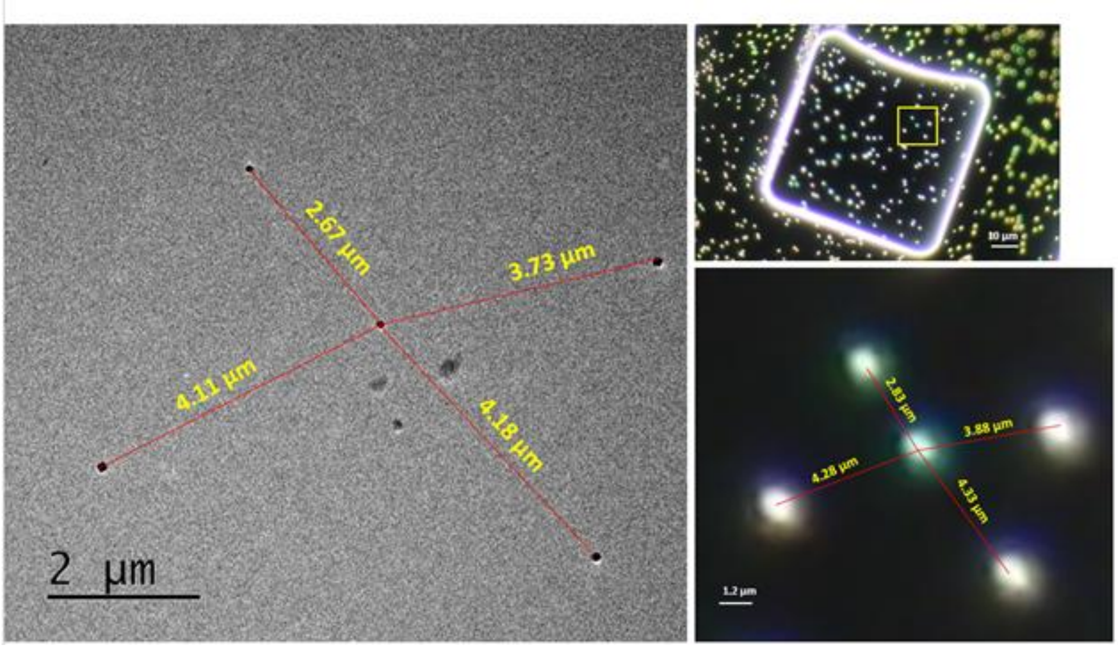

Figure 3.5. Left) The full image taken by the CCD camera attached to the TEM with 2500x magnification. The distances (red lines) between the NPs on the image were measured with imageJ (yellow numbers). **Right)** the DF images of the sample grid before TEM were taken by the Canon colour camera. The interparticle distance (red lines) were measured from the images by imageJ (yellow numbers).

Chapter 4. Silver Nanocubes: Results and discussion

In the previous Chapter, a novel correlative image technique was developed. In this Chapter, as proof-of-concept to show the importance of correlative studies of the optical properties of single NPs. The flexibility of the experimental technique was also demonstrated here: the correlative image technique along with the quantitative measurement protocol (developed by Dr. Attilio Zilli, details in **section 2.2.4 and 2.3.2**) were implemented together to obtain the optical cross section spectra in absolute nm^2 units of individual 75 nm Ag nanocubes; such optical measurement can be carried out with NP in different dielectric environments. The experimental technique is also compatible with 3D tomography HR-TEM imaging, the geometrical information of the imaged Ag nanocubes were then used for electromagnetic simulations with COSMOL (developed by Dr Attilio Zilli and performed by the MSc student Zoltan Sztranyovszky, from Cardiff School of Physics and Astronomy), which are shown here for completeness.

4.1 Correlative imaging of Ag-cubes.

75 nm edge size Ag-cube were purchased from nanoComposix Inc (USA). The Ag-cubes are coated with 55k Da polyvinylpyrrolidone (PVP), and suspended in ethanol with -20 mV Zeta potential. They are provided at a silver mass concentration of 1.06 mg/mL, corresponding to a particle concentration of 2.1x10^{11} particles/mL resulting in an OD (absorbance of the beam of light through 1 cm path length of the sample) at 515 nm (in ethanol) of 58. The edge size measured by TEM for the batch provided is 78±5 nm (as specified in the batch data sheet from the manufacturer). As discussed in Chapter 1, the LSPR extinction cross-section of a MNP depends not only on the particle size and shape but also on the environment's refractive index (Genzel *et al*. 1975), (Davletshin *et al*. 2012b). **Figure 4.1** shows absorbance spectra of the Ag-cube stock diluted in different solvents. When suspended in water (n = 1.33), three LSPR peaks were observed at 505 nm, 447 nm and near 380 nm within the spectrometer range (380 nm to 900 nm), whereas in anisole (n = 1.51) all three LSPR peaks were red-shifted to 549 nm (referred as P_a), 481 nm (referred as P_b) and 400 nm (referred as P_C). As also mentioned in Chapter 1, by comparison with a spherical AgNPs (**Figure 6.10** in **Section 6.3**), the Ag cube has several distinct symmetries for dipole resonance, also there are quadruple and higher resonance for 75 nm Ag-cube, hence exhibits more peaks (Fuchs 1975). The most intense

peak (P_a) is also the most red-shifted peak, which can be attributed to a dipole resonance excitation at sharp corners (Sherry *et al*. 2005. Haes *et al*. 2005). Calculations of the nearfields around silver nanowires with a square cross section show that surface charges accumulate at sharp corners (Kottmann *et al*. 2001). This segregation of charges into corners increases charge separation and decreases the restoring force for the electron oscillation, hence lower the dipole resonance frequency. LSPR peaks P_b and P_C might result from a quadrupole contribution which is significant for Ag cubes of edge length >50 nm (Zhou *et al*. 2008). The spectrum of Ag-cubes suspended in anisole (red-line) represents the ensemble-averaged spectrum for single Ag-cubes in a homogeneous environment (n=1.51). These Ag-cubes have a narrow size and shape distribution, as indicated on the manufacturer's batch data sheet (standard deviation of edge size = 5 nm; coefficient of variation: 7%). It is important to note that PVP is insoluble in anisole, thus flocculation can take place as the result of an entropic effect. The rate of this flocculation should be the highest shortly after injecting the highly concentrated Ag-cube stock into anisole for dilution, which explains the lower absorbance of Ag-cube in anisole than that in water, and a red-shifted aggregation peak in the 600 to 800 nm region formed. Once the remaining Ag-cubes were suspended in anisole, they underwent slow flocculation after being diluted in anisole, with a slow spectral change, that only became noticeable after 15 mins.

As described previously (see Chapter 2 and 3), diluted Ag-cubes in solution (9 µL of OD_{515nm} = 0.16) were settled on an APTES functionalised silicone grid, which was then mounted in anisole. The coloured DF image of the grid was taken. As suggested in **Figure 4.1,** the average single Ag-cube has the strongest LSPR peak near 550 nm in anisole, thus Ag-cubes should appear as a green spots on the DF image (**Figure 4.2**). Generally, microspectroscopy measurements for both scattering and absorption spectra were performed on 5 to 10 isolated NPs (at least 2 µm away from other scattering objects) in each window (**Figure 3.13 left column)**. Their positions were marked on the DF images, and the coordinates of these positions were later measured on the DF image by imageJ (see the **Section 2.2.4** for detail). After optical measurements, the sample grid was de-mounted and retrieved, dried in air under nitrogen gas for 10 mins and then mounted in air to study the effects of the dielectric environment on the optical extinction spectra of Ag-cubes.

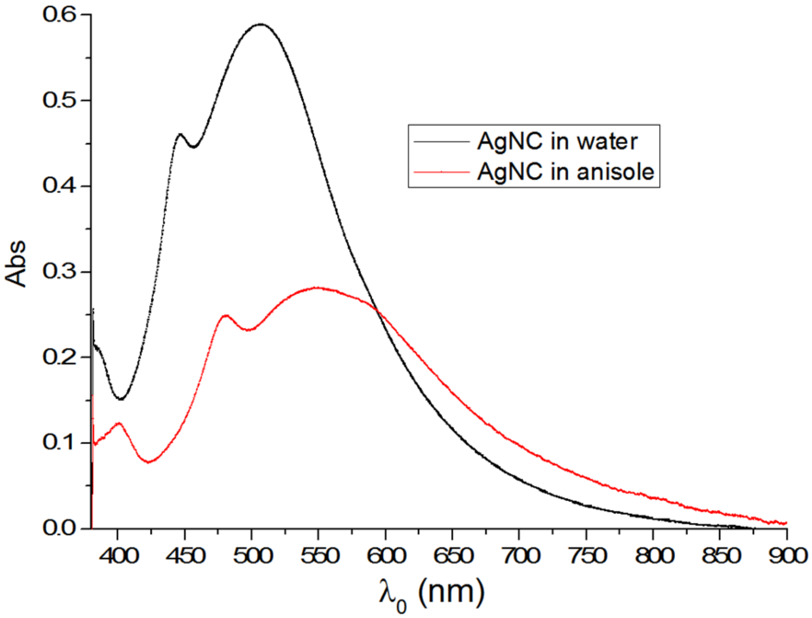

Figure 4.1 Spectra of diluted 75 nm Ag-cube solution: the purchased stock was first diluted with water (1:10); 30 μL of this stock was mixed with 270 μL of water (**black line**) or anisole (**red line**) in a glass cuvette for 10 seconds before taking the spectra.

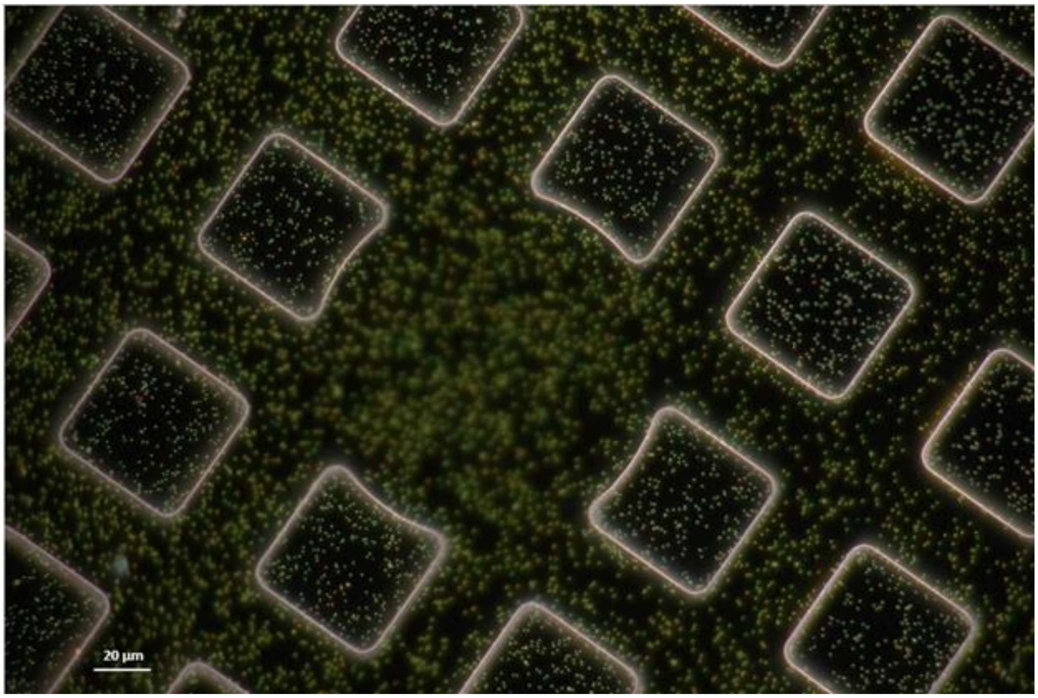

Figure 4.2 DF image of 75 nm Ag- cubes settled on an APTES-functionalised SiO_2 film and mounted in anisole.

The sample grid was first mounted in air in the same orientation, i.e. with the film on the coverslip side, as in anisole (**Figure 4.3 A**). However anomalous scattering patterns and interference fringes were observed on the DF images and extinction images respectively. This is likely to be due to the fact that some parts of the SiO_2 film were physically in contact with the supporting coverslip. These optical artefacts were unpredictable and compromised the optical measurements if the NPs of interest were on or close to the patterns (**Figure 4.3 B**). Furthermore, the SiO_2 film was more susceptible to physical damage if a large area of it was stuck onto the coverslip. To avoid these issues, the sample grid was mounted in the upside-down orientation when imaged in air. (**Figure 4.3 C and D**) show that when the SiO_2 film and NPs were far away from the coverslip, the artefacts were not observed on both DF and extinction images. In anisole, NA > 1 can be used in the excitation with the oil condenser, but this would lead to total internal reflection from the glass to the air. Therefore the DF ring in air had to be between 1 and the $NA_{obj} = 0.75$ to achieve DF with illumination of NA <1. On the DF images of the grid in air, the dark background (i.e. the contrast observed in regions away from the NPs) is significantly brighter (ideally there should be no scattered light away from the NP) than that for the grid in anisole. This is because the DF stop was closer (0.8 to 0.9 NA) to the 0.75 NA of the 20x objective) to block all the light directly from the lamp; a slightly larger DF patch-stop would narrow the NA range and improve the background of the DF images as well as the spectroscopy measurements. Nevertheless, due to the strong scattering cross-section of 75 nm Ag-cubes in air, the signal was sufficient to allow us to search and acquire the spectra of NPs of interest on the SiO_2 film (**Figure 4.5 mid column**). However, for NPs with weak scattering cross-section such as 50 nm edge-size Ag decahedron, this mounting geometry might not be suitable (data not shown). Furthermore, the orientation of a NP with asymmetrical shape determines how the NP interacts with light from a fixed direction of incidence, hence the spectral data measured with different mounting orientations might not be comparable directly without a comprehensive understanding of the optical properties of the NPs through computational modelling.

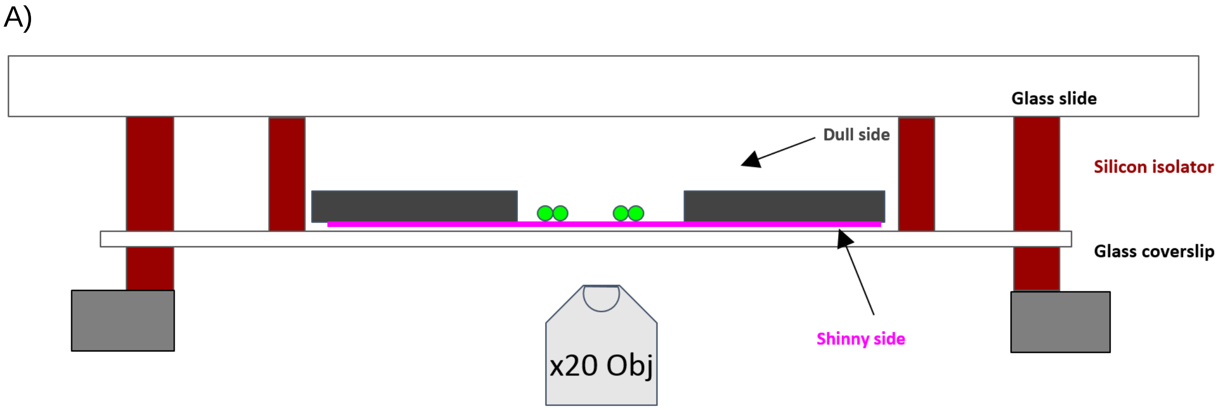
A)
Glass slide
Dull side
Silicon isolator
Glass coverslip
Shinny side
x20 Obj

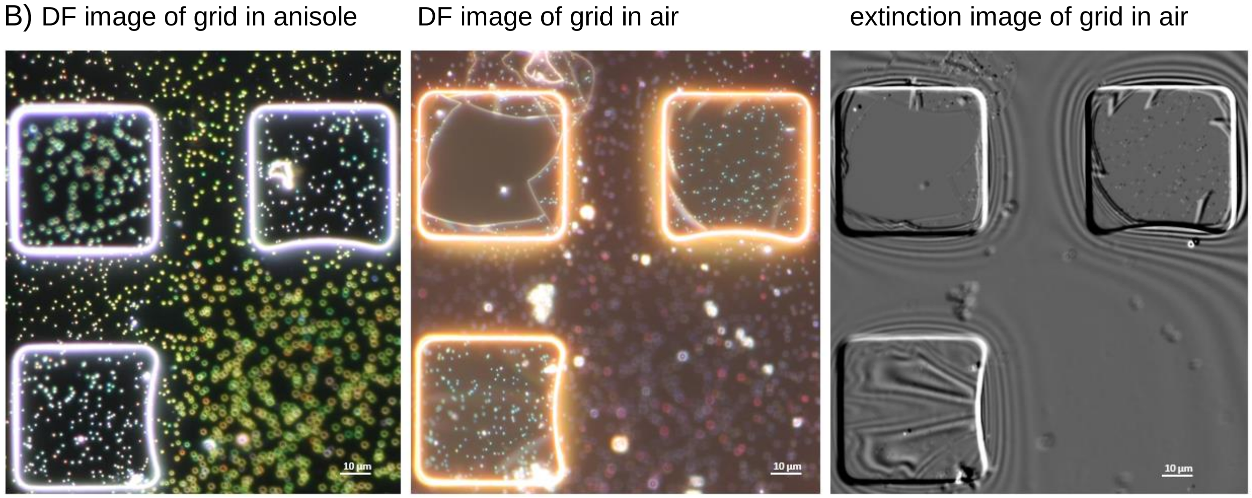
B) DF image of grid in anisole
DF image of grid in air
extinction image of grid in air
10 µm
10 µm
10 µm

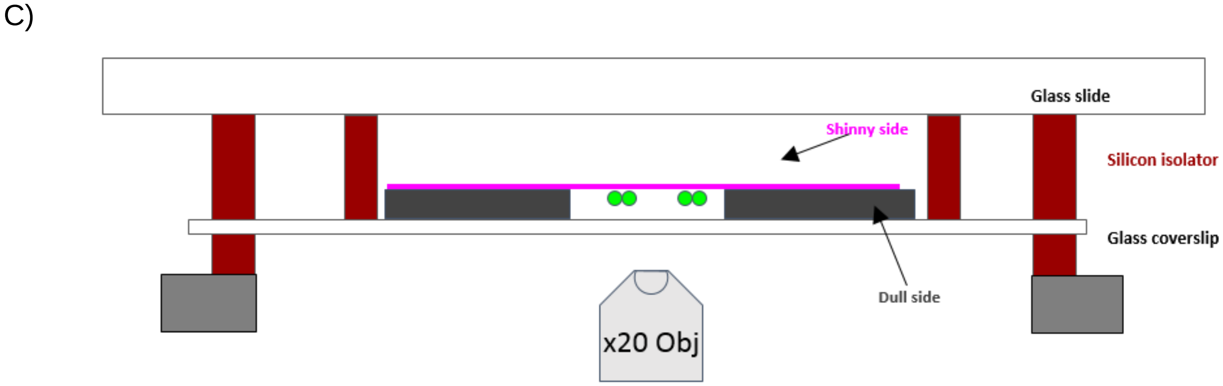
C)
Glass slide
Shinny side
Silicon isolator
Glass coverslip
Dull side
x20 Obj

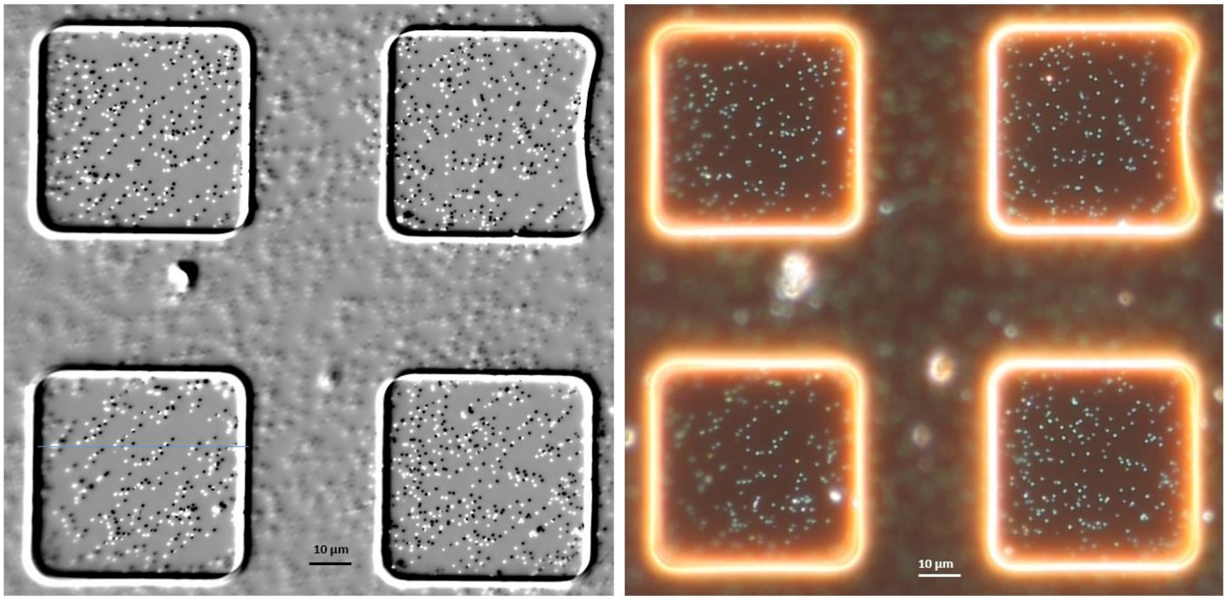
D) Extinction image of grid in air

DF image of grid in air

Figure 4.3 A) Schematic illustration (cross-section view) of the standard mounting geometry for the optical measurements of sample grids in anisole. **B**) The standard mounting geometry was used to obtain a DF image of the grid in anisole (left), a DF image of the grid in air (mid) and an extinction image of the grid in air (right). **C**) Schematic illustration of the upside-down mounting geometry for the optical measurements of sample grids in air. **D**) The upside-down mounting geometry was used to obtain an extinction image of the sample grid (left) and a DF image of the sample grid (right).

For the optical imaging step, as described in **Section 2.2.4**, a set of five different signals were acquired, which are proportional to the corresponding powers (P_{DF}, P_{BF}, P_{back}, P_{lamp} and P_{dark}) for each candidate NPs on the grid. The absorption and scattering cross-section spectra in absolute units were then calculated by **eq 2.16** and **eq 2.17** respectively (details in **Section 2.3.2**). The parameters for the calculation were computed analytically on MATLAB, yielding: for the spectra of NPs in anisole: $\xi = 1.54$, $f_{BF} = 0.140$, $f_{DF} = 0.112$ and $\zeta = 0.981$; for the spectra of NPs in air: $\xi = 6.43$, $f_{BF} = 0.0893$, $f_{DF} = 0.0705$, $\zeta = 3.41$.

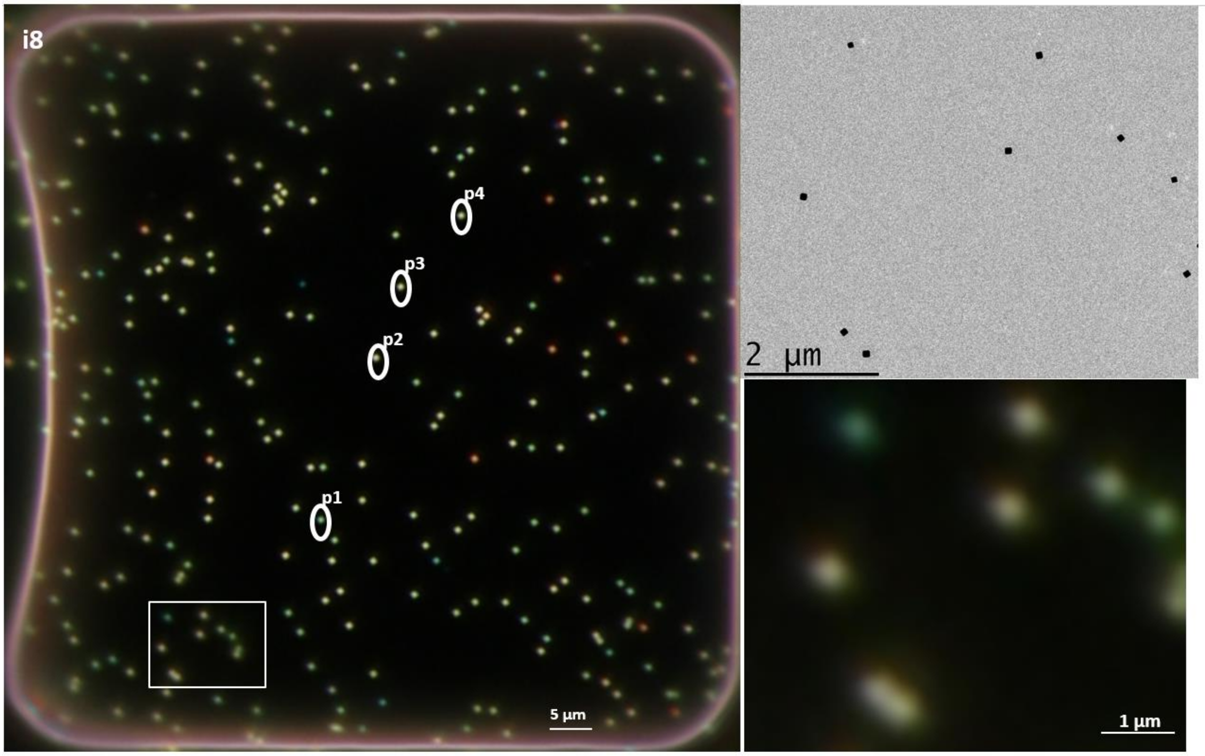

Figure 4.4 Left: DF image (anisole as mounting medium) map of the SiO_2 region with NPs of interest marked with white circles. **Right**: the distribution pattern of the NPs on the TEM images (upper panel) was correlated with that on the DF map (lower panel).

As described in **Section 3.1.4**, thanks to the DF image map (**Figure 4.4**) and the NP coordinates derived from it, NPs of interest were found and correlated under TEM, i.e. HR-TEM images (**Figure 4.5**) of the same NPs identified in DF were acquired. On the DF image map, about 10 % NPs appeared red in colour. Many of them are likely to be aggregates of Ag-cubes or AgNPs with different shapes. One of the red dots that had distinctive spectral features at various in-plane linear polarisation angles (**Figure 4.6 B**) was selected for correlative imaging. The projection of the NP on the TEM micrograph suggests that the NP is likely to be a right-triangular bipyramid reported in literature (Zhang *et al*. 2009. Very small number of bipyramid projection can also be found on the sample data sheet from the supplier, indicates that these are by-product of the colloid synthesis (**Section 1.4**). This finding demonstrates the applicability of the correlative imaging techniques: Without proper correlation at single NP level, one would not be able to eliminate the speculation that the red dots can be aggregates, cube dimers or dielectric debris. Our techniques allow identification of NPs with interesting spectra.

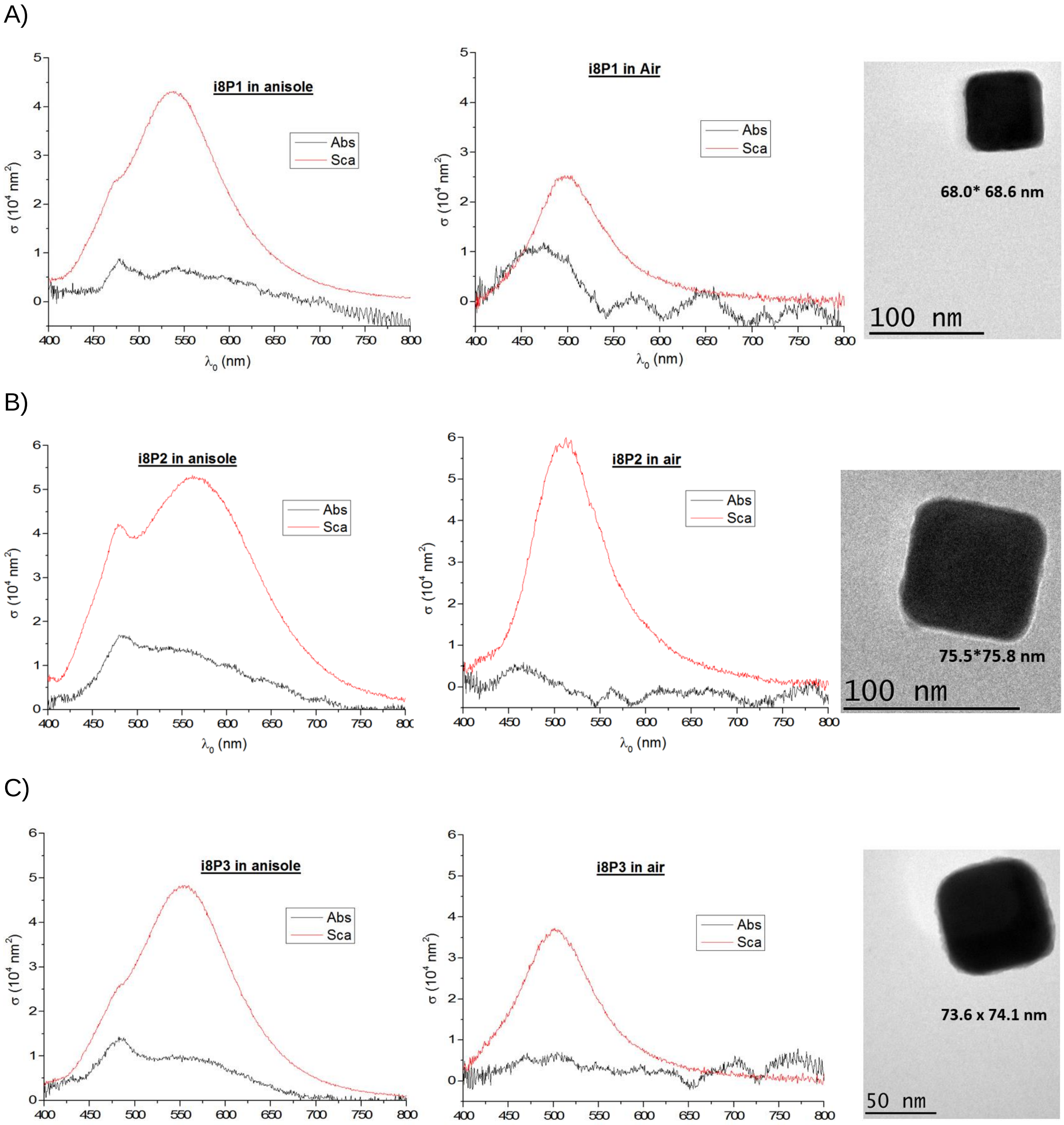
A)
i8P1 in anisole
Abs
Sca
σ (10^4 nm^2)
λ$_0$ (nm)
i8P1 in Air
Abs
Sca
σ (10^4 nm^2)
λ$_0$ (nm)
68.0* 68.6 nm
100 nm
B)
i8P2 in anisole
Abs
Sca
σ (10^4 nm^2)
λ$_0$ (nm)
i8P2 in air
Abs
Sca
σ (10^4 nm^2)
λ$_0$ (nm)
75.5*75.8 nm
100 nm
C)
i8P3 in anisole
Abs
Sca
σ (10^4 nm^2)
λ$_0$ (nm)
i8P3 in air
Abs
Sca
σ (10^4 nm^2)
λ$_0$ (nm)
73.6 x 74.1 nm
50 nm

D)

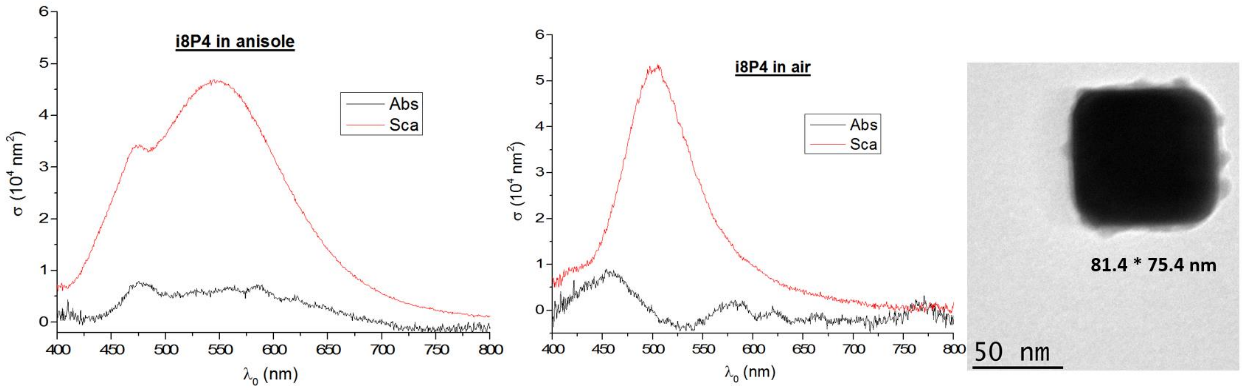

Figure 4.5 Correlative imaging of 75 nm edge Ag-cubes on SiO_2 film: quantitative scattering / absorption spectra of 4 Ag-cubes were first acquired with sample immersed in anisole (**left column**). Quantitative scattering / absorption spectra of the same NPs were then acquired with sample in air (**mid column**). High-resolution TEM images of the same NPs were acquired at 80 000x magnification (**right column**).

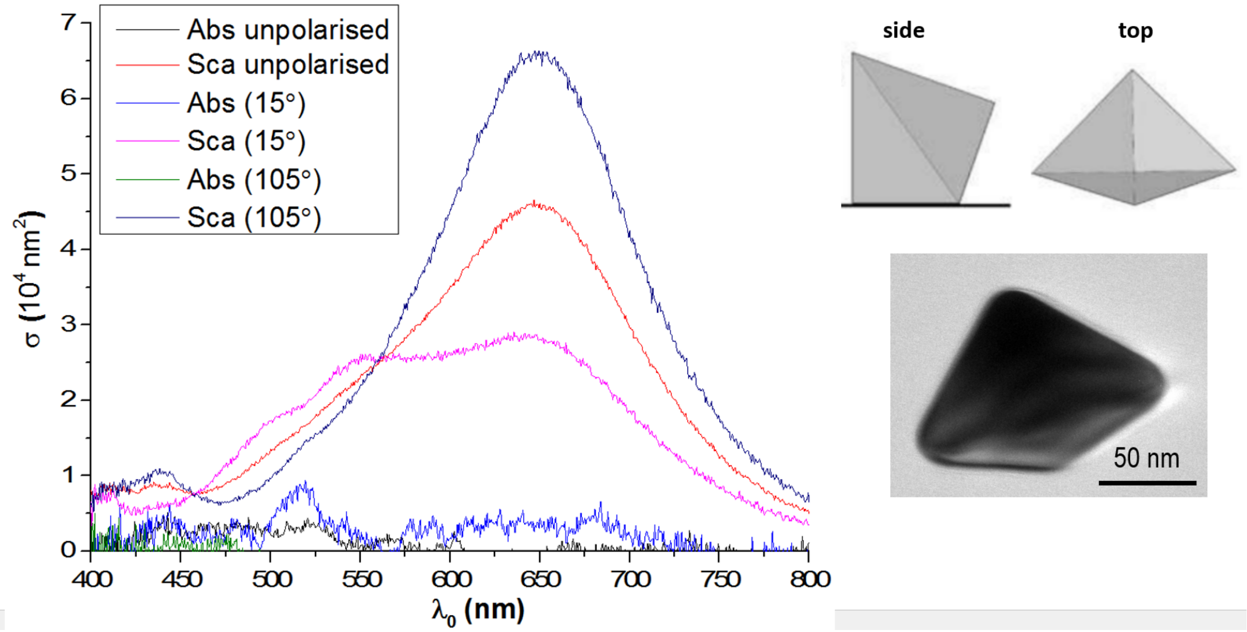

Figure 4.6. A) Left: DF image of the SiO_2 region with NP labelled as o15pA (red square); **Right:** TEM micrograph of the same region. **B**) **Left:** quantitative scattering / absorption spectra of the red dot, **Right upper panel**: 3D model of a right triangular bipyramid, adapted with permission from (Zhang *et al*. 2009). Copyright 2009 American Association for the Advancement of Science. **Right lower panel**: HR-TEM images of the NPs were acquired at 80 000x magnification.

For acquiring 3D TEM images of NPs, the sample grid was mounted on the TEM EM-21010/21311 HTR holder, which allows maximum +70° and -70° tilting over the Y axis. An Ag-cube (**Figure 4.5 B)** in the centre of the SiO_2 window was selected to avoid the incident electron beam being blocked by the silicon frame of the grid. Preliminary data showed that with low electron current density on the imaged area, the sample grid could be tilted from +50° to -50° without tearing the SiO_2 film or moving the NP on the substrate. Further increasing or decreasing tilting angle resulted in blockage of the electron beam by the frame of the TEM grid.

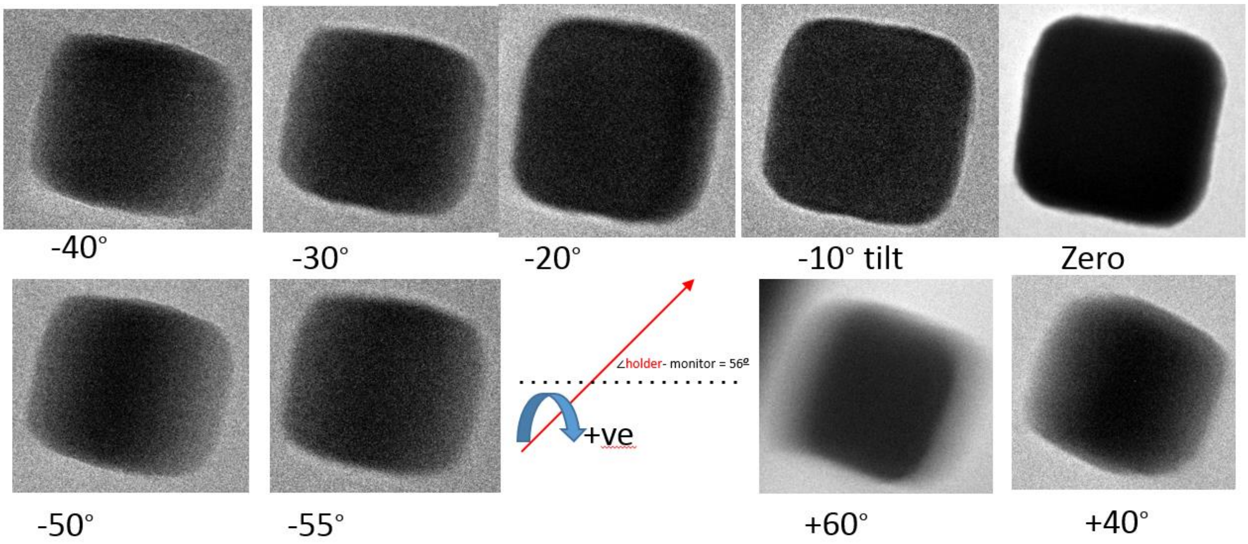

Figure 4.7 Preliminary 3D tomography imaging of an Ag-cube. The red arrow is the tilt axis; the dotted line is the x-axis of the TEM image. For image acquisition with the attached CCD camera, an electron current density of 40 pA/cm^2 was used when the holder was tilted. Up to 120 pA/cm^2 can be used when the holder was not tilted. The CCD camera exposure time was set to the lowest value (0.1s) due to drifting,

4.2 Data analysis with computational modelling

EM simulation has become an essential tool for theoretical studies to understand how optical properties of NPs depend on size, shape, and local environment. The finite element method (FEM) is one of the most popular numerical approaches (Jin 2014). It is essentially a mathematical algorithm to discretize and solve partial differential equations. In comparison with other numerical approaches such as DDA and the finite-difference time-domain (FDTD), it is flexible for handling irregular geometries and fine features within large domains, it also can approximate more accurately curved surfaces (such as rounding of the corner) and be selectively refined in specific areas of interest.

A computational modelling framework was developed by Dr. Attilio Zilli with the commercial software COMSOL Multiphysics, which implements the FEM, and was used by the MSc student Zoltan Sztranyovszky (Cardiff School of Physics and Astronomy) to reproduce the experimental data shown in this Chapter. The mounting geometry (**Figure 4.3**), the illumination setup (**section 2.2.4**) and the structural information of the imaged Ag nanocubes (**Figure 4.5)** were used as input for the simulation. As an example, the calculated spectra of the Ag-cube labelled i8P2 in air and anisole are presented (**Figure 4.8**) along with measured spectra.

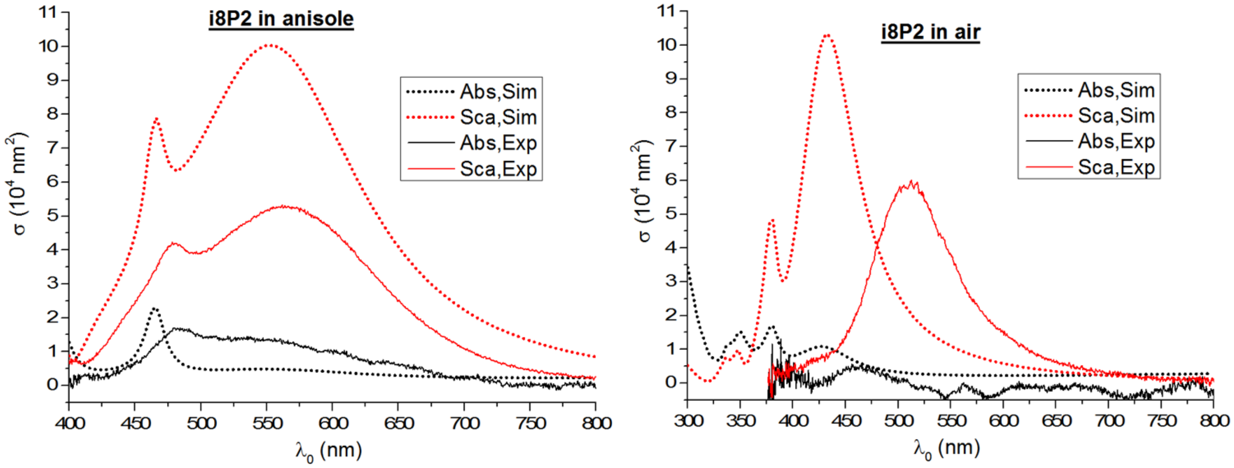

Figure. 4.8 Absolute absorption and scattering cross section spectra of Ag-cube i8P2 in air (n= 1.00) (**black lines**) or anisole (n = 1.51) (**red lines**). **Solid lines** are experimental data and **dashed lines** are simulations.

For the spectra of the Ag-cube in anisole, the position scattering dipole peak (550 nm) and quadrupole peak (475 nm) are consistent between experiment and simulations. For the spectra in air, the position scattering dipole peak (510 nm) of the observed spectrum is significantly red-shifted. One possible explanation for this discrepancy is that the imaged Ag-cubes here are thought to be coated with PVP (40k). Because the thickness of the PVP is unknown (unable to measure with available techniques), it was not taken into account in the simulation. PVP has a refractive index of n = 1.52 (Konig *et al*. 2014), which is close to the refractive index of anisole (n = 1.51). Therefore, the PVP coating has no significant effects on the spectra of Ag-cube in anisole. However, when imaged in air (n = 1.00), the PVP coating can cause a significant red-shift of the spectra of the Ag-cube

Chapter 5. Plasmon Mediated Fabrication

5.1 Plasmon Mediated fabrication and purification

Preliminary work was carried out with Dr. Iwan Moreels' group at the Istituto Italiano di Tecnologia (IIT) in Genova, Italy, as part of a one month internship during my PhD. The seeds were fabricated as described in the procedure **section 2.1.2**, and the yellow coloured seeds colloidal solution (**Figure 5.1 B1**) was transformed into orange, purple or blue colour (**Figure 5.1 B2-5**) after overnight irradiation with 470 nm, 505 nm or 625 nm LEDs respectively, indicating the formation of various plasmonic NPs. The product solution from 470 nm irradiation (only) shows multiple scattering by its milky appearance, indicating is contains particles with larger volume that scatter efficiently (**Figure 5.1 B5**). Preliminary test showed the concentrations of silver nitrate, PVP or citrate by a factor of 0.5 or 2 during the seeds fabrication had no significant effect on the colour transformation in the irradiation step. This is consistent with the reports in literature (Langille *et al*. 2013). On the other hand, increasing the concentration of sodium borohydride by 2-fold or not using the freshly prepared sodium borohydride resulted in the solution been transformed into black colour (data not shown).

A)

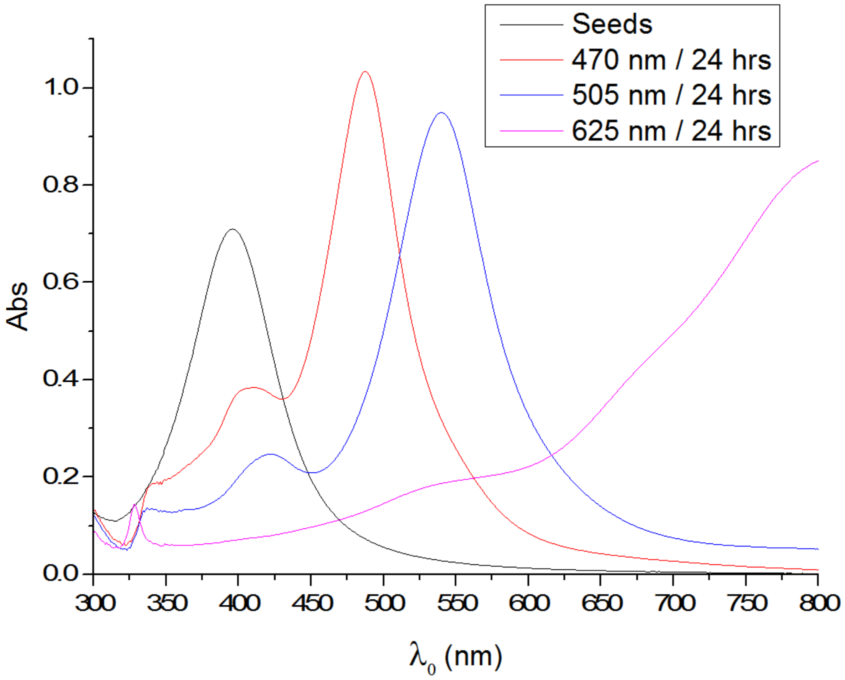

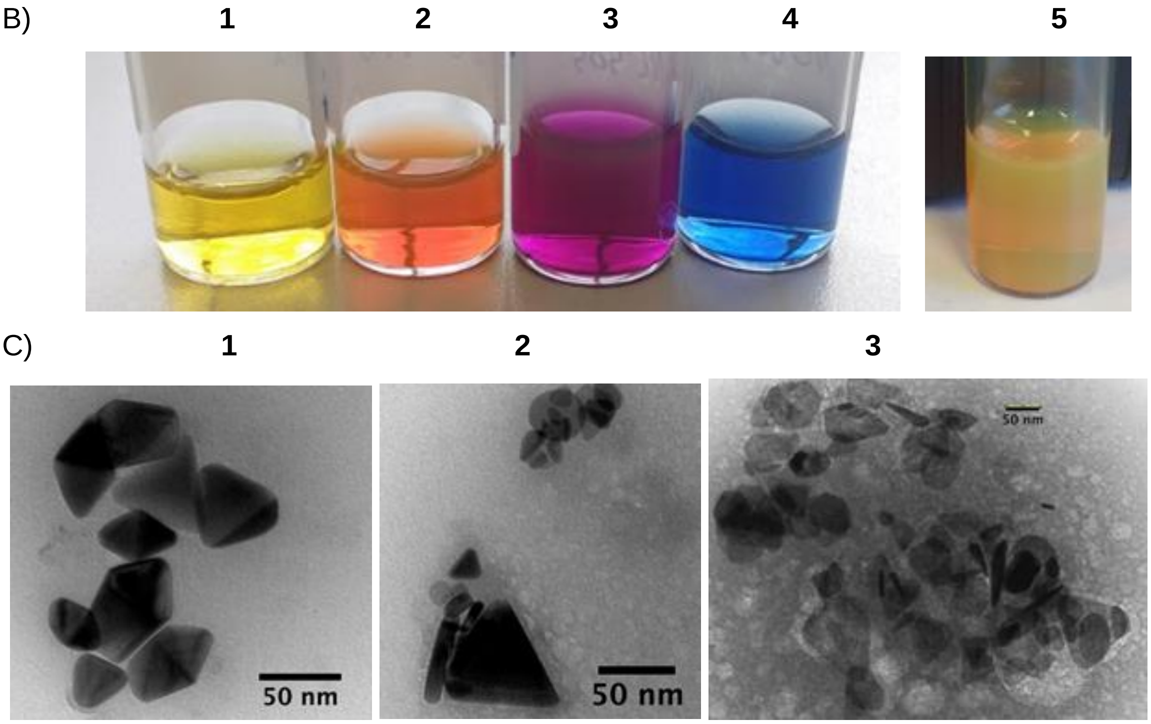

Figure 5.1. Plasmon-mediated fabrication at IIT **A**): UV-Vis absorption spectra of the seeds solution, and the product solutions from irradiation with different LED. **B**): visible colour photo of the seed solution (**1**) and product solutions after irradiation (**2**-**5**). Note that, for (**1**-**4**) large portion of light was transmitted from the back of the solution, whereas (**5**) showed the reflective light (multiply scattered) from the solution. The seeds solution were irradiated with the 470 nm LED (**2** and **5**), 505 nm LED (**3**) or 625 nm LED (**4**) at their maximum output power for overnight at room temperature (section 2.1.2). **C**). HR-TEM micrographs of the dried product solutions from **1**) 470 nm irradiation (product solution B2 and B5) **2**) 505 nm irradiation (product solution B3) and **3**) 625 nm irradiation (product solution B4), drop-casted on silicon nitride TEM grids.

The absorption spectra of the product solutions and representative TEM micrographs of the NPs in a diluted product solution are shown in **Figure 5.1 C**. The product solution with blue colour (irradiated at 625 nm) has a broad absorption, apparently having a peak above 800 nm. The TEM micrograph shows that it contains very large nano-plates with irregular shapes. The product solution with purple colour (irradiated at 505 nm) has a sharper absorption peak at 540 nm and a small peak at 460 nm, and the majority of NPs in the product solution were nanoprisms and nano-discs. Both 625 nm and 505 nm irradiation might promote slow growth of the planar-twinned crystals in the seeds solution and resulted in the formation of triangular prisms, where without dual-irradiation, uncontrolled fusion sequentially takes place (Jin *et al*.

2003; Tang *et al*. 2013). The product solution with orange colour (irradiated at 470 nm) has the sharpest absorption spectrum, with a large peak at 498 nm and a smaller one at 400 nm. The TEM image showed that the solution contained mostly decahedra as well as a small fraction of tetrahedra and bi-tetrahedra. Only the 470 nm product solution showed strong reflection of green light in a dark background (**Figure 5.1 B5**). This shows a significant scattering part in the extinction, which is the case for larger particles

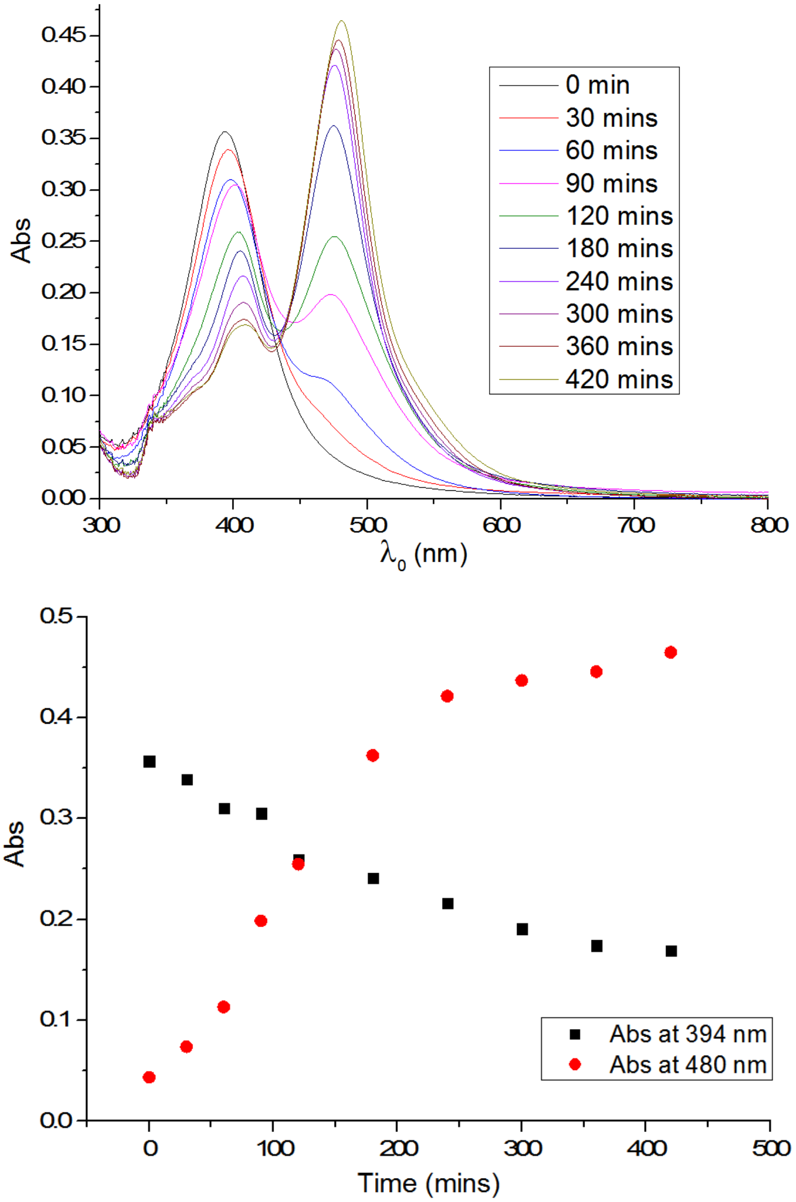

Figure 5.2. Kinetic study of the decahedron formation during 455 nm LED irradiation. 7 mL of standard seeds solution (OD_{400nm} = 3.5) was irradiated with a 455 nm LED (ThorLabs). **Upper panel)** the

irradiation was paused at different time points, and 50 µL of the reaction solution was sampled and diluted (1 in 10) for UV-Vis spectroscopy. **Lower panel**: The absorbance at 394 nm (red dots) and 480 nm (black dots) were plotted against the irradiation time.

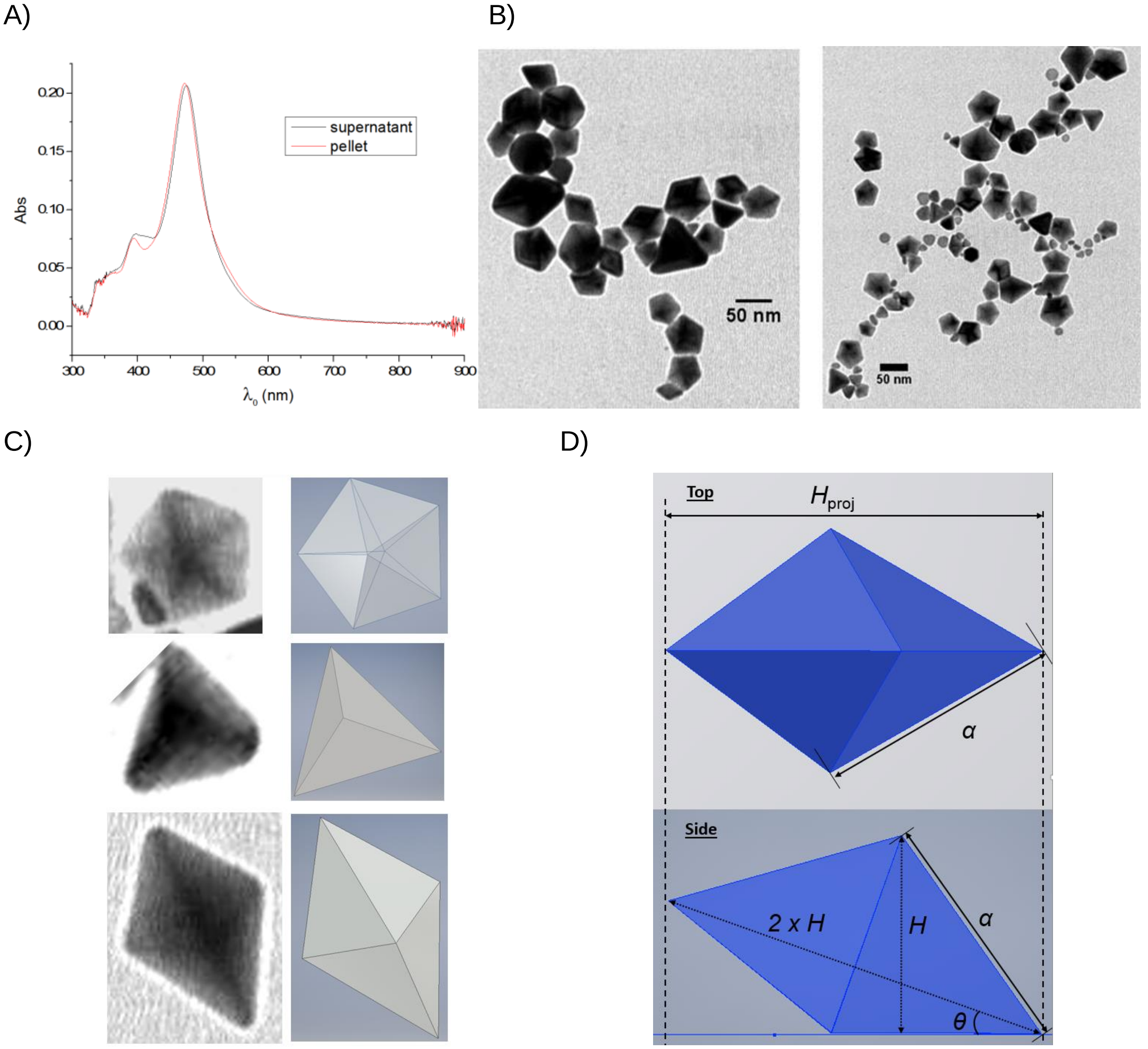

Figure 5.3. The product solution after 455 nm LED irradiation was centrifuged at 500 rcf for 20 mins **A**) UV-Vis spectra of the resuspended pellet (**Black line**) and the supernatant (**Red line**) after centrifugation. **B**) HR-TEM images (JEOL JEM-1011) of the drop-casted solution of resuspended pellet (**Left**) and supernatant (**Right**). **C**) Top view of the proposed 3D structure (modelled by AutoCAD inventor) for different projections found on the TEM micrographs: decahedron for the pentagonal projections (**left**), tetrahedron for triangular projections (**mid**) and bi-tetrahedron for Kite-shaped projections (**right**) **D**) the proposed 3D structure (modelled by AutoCAD inventor) for bi-tetrahedron lying on a substrate, *α* is the edge size; H_{proj} is the projected length of the long axis; *H* is the space height of

the pyramid that consists of half of the bipyramid; the angle of inclination between the long axis and any face of the bipyramid is *θ.* **E**)

Subsequently to these results, we used a 455 nm LED as irradiation source, which resulted in a higher yield of decahedra with sharp edges. A kinetic study (**Figure 5.2**) showed that the characteristic absorption spectrum was formed within 7 hours irradiation. After 7 hours, the spectral features remained more or less the same even after overnight irradiation. The kinetics of the spectral changes (peak intensities at 394 nm and 480 nm) shown here is consistent with the reports in literature (Zheng *et al*. 2009), despite the fact that different volume/concentration of solution and irradiation source were used here. During the initial 7 hours period, the seed peak at 390 nm gradually decreased while the peak around 480 nm was gradually formed. During subsequent 16 hours irradiation (not shown here), there was a small (5 nm) red-shift of the peak to 500 nm, which is also present in data shown in the literature, but has not been investigated. The red-shift might be the result of corner sharpening or shape/size focusing effect of various Ag crystals populations in the solution (discussed below in **Section 5.2**).

All the TEM micrographs in **Figure 5.1 C** have a dark background. This was likely due to the leftover reactants and by-products since the product solutions were drop-casted onto the TEM grid without purification procedure. Centrifugation, as a convenient way for purification of NPs from aqueous solution, was used to remove i) the unreacted reagent and small by-product molecules; ii) the Ag crystals with small mass/volume, such as remaining Ag seeds and small /medium sized Ag plates in the product solution. For removing the small molecules in the supernatant, since all of the reagents and small molecule by-products are water soluble (as no precipitates formed after irradiation), high speed centrifugation is desirable to prevent loss in yield. We found previously that centrifugation with 1500 rcf for 20 mins resulted in a separation of 40 nm spherical AgNPs without significant loss (data not shown here). Below this speed, the AgNP pellet at the bottom of the centrifuge tube started to become soft, which can lead to significant loss in yield when removing the supernatant. Since the decahedra have about 30 nm - 50 nm longitudinal length, the same centrifugation settings were used for removing the small molecules. Despite PVP and sodium citrate being present in the solution, repetitive centrifugation at these settings caused aggregation (the pellet could not be resuspended even with sonication). Therefore, only a single centrifugation and resuspension (wash) with this setting was used. To remove the small Ag crystals, which have a smaller mass difference to the decahedra, a weaker centrifugation was required. To optimize the separation while retaining a good yield, different centrifugation speeds were tested. **Figure 5.3. A** shows that when using 500 rcf for 20 mins, the supernatant and the pellet-resuspension (using the same volume as the initial solution, and 0.1% PVP and 2 mM citrate buffer for resuspension) had similar absorption spectra with the same peak amplitude, indicating that roughly half of the Ag volume in the solution was separated between pellet and supernatant (assuming that the absorption is proportional to the volume for constant shape, which is correct for small plasmonic particles dominated by absorption). The spectrum of the pellet-resuspension has a sharper speak at 400 nm, which is thought to be the resonance of the quadrupole mode of the decahedron. This is more pronounced for larger particles, since at a given edge sharpness, the edges are more defined, increasing the excitation of the quadrupolar mode. In contrast, the spectrum of the supernatant extra absorption in between the quadrupole mode peak and the dipolar peak (at 490 nm), indicates that the supernatant contained a larger amount of small irregular Ag crystals. To minimise the aggregation in the pellet, low speed (500 rcf, 20 mins) centrifugation was carried out before the high speed (1500 rcf, 20 mins) centrifugation to remove the chemicals in the product solution before using high speed to push NPs close together. The resulting TEM micrographs (**Figure 5.3. B**) showed that after this 2-step purification via centrifugation, the pellet-resuspension had good yield of decahedra without small particles or dark background.

5.2 Statistical analysis of AgNP populations

Because the AgNPs from colloid synthesis tend to have high symmetry (**Section 1.4.2**). It is possible to figure out the 3D structure of the AgNPs in the product solution from statistical analysis of TEM data as well as data in literatures. On the TEM micrographs obtained in IIT (**Figure 5.3 B**), we see the 2D projection of the NPs on the sample grid. Among 148 NPs across 3 TEM micrographs of the purified production solution (455 nm irradiation), there were about 72% of pentagonal projections, 14% of triangular projections, 6% of Kites-shaped projections and 8% other irregular shaped projections. The NPs with irregular shapes have relatively weak contrast on the TEM micrograph and some of them overlap to produce regions with stronger contrast, indicating that these NPs are likely to be Ag plates with a few nanometer thickness.

5.2.1 Pentagonal projection / decahedron

The NPs with pentagonal projection appeared to have more volume than the Ag plates, as derived from their stronger contrast, and many of them have a fivefold twinning structure visible on the TEM micrograph (dark lines originating from the centre toward each corners). These are the features of Ag decahedron previously described (Ye *et al*. 2015; Zheng *et al*. 2009; Gao *et al*. 2006). (Sanchez-Iglesias *et al*. 2006) fabricated 44 nm edge-size Au decahedra by growing PVP passivated gold seeds with ultrasound; TEM micrographs of the Au decahedra closely resemble the Ag decahedra in (**Figure 5.3 C left**). Tilting experiments (±45°) of HR-TEM showed the Au decahedron was composed of pentagonal bi-pyramids of equal equilateral-triangle faces, with somewhat rounded edges (2 nm radius). It is observed that during colloid synthesis metal nanoparticles tend to grow into the structure of one of the Platonic solids (Xia *et al*. 2009). All Platonic nanocrystals have three common features: i) they are constructed by congruent (identical in shape and size) polygonal faces; ii) their polygonal faces are regular (all angles equal and all sides equal); iii) the same number of faces meet at every corner. The Au decahedron only has the first two features but not the 3rd one. Studies of 3D structure of Ag decahedra from plasmon mediated fabrication have not yet been reported. It is very likely that the Ag decahedra we observe have regular faces, since they were fabricated from colloid growth. We randomly selected 115 Ag decahedra on the TEM micrographs and measured the longest edges of their pentagonal projections. Those edges are likely to be the ones that are parallel to the substrate surface (or with smallest tilt angle to the substrate surface). The Ag decahedra in the purified product solution have an average edge-length of 28.7 nm with a standard deviation of 8.2 nm.

5.2.2 Triangular projection / Tetrahedron

Some NPs with the triangular projection also appeared to have more volume than the Ag plates. Many of those crystals have the most electron-scattering area (dark region on the TEM micrograph) in the centre of the triangle, from where 3 dark lines extended to 3 corners of the triangle (**Figure 5.3 C mid**). This pattern closely resembles that of Ag tetrahedra (Zhou *et al*. 2008). Furthermore, the triangular projections appeared to be equilateral triangles, consistent with the assignment of these NPs to Ag tetrahedra. Because the substrate surface of the silicon dioxide grid is flat, most of the Ag tetrahedra settled with one of their faces flat on the substrate. If we assume that the contacting face is parallel with the substrate, this face has the same dimension as the triangular projection of the tetrahedron. We randomly selected 21 Ag tetrahedra on the TEM micrographs and measured the lengths of the 3 edges of each projection. The Ag tetrahedra in the purified product solution have an average edge-size of 36.7nm with standard deviation of 13.9 nm. As discussed in Chapter 1, in the literature Ag tetrahedra were selectively synthesised by plasmon-mediated fabrication (Zhou *et al*. 2008; Zheng *et al*. 2007). Tartrate was added to the initial solution, which was thought to assist the nucleation of small Ag seeds into tiny tetrahedra via face-selective binding. Citrate was also added before irradiation, which not only served as the reducing agent for slow growth (**Section 1.4.3**) during irradiation but also to selectively cap (Al-Rammahi and Henderson) facets to preserve them in the final structure. Electron diffraction showed that those Ag tetrahedra were single crystalline nanoparticles. We did not use tartrate here, but it is possible that a smaller portion of seeds were single crystalline that later grew into tetrahedra with the help of citrate molecules in our reaction solution.

Statistical measurements of AgNPs in the product solution

Projections on TEM	Pentagon	Triangle	Kite
Percentage found	72%	14%	6%
Edge size α (nm)	28.7 ± 8.2	36.7 ± 13.9	37.1 ± 10.6
Longitudinal length H_{proj} (nm)	46.2 ± 9.1	26.2 ± 7.1	58.0 ± 19.13

Table 5.4. Average size of the projections shape on the TEM micrographs measured with imageJ.

5.2.3 Kite projection / Bitetrahedron

Some NPs with the convex-Kite-shaped projections are clearly thicker (i.e. darker) than the Ag plates. Many of those crystals have the most electron-scattering area (dark region on the TEM micrograph) near the centre of the projections, from where 4 dark lines extended toward to 4 corners of the Kite (**Figure 5.3 C right**). There can be a number of possible 3D polygon structures can produce Kite-shaped projections; statistical analyse is required to elucidate the morphology of those AgNPs from the TEM micrographs: If we assume that all immobilised Ag crystals have a face in contact with the substrate surface, the most likely 3D structure for these observed features is a triangular bipyramid that consist of 6 triangle-shaped faces. The structure is equivalent to two identical irregular or regular tetrahedra symmetrically placed base-to-base. Octahedra can also produce the convex-Kite-shaped projection, however, they are also able to produce a range of irregular shaped projection when immobilised on the substrate (Seo *et al*. 2006) which we have not observed on our TEM micrographs. Furthermore, the Kite-shaped projection from the octahedron should always have aspect ratios close to one; the average aspect ratio of the Kite projection here is 1.59 with standard deviation of 0.64. We randomly selected 15 Ag bi-tetrahedra on the TEM micrographs and measured the long-side lengths (the edges on the face contacting the substrate) to have an average value of α = 37.1 nm with a standard deviation of 10.6 nm, which should be the average edge-size of the triangular bipyramids. The Kite-shape projections have an average width (the short diagonal of the Kite) of 38.62 nm with a standard deviation of 11.7 nm, which is close to the average value of edge-size. The Kite-shaped projections have an average length (the long diagonal of the Kite) of H_{pro} = 58.0 nm with a standard deviation of 19.13 nm. This is close to the calculated value obtained as follows (**Figure 5.3 D**): A single triangular bipyramid with edge-size α has a long axis of $2{*}H = 2(\sqrt{6}/3)\alpha$, where H is the space height of the pyramid that consists of half of the triangular bipyramid; the angle of inclination between the long axis and any face of the bipyramid is $\theta = \arcsin(H/\alpha) = 0.34$ rad. Therefore the projected length of the long axis is $H_{proj} = \cos(0.34 \text{ rad}) * 2{*}H = 1.54\ \alpha$. For a triangular bipyramids with α = 37.1 nm this is H_{proj} = 57.2 nm. All those results support that the NPs with the Kite-shaped projection are regular (equilateral) triangular bipyramids (known as bi-tetrahedron). NPs with the Kite-shaped or rhombus-shaped projection were also found on the TEM micrographs of drop-cast product solution from plasmon mediated fabrication of Ag decahedra in the literature (Zheng *et al*. 2009; Ye *et al*. 2015). Many authors assign those projections to Ag decahedra with a side view orientation or ignored them in the discussion. It is possible for an Ag decahedron to produce a Kite-shaped or rhombus-shaped projection, however, this requires the Ag decahedron to be in contact with the substrate only via an edge or corner. Furthermore, in our TEM micrographs, Ag decahedra have an average longitudinal length (the longest diagonal of their pentagon projections) of 46.2 ± 9.1 nm, which is significantly smaller than the average H_{proj} of the bipyramid (58.0 ± 19.13 nm) (**Table 5.4**). This indicates that not all of the NPs with Kite-shaped or rhombus-shaped projection can be Ag decahedra, and there must be a significant amount of NPs with more elongated 3D shapes present in the product solution. Despite the fact that the statistical measurements agreed with our proposed 3D shapes of the NPs in the purified product solution, the hypothesis still needs to be confirmed with scanning electron microscopy over a large number of product NPs, which can reveal surface topography of the NPs. In the literature, silver right triangular bipyramids were synthesised by plasmon mediated fabrication (monochromic LED as irradiation source) (Zhang *et al*. 2009). The right triangular bipyramid has the same 3D structure of a bi-tetrahedron, except that it consists of 6 isosceles right triangles. When lying on a substrate, a right triangular bipyramid will also produce a Kite-shaped projection on the TEM micrograph (**Figure 4.6B Right**). This projection should have a much smaller aspect ratio in comparison with the Kite-shaped projection in our TEM micrographs. Mirkin's group has fabricated right triangular bipyramid with edge-sizes of 106 nm, 131 nm, 165 nm and 191 nm by irradiating the seed solution with 500 nm, 550 nm, 600 nm and 650 nm light (LED) respectively. $AgNO_3$ and bis (p-sulfonatophenyl) phenylphosphine dihydrate dipotassium were added to the reaction solution with higher pH, which is thought to increase the Ag^+ reduction speed and allow a self-nucleation of the Ag seeds with planar twinned defects. The higher rate of Ag^+ reduction (higher pH, and higher free Ag^+ concentration) led to monodisperse right triangular bipyramid, whereas a lower rate of Ag^+ reduction (lower pH, and lower free Ag^+ concentration) led to an increased amount of Ag plates. On our TEM micrographs, we did not observe the characteristic projection of right triangular bipyramids, but there were plenty of Ag plates. In our reaction solution, excessive amount of sodium hydroborate was used to convert all the $AgNO_3$ into Ag seeds. Therefore, during the irradiation step, Ag^+ was supplied from slow dissolution of Ag seeds by the irradiation, and only Ag plates were produced from Ag seeds with planar twinned defects.

Small fractions of tetrahedra and bi-tetrahedra were reported in the literature to be in the product solution of Ag decahedra synthesised by irradiating the growth colloid seeds with 465 nm LEDs (Zheng *et al*. 2009). Both crystal structures were also reported in silver decahedra synthesised by PVP-assisted N,N-dimethylformamide (DMF) thermal mediated reduction (Gao *et al*. 2006). It has be proposed that in both thermal mediated and plasmon mediated fabrication, the majority of decahedra originated from epitaxial growth of the five-fold symmetric twinning seeds, with some decahedra formed by a step by step aggregation/fusion process (from single tetrahedra to bi-tetrahedra then tri-tetrahedra etc.). On our TEM micrographs, the average edge-size of the tetrahedra is close to that of the bi-tetrahedra. Perhaps the bi-tetrahedra were originated from fusion of a pair of tetrahedra with similar size; alternatively the bi-tetrahedra form by introducing a stacking fault at some point during growth when starting a new 111 plane, at which point the facets revert and a bipyramid is formed. The average edge-size of the decahedra (28.7 ± 8.2 nm), on the other hand, is smaller than that of the tetrahedra (36.7 ± 13.9 nm). Considering the standard deviation, it is possible that some of the large decahedra were formed via fusion of tetrahedra. However, we did not observe any tri-, quadri- or penta- tetrahedra on our TEM micrographs, although the projection of those structures can be hard to predict in the regions of the substrate with the crowded crystals. SEM analysis could be used to identify the presence of such shapes. The fusion process observed in the plasmon mediated fabrication of nanoprisms was thought in the literature to be the result of the redistributions of high local fields to the fusion site to facilitate the process during the irradiation step. Modeling the electromagnetic field around a tetrahedron as well as a bi-tetrahedron will help us to elucidate this fusion process.

The 3D geometry of NPs that have a Platonic structure (e.g. tetrahedron or cube) or consist of multiple of the same type of Platonic structures (e.g. bi-tetrahedron and decahedron) can be entirely defined by the edge side of the NPs. However, as discussed in Chapter 1 (and also shown in **Figure 6.16)**, the optical properties of AgNPs are highly sensitive to their shape and sizes. Colloid synthesis is unlikely to produce AgNPs with perfect symmetry, for example we found typically 2 to 5 nm differences in the length of the edges on the same tetrahedron. High resolution TEM or even TEM tomography experiments might be required for investigating the small structural features such as corner rounding and 3D orientation that are known to have significant effects on the optical properties of the AgNPs.

5.3. Correlative imaging

After returning from the internship in Italy, seed solutions was synthesised with the same protocol developed at IIT. We also have set up a irradiation chamber (**Figure 2.1** in **Section 2.1.2**), which was designed for fabricating AgNPs with different shapes and sizes as well as for studying the plasmon mediated fabrication in Borri and Langbein's lab. In this thesis, the AgNPs in the product solution obtained from the 447.5 nm irradiation were investigated.

Figure 5.5 shows that after overnight irradiation of the seed solution with the 447.5 nm LED in the chamber, the colour of the solution was changed from yellow to orange, and the product solution weakly scattered green light. The spectra of the purified product solution showed the two characteristic peaks of silver decahedra. TEM micrographs of the purified product solution showed mostly Ag decahedra, a small amount of AgNP seeds and plates, and was free from the dark background observed previously. Similar to the TEM micrograph of the product solution obtained in IIT, decahedra of a significant size distribution, as well as Ag tetrahedra and bi-tetrahedra are found. Free access to TEM analysis was provided by the industrial collaborator BBI Solutions during my PhD, and was used for the image in **Figure 5.5**. However the available TEM instrumentation had a low resolution and missed a spatial calibration, hence the size of the crystals in this image were not measured. Nevertheless, it served the purpose to qualitatively show the heterogeneity of the AgNPs in the product solution. With the imaging techniques developed in our lab, we can use this heterogeneity as a convenience to study the optical properties of each single particle with different shapes and size on one sample grid. Correlative optical TEM studies on a single Ag decahedron, tetrahedron or bi-tetrahedron have not yet been carried out in the literature.

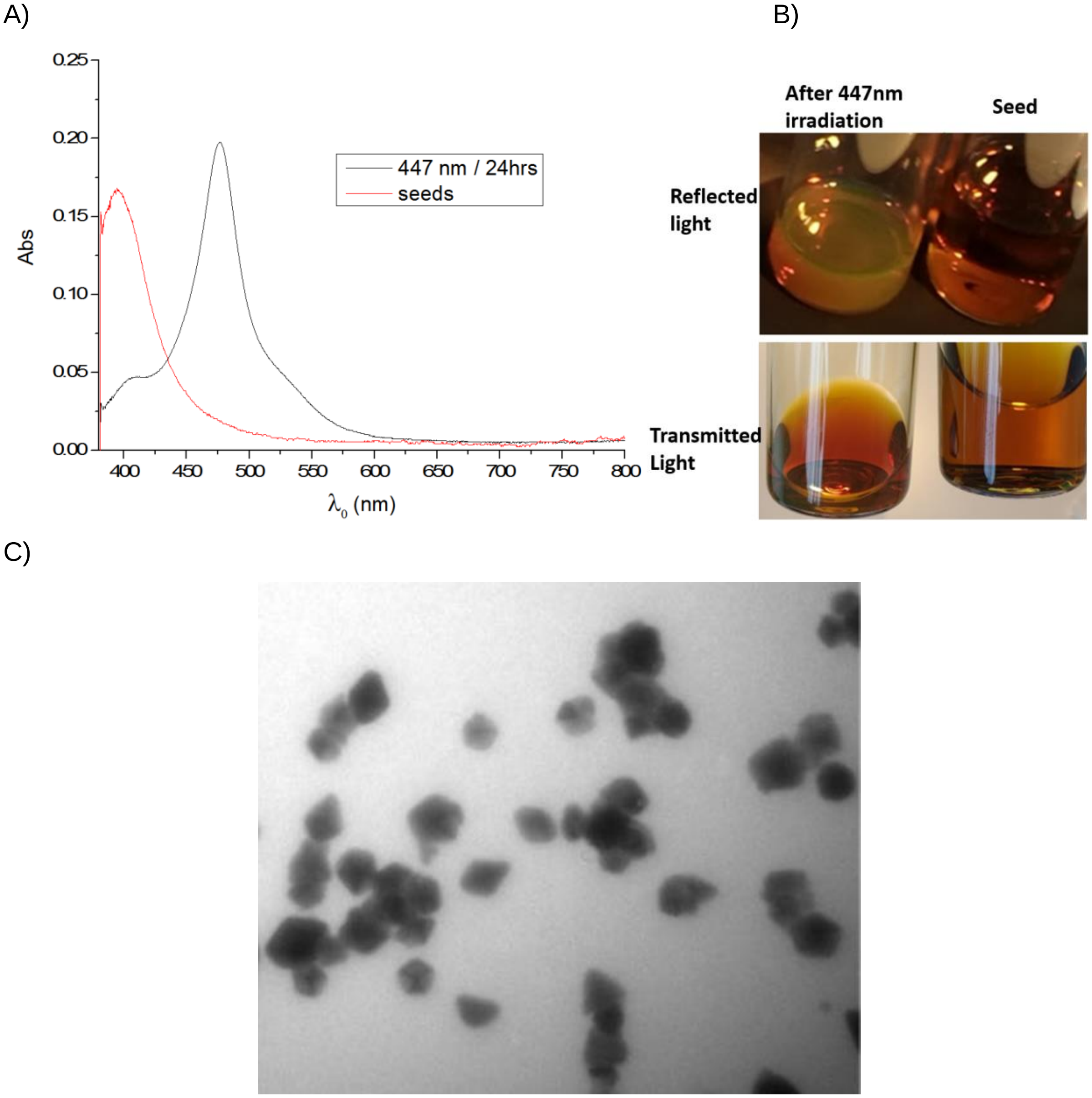

Figure 5.5. Plasmon-mediated fabrication with custom built irradiation chamber in our lab. The seed fabrication and irradiation condition are described in **section 2.1.2** **A**) UV-Vis absorption spectra of seeds solution (**red line**), and after 447 nm / 24 h irradiation (**black line**). **B**) Colour photographs of

transmitted light and scattered light from the seeds and product solution 24h. **C**) TEM of the solution after 447 nm / 24 h irradiation, purification and drop-casting onto a copper grid with Formvar carbon film according to the procedure in **Section 2.1.5B** (by Philips CM100 TEM, the camera system was not calibrated, thus the scale bar was unavailable).

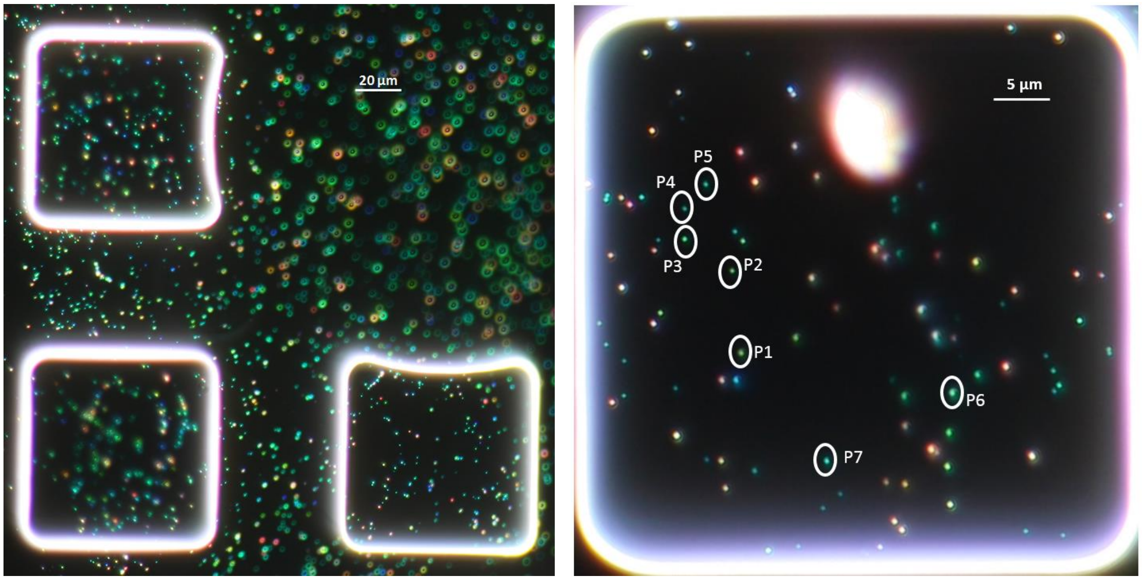

Figure 5.6 Left) DF image of NPs from the purified product solution (447nm/24h) (OD_{475nm} = 0.20 settled on a 1% APTES functionalised SiO_2 film using the standard method described in **Section 2.1.4** and **Section 2.1.6 B** and mounted in anisole. SiO_2 film is the top of mesh, and the square regions have no support (**Figure 3.1**). The SiO_2 film inside the region can show bending due to residual strain, whereas the support is very flat. Furthermore, the grid can sometime be slight tilted, creating a focus gradient, and defocussed regions. **Right)** DF imaging of grid G, window outer-16; 7 particles from this window were selected for correlative imaging (white circles and numbered P1 to P7); the data are presented in **Figure 5.6**.

To carry out our correlative optical and TEM imaging (using the high-resolution TEM facility at Cardiff University), NPs in the purified production solution were settled onto an APTES functionalised SiO_2 / SiN TEM grid (details in **section 2.1.6B**). DF images (**Figure 5.6**) of the grid mounted in anisole showed that the product solution contains particles with various LSPR with the majority of them scattering cyan or green light. This is consistent with the majority of NPs on the TEM micrograph in **Figure 5.5 C)** being decahedra, and the main extinction peak of the product solution being about 500 nm (note that, similar to what will be shown for the 40 nm spherical AgNP in **Figure 6.2** and **Figure 6.10**, the LSPR frequency of these AgNPs red-shifts by about 35 nm when transferred from water to anisole, however, this is only a rough estimation the red-shifts is also depended on the shape). Most of cyan/green spots on the DF images are likely to contain an isolated decahedron as they scatter light with similar colour and intensity. Interestingly, many cyan/green spots have an anisotropic polarisation response (see also Chapter 6), namely when changing the linear polarisation orientation of the DF excitation, many NPs are excited maximally for two orthogonal polarisation orientations, with one mode scattering blue light (similar to the transverse mode of a dimer, see Chapter 1), and the orthogonally polarised mode scattering green/cyan light (similar to the longitudinal mode of a dimer). Micro-spectroscopy data (**Figure 5.7 to 5.9**) showed that the "transverse mode" of these NPs has a single LSPR peak around 470 nm (called P1), whereas the "longitudinal mode" has a LSPR peak (called P2) red-shifted by $\Delta\lambda = \lambda_{p2} - \lambda_{p1}$ in the range of 50 to 100 nm. 10 green and cyan coloured NPs with various $\Delta\lambda$ were selected for the correlative imaging studies. Because each mounting of the sample grid in anisole can only last about 5 to 6 hours before the sample chamber starts to dry out, the absorption and scattering spectra of the each NP were taken under 1) unpolarised light; 2) polarised light at the angle (θ_{tran}) where peak amplitude of P1 of the candidate is the highest; 3) polarised light at the angle (θ_{long}) rotated 90° from the angle used in 2).

In the correlative TEM imaging, all encountered NPs, including the selected candidates, were found to have one of the following three structures: tetrahedron, bi-tetrahedron or decahedron. Correlative data (DF image, microspectroscopy and TEM micrograph) of 7 selected NPs were obtained (**Figure 5.7 to 5.9).**

5.3.1 Single silver decahedra

TEM showed that nanoparticles labelled as NP1, NP2 and NP3 (**Figure 5.7 Right**) are Ag decahedra (**Figure 5.7 left** column lower panel). Although the thickness of Ag decahedron from plasmon mediated fabrication has not yet been measured in literature, TEM tilting experiments showed that a 40 nm edge-size gold decahedron from colloid synthesis has a regular shape (each face is an equilateral triangle) (Sanchez-Iglesias *et al*. 2006). If we assume that our decahedra have a regular shape, we should be able to construct the 3D structure of the crystal. We measured the longest edge-size of the pentagonal projection on the TEM micrograph as the estimate of the edge-size. All three decahedra here have edge-size close to the average value of 28.7 nm measured in **Section 5.1**.

(Pietrobon and Kitaev 2008) were able to regrow small decahedra (35 nm) adding Ag seeds under metal halide lamp irradiation to produce Ag decahedra with edge-size of 35, 46, 57, 69, 88, and 123 nm. The spectra of those product solutions all have two absorption peaks (P1 and P2); P2 red-shifted from 460 nm to 570 nm as the average edge-size increased from 35 to 123 nm, whereas P1 only red-shifted from 390 nm to 420 nm. In (Ye *et al*. 2015), a 3D model was constructed with the commercial software package COMSOL Multiphysics (COMSOL Inc.) using the finite element method (FEM) which showed that a single 32.8 nm edge-size Ag decahedron in water has a single LSPR at 454 nm, and that the LSPR only red-shifted by 6 nm when the edge-size increased to 37.6 nm. The numerical simulation also showed that the corner sharpness of the Ag decahedron (measured as the radius of the rounded corners) had a significant effect on its spectral features: as the corners of a 32.8 nm edge-size Ag decahedron sharpened from 2.5 nm to 0.5 nm radius, the LSPR peak red-shifted from 454 nm to 500 nm. The simulated distribution of the electric field of Ag decahedra with different corner sharpness showed that the localised field of the LSPR at the edges was enhanced by increasing the corner sharpness. Those data explain our observation that NP2 is the smallest of the three decahedra, but its P2 is red-shifted by the greatest amount due to its sharp corner (**Table 5.10**).

NP1

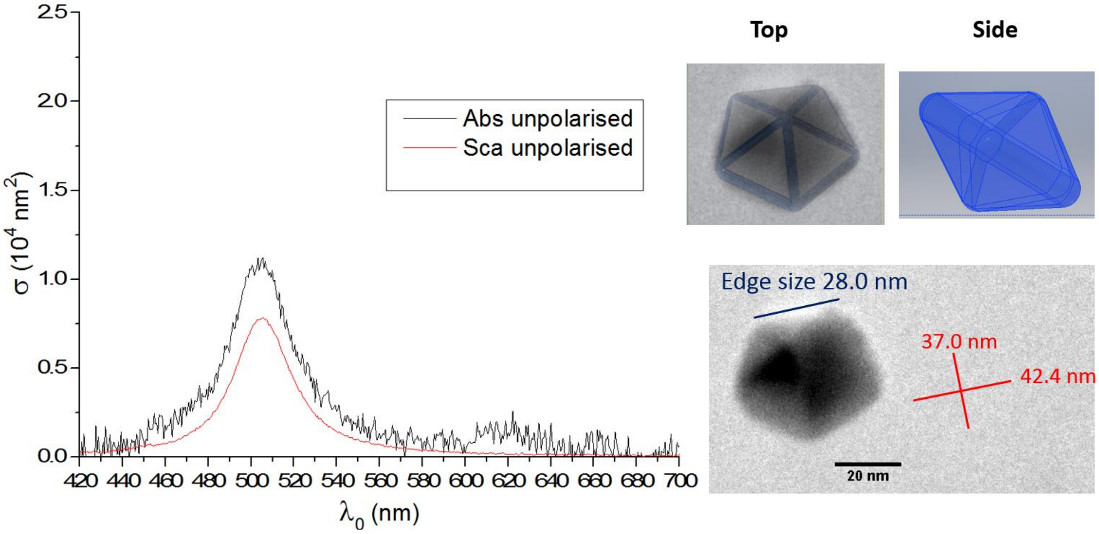

NP2

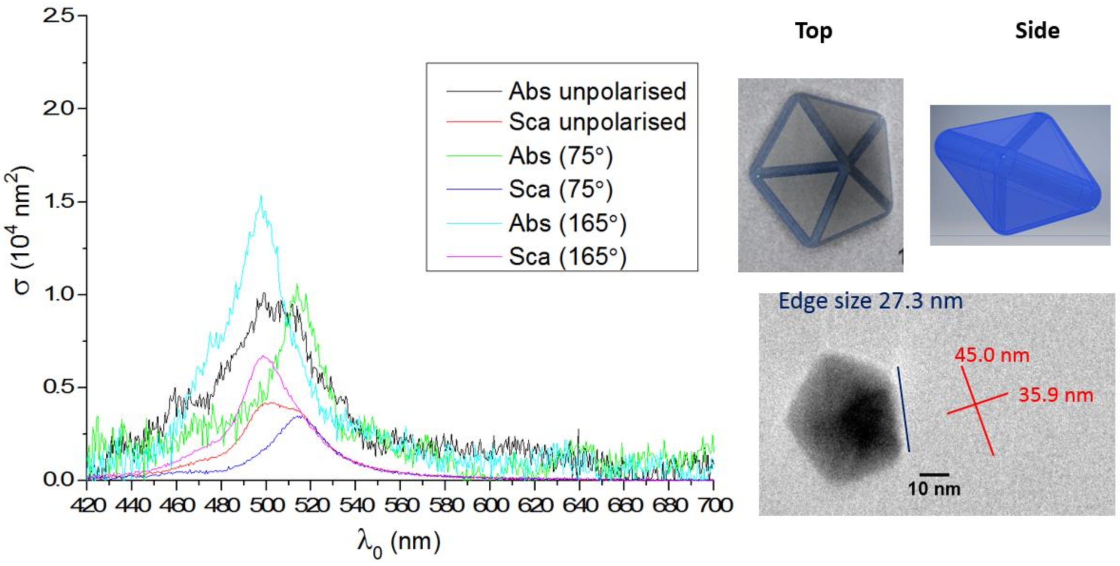

NP3

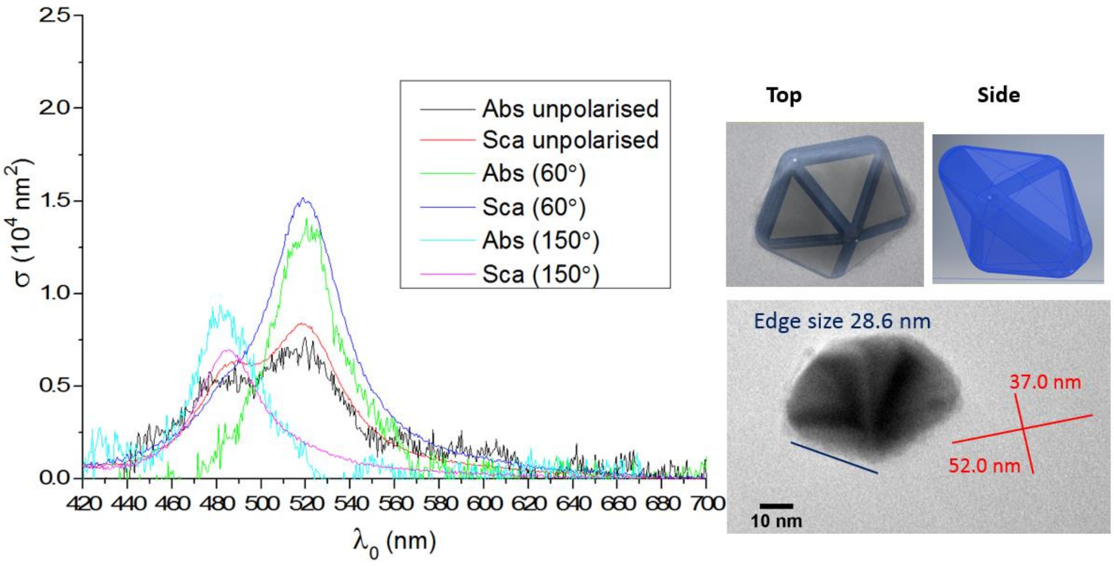

Figure 5.7 Correlative studies of NP1 to NP3 in **Figure 5.6 Left). Left column**: polarisation resolved absolute absorption and scattering spectra of each candidate NP (**Section 2.3.2**). The parameters for the quantitative analysis were computed analytically on MATLAB as follow: for the spectra of NPs in anisole: ξ =1.54, f_{BF} = 0.112, f_{DF} = 0.138 and ζ = 1.54. **Right column lower panel**: TEM micrographs of each imaged NP; size and rounding of the NPs are measured (coloured lines and numbers) and summarised in **Table 5.10. Right column upper panel:** Preliminary 3D models of the imaged NPs (see details are discussed below)

Ag decahedral particles have a lower symmetry (D_{5h}) than cubic and spherical AgNPs, and the immobilised Ag decahedron on the substrate can have various degree of tilting due to the roughness on the substrate or NP itself. Thus, Ag decahedra with similar edge-sizes can produce a variety of 2D projections on TEM micrograph, those projections also reflect how the incident polarised light interact with the Ag decahedra. Therefore, the spectral features observed for a single Ag decahedron depends not only on its shape and size but also its 3D orientation on the substrate. Because the sample grid can occasionally move and rotate during the imaging steps, and the orientation of the TEM micrograph changed slightly under different magnifications, we were unable to correlate the angular coordinates of the polariser and the orientation of the TEM micrograph. In terms of characterising the size and shape of the Ag decahedra, we measured the length of the longest diagonal of the pentagon projection (referred as longitudinal length here). On the transversal axis, we measured the width of the pentagonal projection (referred as transverse length here). The aspect ratios were calculated as longitudinal length/transverse length. **Figure 5.7** left column showed that P2 of our decahedra red-shifted further as their aspect ratio increase. The aspect ratios can be used to calculate the tilt angle, and accordingly a relative excitation of the two modes.

A numerical simulation with COMSOL is currently being developed in the group (Dr. Zilli) to better understand the correlative data obtained and the optical properties of the Ag decahedra.

5.3.2 Single silver tetrahedra

The optical properties of Ag tetrahedra have not yet been well studied in the literature; this is mainly due to the difficulty of large scale fabrication. In (Zhou *et al*. 2008) the fabrication of 100 nm edge-size Ag tetrahedra with light-driven growth is reported. The spectrum of the product solution had a large broad LSPR peak at 650 nm, and 2 or 3 smaller LSPR peaks in the 550 nm to 400 nm region. SEM micrographs showed that the product solution also contained about 30% silver plates. (Wiley *et al*. 2006a) calculated the UV-vis extinction spectrum of a 40 nm Ag tetrahedron in water using the discrete dipole approximation (DDA) method and showed that it has two broad LSPR peak at 570 nm and 680 nm. The Ag tetrahedron was thought to have the most red-shifted resonance peaks than other 40 nm AgNPs with Platonic structures, because it has the sharpest corners. We obtained correlative data of one 40 nm tetrahedron (**Figure 5.8**). It also has two LSPR peaks, but less red-shifted than the calculated spectrum in the literature, which might be the result of corner rounding the calculated spectra in (Wiley *et al*. 2006a) did not consider corner rounding of the tetrahedron.

It is important to notice that the polarisation resolved micro-spectroscopy data (**Figure 5.8 left**) shows that P1 and P2 of the Ag tetrahedron are present at both polarisation angles. This is due to the triangular shape of the particle, which does not have a two-fold symmetry and thus no splitting of the dipolar modes. The modes visible are thus different mixtures of dipolar and quadrupolar modes. This feature potentially can serve as a signature for distinguishing the Ag tetrahedra from bi-tetrahedra and decahedra during the optical imaging step of our correlative technique.

NP7

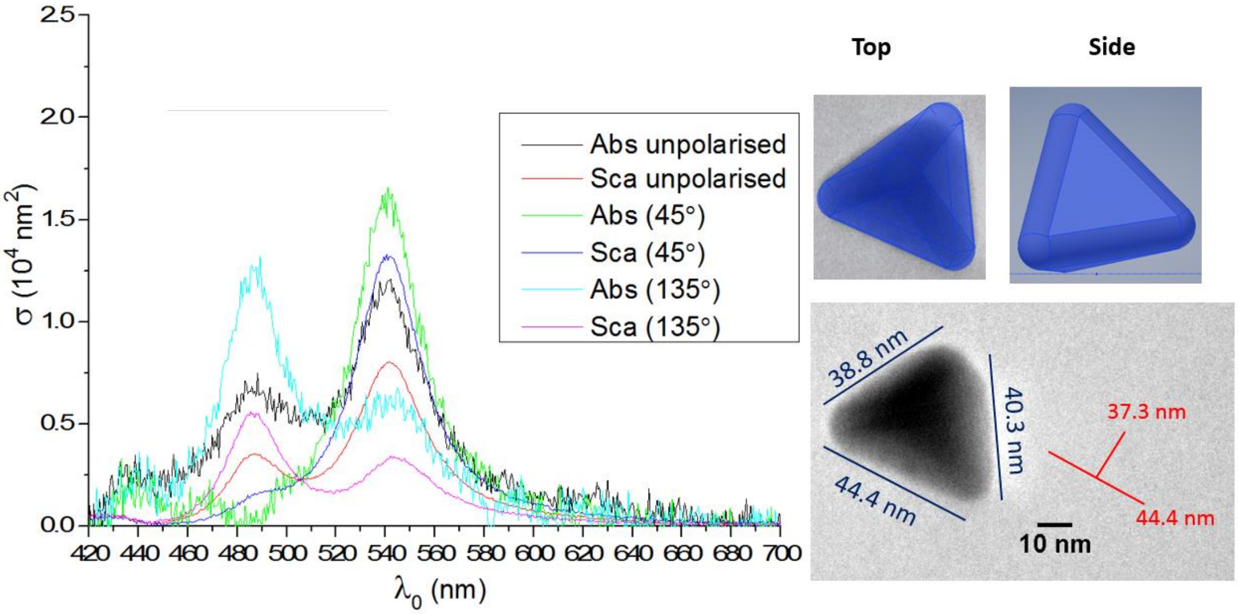

Figure 5.8 Correlative studies of NP7 in **Figure 5.6 Left). Left column**: polarisation resolved absolute absorption and scattering spectra of each candidate NP (**Section 2.3.2**). The parameters for the quantitative analysis were computed analytically on MATLAB as follow: for the spectra of NPs in anisole: ξ =1.54, f_{BF} = 0.112, f_{DF} = 0.138 and ζ = 1.54. **Right column lower panel**: TEM micrographs of each imaged NP; size and rounding of the NPs are measured (coloured lines and numbers) and summarised in **Table 5.10. Right column upper panel:** Preliminary 3D models of the imaged NPs (see details are discussed below)

5.3.3. Single silver bi-tetrahedra

Bi-tetrahedra have also not been fabricated in large scale in the literature. As discussed in Section 5.1 and in Chapter 1, both plasmon and thermal mediated colloid synthesis only yield triangular bipyramids. Mirkin's group fabricated silver right-triangular-bipyramids with edge-size of 106 nm, 131 nm, 165 nm and 191 nm using a plasmon mediated method. The 106 nm edge-size bipyramid solution showed a sharp absorption peak (P1) at 400 nm and a stronger peak (P2) at 510 nm. The orientation averaged UV/Vis spectra of the right triangular bipyramid were calculated using the DDA method (Zhang *et al*. 2009; Yang *et al*. 1995), which showed that an increased edge-length of the bipyramid resulted in a significant red-shift and broadening of P2; P1 was also red-shifted but to a much lesser extent. The calculated spectra were in agreement with the absorption spectra of the product solutions. Their model also showed that tip truncation caused a significant blue shift of the spectra.

(**Figure 5.9 and table 5.10**) show that the nanoparticles labelled as NP5, NP4 and NP6 are bi-tetrahedra; NP5 has a larger edge-size than NP4, and P2 of NP5 is red-shifted further than P2 of NP4. NP6 has the largest edge-size compared to the other two bi-tetrahedra, however it has the most rounding on its corners, which leads to a more significant blue-shift of its P1 and P2. Although right triangular bipyramids are similar in shape to bi-tetrahedra, their preferred orientations (Wiley *et al*. 2006b. McEachran and Kitaev 2008) on the substrate are very different, hence they interact with the incident light differently.

NP4

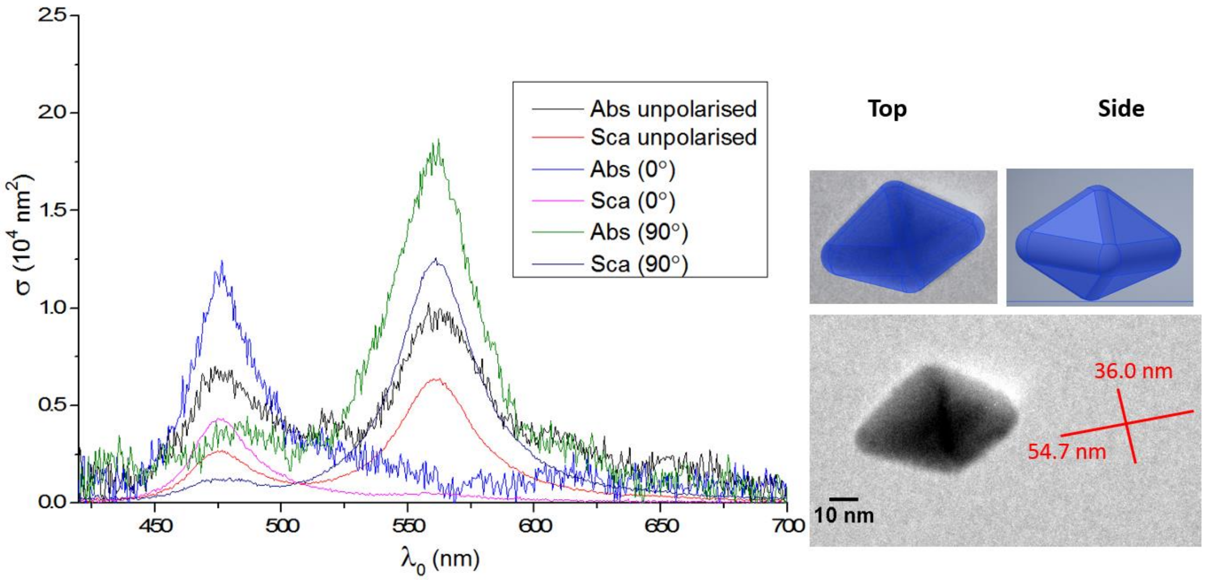

NP5

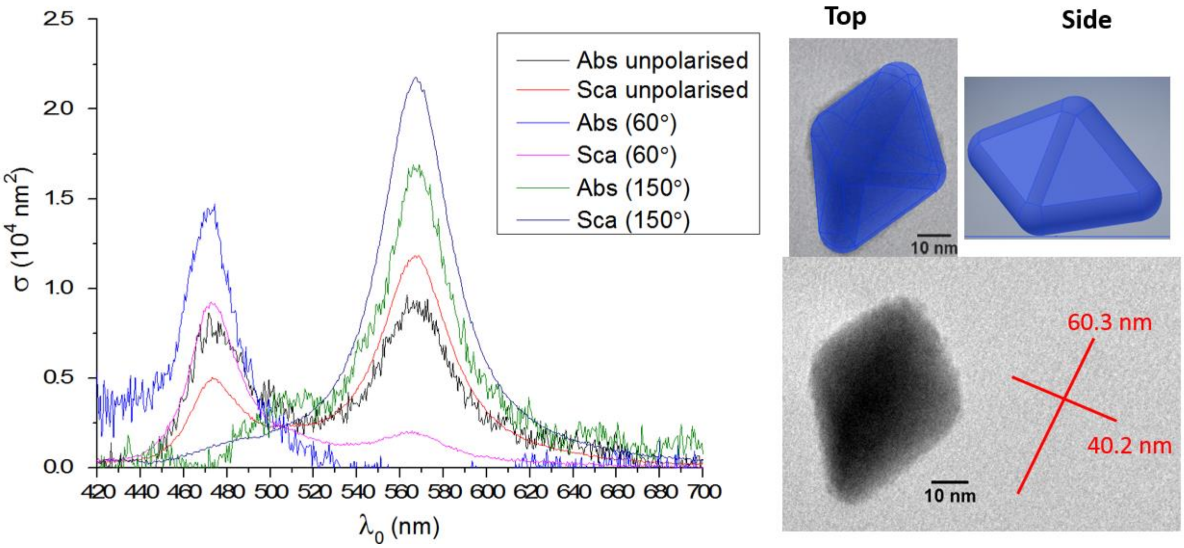

NP6

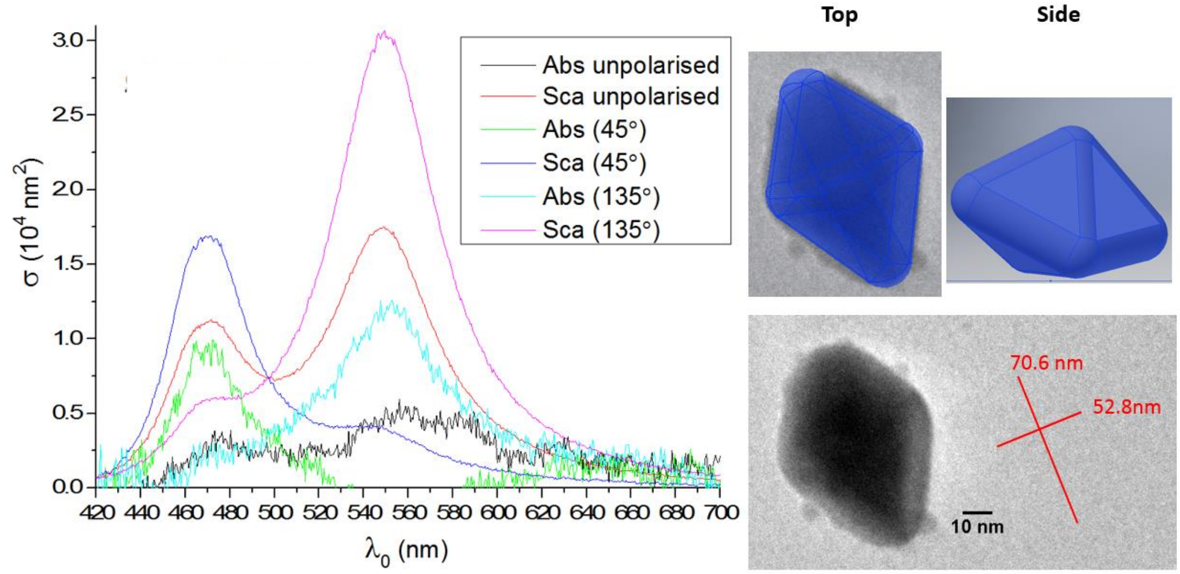

Figure 5.9 Correlative studies of NP4 to NP6 in **Figure 5.6 Left). Left column**: polarisation resolved absolute absorption and scattering spectra of each candidate NP (**Section 2.3.2**). The parameters for the quantitative analysis were computed analytically on MATLAB as follow: for the spectra of NPs in anisole: ξ =1.54, f_{BF} = 0.112, f_{DF} = 0.138 and ζ = 1.54. **Right column lower panel**: TEM micrographs of each imaged NP; size and rounding of the NPs are measured (coloured lines and numbers) and summarised in **Table 5.10. Right column upper panel:** Preliminary 3D models of the imaged NPs (see details are discussed below)

In **Figure 5.7 to 5.9**, the preliminary 3D models (by AutoCAD® Inventor) were constructed by manually fitting (overlapping) the top view of the proposed 3D shape with the TEM image of

NP, the only guides were the outer profile of the 2D projections and the dark strips within the projections. Our 3D models here assume that for each NP, all of its edges and corners have the same degree of rounding. However, from the overlapped model-TEM images (**Figure 5.7 to 5.9, Right column upper panel**) it is easy to see that some NPs have truncated sides (e.g. NP3) and corners (e.g. NP7). In fact, small number of truncated tetrahedra, bi-tetrahedra and decahedra can be found in **Figure 5.3** and **Figure 5.5**. Those truncated NPs have been reported in literature: by using dual electron microscopy labels to track the growth of AuNP seeds with silver precursors during plasmon mediated fabrication (150-W halogen lamp with a bandpass filter cantered at 550 ± 20 nm) (**Figure 5.11**), Langille and co-worker (Langille *et al*. 2012) proposed that single crystalline seed undergoes stepwise evolution: as the bimetallic NP grew, they successively developed twin planes to form multiply twinned NPs. The 3D models in **Figure 5.11 B** to **H** highly resembles the NPs found in **Figure 5.3** and **Figure 5.5**, indicating that some single crystalline seeds in our reaction solution took a similar growth pathway during the irradiation step. Therefore, we need to refine our 3D models, taking into account the truncated edges and corners. Furthermore, TEM images with higher signal-noise ratio and/or 3D tomography data with specialised image fitting software are required more accurate 3D models in the future.

Size measurements of selected AgNPs

	Shape	edge-size (nm)	Rounding radius (nm)	Longitudinal length (nm)	Transverse length (nm)
NP1	Decahedron	28.0	4.0	42.4	37.0
NP2	Decahedron	27.3	3.2	45.0	35.8
NP3	Decahedron	28.6	5.8	52.1	36.9
NP4	Bi-tetrahedron	36.3	5.1	54.7	36.0
NP5	Bi-tetrahedron	40.7	6.7	60.3	40.2
NP6	Bi-tetrahedron	52.2	12.9	70.6	52.8
NP7	tetrahedron	41.2	8.1	44.4	37.3

Table 5.10 Measured dimension of candidate NP1 to NP7 on the TEM micrographs in Figure 5.7 to 5.9. As discussed in section 5.1, the edge-size was measured from the longest edge of the projection profile

(blue line in Figure 5.7 to 5.9 right column). The rounding was measured as the radius of the rounded corners; specifically, as the average over all 5 corners for NP1 to NP3, as the corner surrounded by the two longest edges for NP4 to NP6, and as the average over all 3 corners for NP7. Longitudinal length for NP1 and NP6 is the longest diagonal of the projection (red line in Figure 5.7 to 5.9 right column); for NP7, it is the longest edge of the triangular projection profile. The transverse length is the longest width of the projection profile on the axis that is perpendicular to the longitudinal axis.

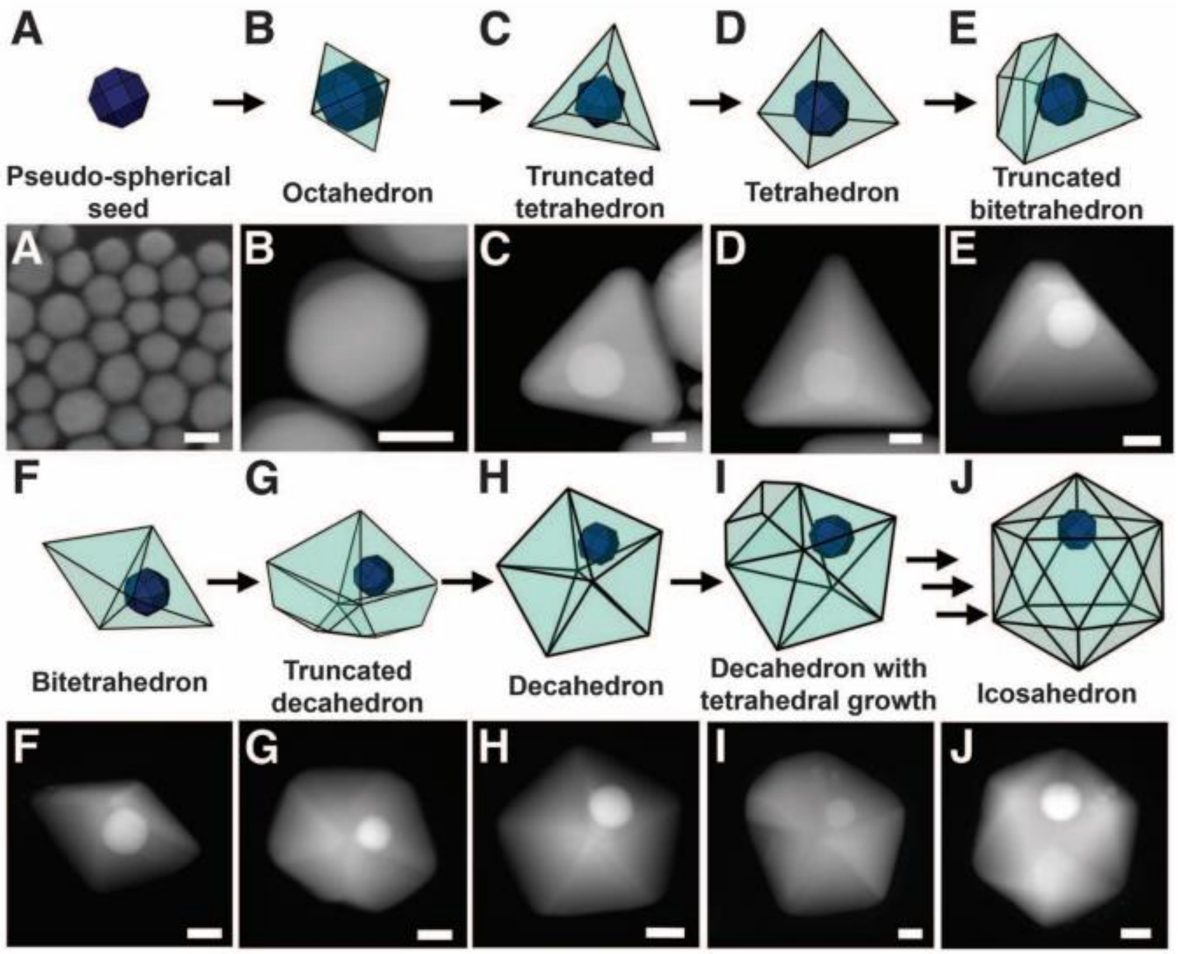

Figure 5.11 Scanning transmission electron microscopy (STEM) images and 3D models depicting the proposed growth pathway of a single crystalline Au seed into an Au-core/Ag-shell icosahedron via plasmon mediated method. **A**) STEM image of the single crystalline Au seeds. **B** to **J**) STEM images of bimetallic particles with **B**) octahedral, **C**) truncated tetrahedral, **D**) tetrahedral, **E**) truncated bitetrahedral, **F**) bitetrahedral, **G**) truncated decahedral, **H**) decahedral, **I**) decahedral with an additional tetrahedral growth, and J) icosahedral morphologies, which were all observed as products of the same reaction. Scale bars: 25 nm. Adapted with permission from (Langille *et al*. 2012). Copyright 2012 American Association for the Advancement of Science.

Chapter 6. Silver dimers

6.1 Fabrication of AgNP in aqueous solution via PEG-dithiol

Thiol functionalised polyethylene glycol (PEG) is commonly used as stabilising reagent for both AuNP and AgNP (known as PEGylation) *in vitro* and *in vivo* applications (Zhang *et al*. 2002), thanks to its water solubility and biocompatibility. For example, when these NPs are used in drug delivery, PEGylation can reduce the toxicity of the NPs and extend circulation time (Newton *et al*. 2013; Pierrat *et al*. 2007). Polyethylene glycol dithiol with different number of ethylene oxide units (abbreviated as PxDT; x= average molecular weight) were chosen as the molecular linkers for fabricating silver dimers. High concentrations of PxDT (mM range) were mixed with relatively low concentrations of NPs (pM range) in order to functionalise and passivate the NP surface at the same time, thereby dimers/aggregates are formed in relatively slow kinetics by random collisions of grafted NPs. This dimerisation reaction can then be stopped by either adding a thiol capping reagent such as NEM (**Scheme 2.1**) or immobilising the NPs onto a solid phase. PxDTs with various sizes are commercially available. The contour length (the maximum end-to-end distance of the polymer) of a PxDT is determined by the number of ethylene oxide monomer units on the polymer, which can be calculated by its molecular weight. For example, each P1000DT molecule (purchased from Sigma-Aldrich; size distribution with mean of 1k Daltons) consists of an average of 21 ethylene oxide units; each ethylene oxide unit has size a = 0.35 nm, hence P1000DT has an average contour length of 7.35 nm. Although NPs linked by P1000DT would result in a range of interparticle distances due to the flexibility of the polymer in water, dimerisation of 40 nm AuNPs or AgNPs with 7.35 nm gap-size would still result a noticeable spectral shift. P1000DT was thus first purchased to test our methodology for fabricating dimers.

Because gold is a more chemically inert element than silver, the P1000DT method was developed on AuNPs first. Citrate stabilised 40 nm AuNPs (BBI Solutions, OD_{530nm} = 0.09, equivalent to 0.8×10^{10} particles/mL, i.e. 13 pM, as per manufacturer specifications) were mixed with 0.2 mM P1000DT in a plastic cuvette, and the absorption spectrum of the reaction solution was monitored. **Figure 6.1** shows that shortly after the start of reaction, the long wavelength region of the AuNP's LSPR resonance (above 550 nm) started to gradually increase. The increased area underneath the spectrum in this long-wavelength region is accompanied by a decreased area in the single AuNP LSPR peak region (around 530 nm), indicating dimer formation and resulting plasmon coupling effects between AuNPs in close proximity (<20 nm).

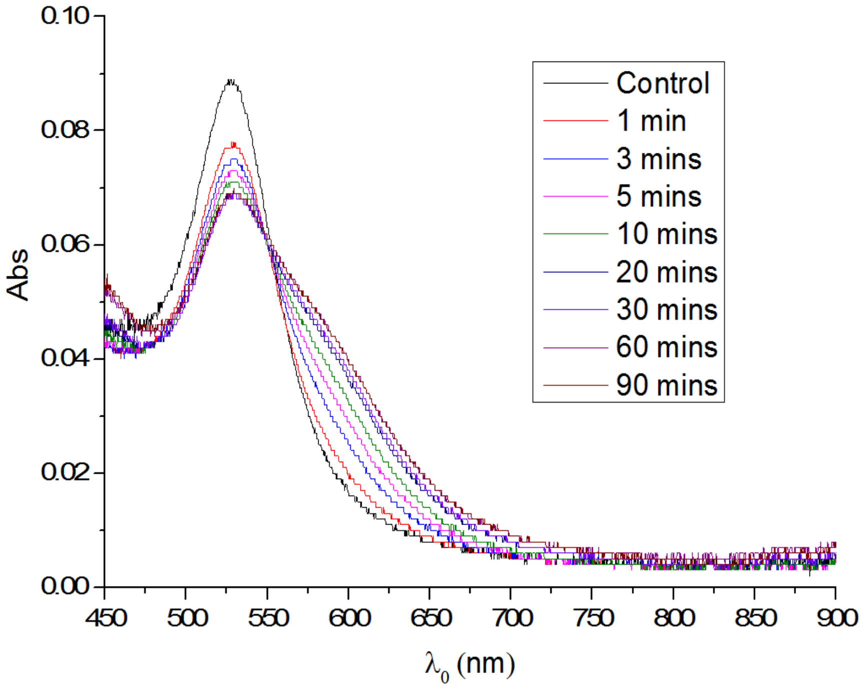

Figure 6.1. Kinetics study of P1000DT mediated dimerisation of AuNP. 360 µL of 40 nm AuNPs OD_{530nm} = 0.09, from BBI solution) were mixed with 40 µL of 2 mM P1000DT (Sigma Aldrich) in a plastic cuvette. The absorbance spectra (coloured lines) were taken by an Ocean Optics hr4000 spectrometer (see Chapter 2) at various time points after the reaction started, as labelled.

0.4 mM P1000DT was then tested with citrate stabilised AgNP (BBI Solutions, OD_{400nm} = 0.2, equivalent to 0.39 x 10^{10} particles/mL[1]). Soon after the start of the reaction, the LSPR peak of the AgNP at 420 nm (referred as "monomer peak" here) started to gradually decrease, and a new absorbance peak at around 480-500 nm region gradually appeared within 2 hour time period, attributed to the longitudinal mode of the dimer (referred as "dimer peak" here) (**Figure 6.2**). According to "plasmon-ruler equation" (see **Section 1.3.1**)(Yang *et al*. 2010), to produce such spectral band, the interparticle distances of the dimer in the solution should be 7 to 10 nm, which is close to the contour length of P1000DT. The amplitude of the AgNP dimer peak

---

[1] Note that for AgNPs, BBI Solutions only provided the OD_{400nm}; the particle concentration (particles/mL) has been calculated using the specification available for nominally identical citrate-stabilised spherical 40 nm AgNPs from nanoComposix.

in **Figure 6.2** is significantly smaller than the AuNP dimer peak in **Figure 6.1**. A possible explanation is the fact that the concentration of AuNPs in the solution was 2 times higher (in number of particles per mL) than that of the AgNP solution. Hence, collisions between AgNPs were less frequent, and the kinetics of dimerisation was slower in the AgNP-P1000DT solution. Also, the kinetics is determined by multiple factors, such as metal-thiol affinity, which can be different for Au versus Ag. Since the silver stock from the supplier has a somewhat lower concentration (nominal OD_{400nm} = 4, equivalent to 9 x 10^{10} particles/mL), we decided to keep the concentration of AgNP constant at OD_{400nm} = 0.2 (0.39 x 10^{10} particles/mL) for all the dimerisation reactions in solution and study the effect of varying concentrations of P1000DT.

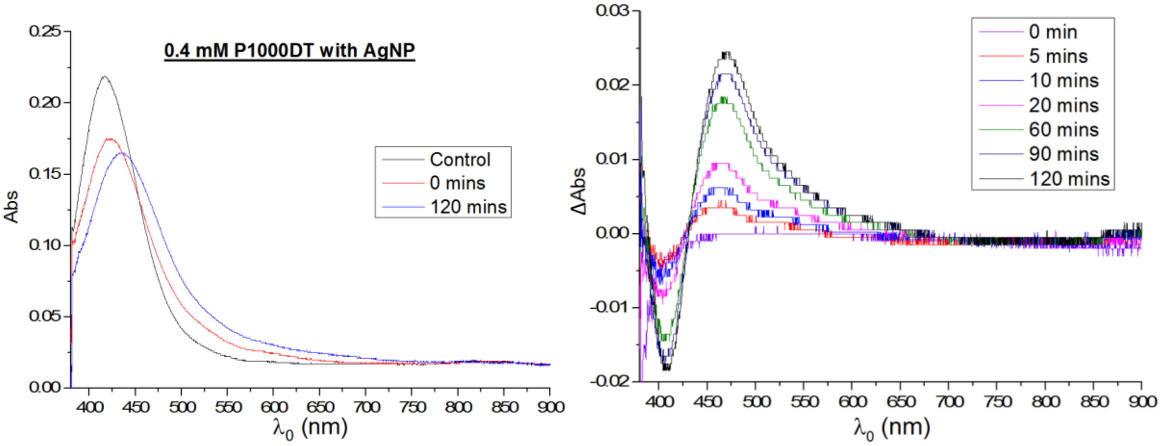

Figure 6.2. Absorbance spectral changes of AgNPs (OD_{400nm} = 0.2) mixed with 0.4 mM P1000DT. **Left**: deionised water was used as the reference for calibration of the spectrometer. 10 fold dilution of the AgNP stock (OD_{400nm} = 2) was used as the negative control. A few seconds after mixing the AgNPs with P1000DT (red line) was set as time 0. **Right**: The spectrum of the reaction solution at time 0 was used as the reference for calculating the absorbance, ΔAbs = (Abs at t mins) - (Abs at 0 mins) (see Chapter 2), for better visualisation of the spectral changes.

Various concentrations of P1000DT were tested to investigate the coating mechanism. (**Figure 6.2 and 6.3**) show that for all four concentration tested, shortly (within seconds) after mixing P1000DT with AgNPs, the monomer peak at 420 nm red-shifted by a few nm. This is a sign of the polymer being adsorbed onto the surface of AgNP (Sharma *et al*. 2014). In all cases, there was also an increase in the long-wavelength tail by various amounts, which is an indication of dimer formation in the first few seconds (time 0). The higher the concentration of P1000DT used was, the stronger was the amplitude of the initial dimer peak observed at time 0. It is well known that thiol has high affinity with fast kinetics toward the Ag surface (Toh *et al*. 2014), thus, once the P1000DT was added to the solution, the polymers were adsorbed onto the AgNP within seconds. When the concentration of P1000DT was high, it is likely that some of the P1000DT molecules had their thiol groups on each end simultaneously absorbed onto two different NPs, before the AgNP surface was fully passivated; this likelihood increased at higher P1000DT concentration as the same numbers of AgNP were present in the solution. This can explain why the initial formation of the dimer peak was stronger at higher P1000DT concentration. **Figure 6.3D** shows that after 2 hours incubation with different concentrations of P1000DT, the monomer peak of the AgNPs was decreasing in amplitude as the concentration of P1000DT increases. The amplitude of the dimer resonance also increased as the concentration of P1000DT increased from 0.01 mM to 0.4 mM. Interestingly, however, at the highest P1000DT concentration of 0.8 mM the dimer resonance showed a smaller amplitude. A possible explanation is that, at very low concentration of P1000DT, the surface density of P1000DT on each AgNPs is relatively low. The polymers form a “mushroom” conformation, that is, one end of a polymer attaches to the surface, and the rest of the polymer body forms a random globular structure in the solution (Damodaran *et al*. 2010). Furthermore, the surface polymers are more likely to form a loop (both thiol groups adsorbed onto the AgNPs). Therefore, the dimers are less likely to form from free collisions. As the concentration of P1000DT increases, the surface density of polymers also increases. The surface polymers start to form a mushroom or even brush conformation instead of loops, which means more surface thiols are available for dimerisation during free collision. This process is however counteracted by the increased passivation of the AgNP surface. Therefore, with increasing concentration of P1000DT, the kinetics of dimerisation becomes more or less constant. For the reaction with 0.8 mM P1000DT, the initial dimer peak was the highest, those dimers might later become large aggregates and precipitate out of the solution. At high concentration, the leftover free polymer that has a hydrophilic backbone and hydrophobic tails (thiol) might form aggregates that trapped and precipitated AgNPs. We decided to use 0.4 mM P1000DT for all the dimerisation reactions in this report.

To confirm that AgNPs were dimerised with P1000DT via covalent bonding of thiol-Ag, a control experiment was designed where 0.4 mM P1000DT was first mixed with 40mM of NEM for 30 mins. This alkylating reagent reacts with sulfhydryls on PxDT and non-reversibly forms stable thioether bonds, so that all the thiol groups on P1000DT were capped (as confirmed by Ellman’s reagent, data not shown). The quenched P1000DT (final concentration of 0.4 mM) was then mixed with AgNPs. **Figure 6.4** shows that the quenched P1000DT was not causing spectral change of AgNPs, showing that the free thiol groups on the P1000DT were essential for dimer formation

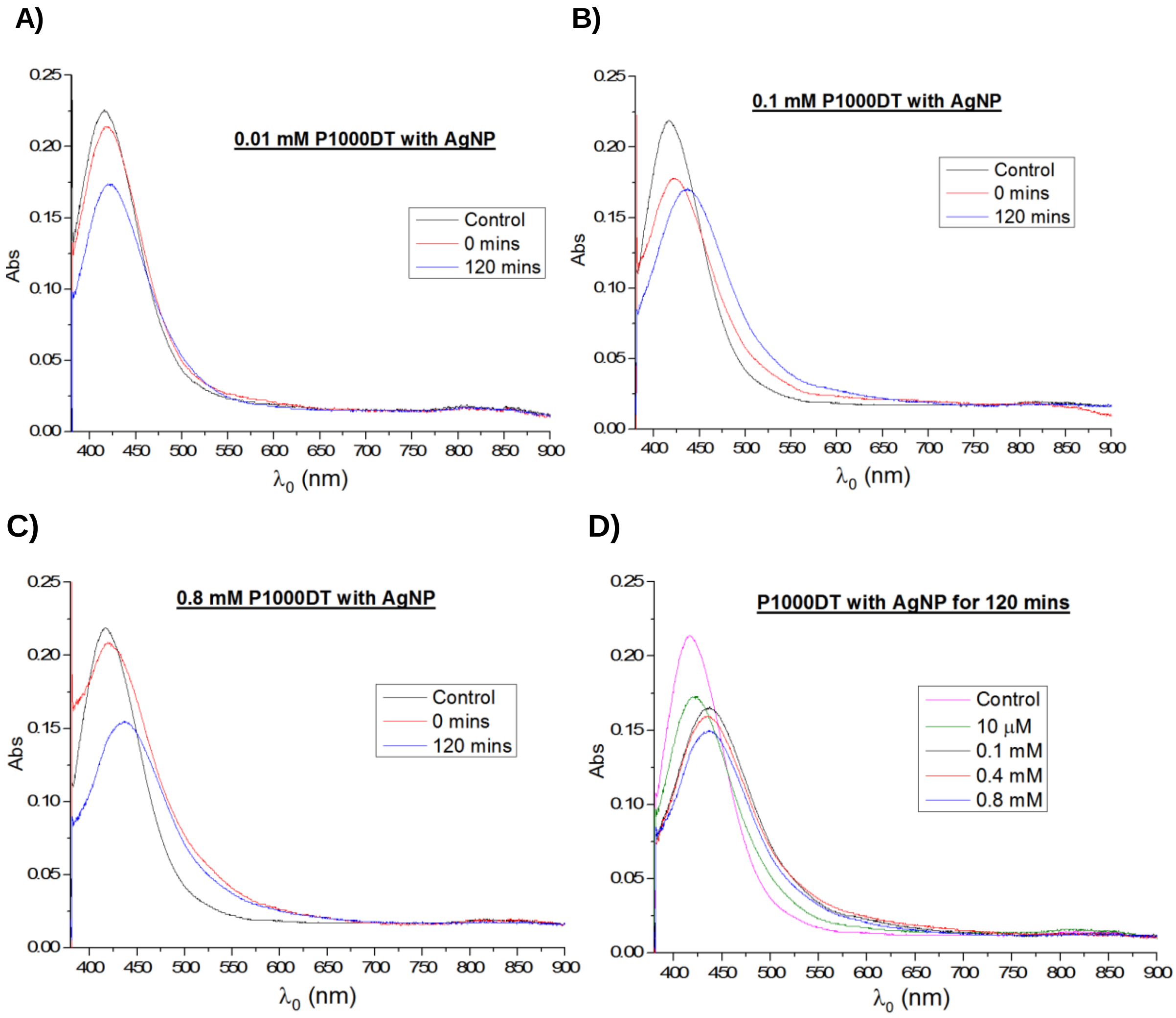

Figure 6.3. A) to **C)** Spectral changes of a AgNP solution (OD_{400nm} = 0.2) mixed with various concentrations of P1000DT. The spectra of the AgNP solution diluted only with water are the 'control'. Soon after mixing the AgNP with P1000DT, the spectra of the reaction solution were taken as '0 mins'. **D)** The spectra of the reaction solution with different concentrations of P1000DT all at 120 mins time point were plotted on the same graph for comparison.

.

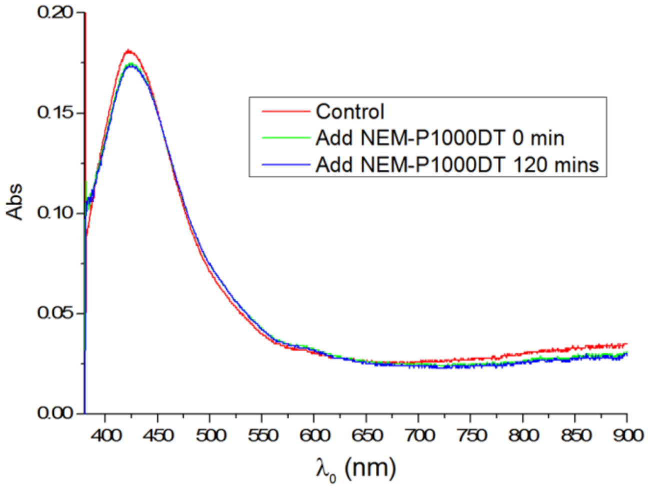

Figure 6.4. Absorbance spectra of an AgNP solution (OD_{400nm} = 0.2) mixed with 0.4 mM P1000DT quenched by 4 mM NEM after 2 hours.

PxDT with various numbers of ethylene oxide units are commercially available (**Table 6.5**).

Commercially available PxDTs

name	MW	# of unit	Contour Length in nm
P180DT	182.3	2	0.7
P300DT	314.46	5	1.75
P1000DT	1000	21	7.35
P1500DT	1500	32	11.2
P3400DT	3400	75	26.25

Table 6.5. PxDT with various number of ethylene oxide units, the contour length was calculated from the structural formula of the polymer with bond length from (William M. Haynes 2015).

It has been demonstrated in the literature that both AuNP (Sonnichsen *et al*. 2005) and AgNP (Yang *et al*. 2010) dimers showed significant spectral shifts due to the dimer formation in the 2 - 20 nm inter-particle separation range. Therefore, P300DT and P1500DT were purchased and tested on AgNPs.

Again, different concentrations of P300DT were used for dimer formation to find the optimum value. **Figure 6.6** shows that after 3 hours incubation with 0.1 mM of P300DT, there was a new absorbance peak in the 580 nm region, which was more red-shifted than the dimer peak appearing when using P1000DT, indicating stronger plasmon coupling at smaller interparticle distance (estimated to be ~ 2 nm when calculated with **eq 1.6**). There was no significant spectral change at a concentration of P300DT higher than 0.1 mM or lower than 0.01 mM (data not shown here). One possible explanation is that the size of P300DT (1.75 nm) is about 4 times smaller than that of P1000DT (7.35 nm), and it is less coiled hence it can be packed at higher density on the surface of an AgNP to form a Self-Assembled Monolayer (SAM); this would happen at high concentration. Because of its smaller size, it is also more likely for the grafted P300DT to form the loop conformation at very low concentration. Therefore, at either high or low concentration AgNPs can be well passivated in different manners, both hindering the dimer formation.

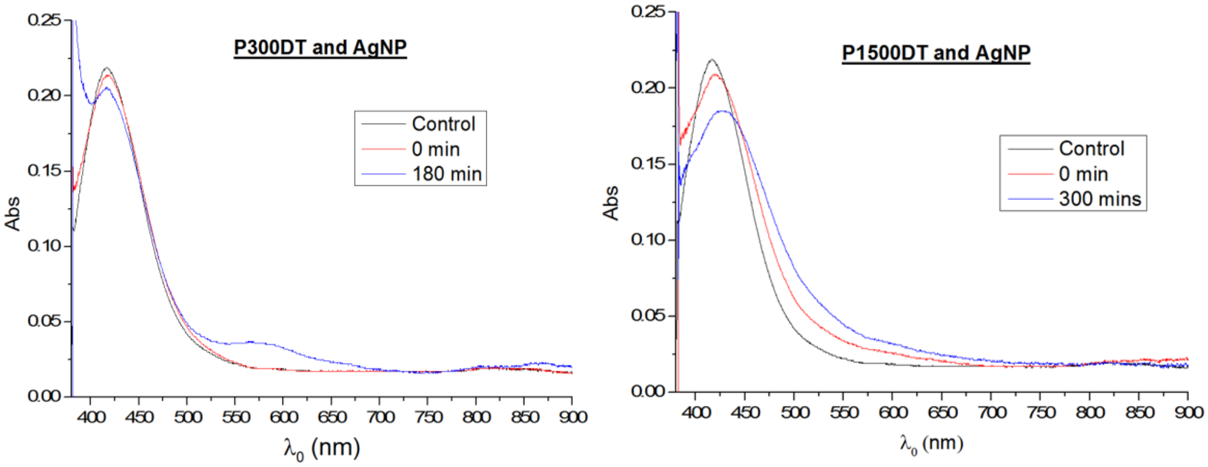

Figure 6.6. Spectral change of an AgNP solution (OD_{400nm} = 0.2) mixed with 0.1 mM P300DT for 3 hours (**Left**); and mixed with 0.5 mM P1500DT for 5 hours (**Right**).

Various concentrations of P1500DT were also tested with AgNPs. **Figure 6.6** shows that after 5 hours incubation with 0.5 mM of P1500DT, there was a new absorbance band on the red-shifted tail. Since the red shift is small, within the bandwidth of the monomer peak, it is not straightforward to obtain the position of the dimer peak from this spectroscopy data. At concentrations lower than 0.1 mM, no dimer band was observed (data not shown). One possible explanation is that P1500DT is a relatively large polymer with backbone more likely to coil up with the hydrophobic thiol groups buried in hydrophilic backbone, hence the grafting density of P1500DT would be lower than that of P1000DT due to steric hindrance which results in the mushroom confirmation. At low concentration (<0.1 mM), the number of free thiol groups was too low for dimer formation.

6.2 NP immobilisation via settlement

One of the goals of the dimer fabrication described above was to study the optical properties of individual AgNP dimers immobilised on a solid substrate, ideally with the correlative imaging techniques described in the previous chapters. NP immobilisation via spin coating is a common technique for even deposition of nanoparticles onto a flat surface such as a glass coverslips. **Figure 6.7 (Left)** shows evenly distributed AgNPs on a Piranha etched coverslip after spin-coating the coverslip with a diluted citrate-stabilised AgNP solution. During the Piranha etching procedure (**Scheme 2.3**), the acid catalyses Si-O bond cleavage on the glass surface; the resulting silanol groups are chemically more active in aqueous environments and they are able to form hydrogen bonding with the ether group on each ethylene oxide unit of the PEG molecule (**Scheme 6.8 C**) as well as with the citrate molecules. However, when deionised water was used as the surrounding medium for DF imaging, a large number of the immobilised AgNPs on the coverslip detached and floated in the medium, after a few hours incubation. A possible cause for this unexpected behaviour is that the glass surface of the coverslip is designed to be extremely flat, and there was only a monolayer of silanol groups available for water mediated hydrogen bonding (Cypryk and Apeloig 2002). Therefore, the binding energy between the AgNP and the glass was too weak. When surrounded by silicone oil, the weak hydrogen network between AgNPs and glass was surrounded by the viscous hydrophobic medium and it was less likely to be disturbed. On the other hand, in the aqueous medium, there are constant exchanges of water molecules in a weak hydrogen network. The binding between the AgNP and glass surface was much less stable.

In order to achieve a stable immobilisation of AgNPs on a glass surface for our optical studies, the coverslips were functionalised with APTES (see materials and methods). The amine group of APTES does not only readily catalyse the formation the silane layers (Kobayashi *et al*. 2005) but also creates sites for a water mediated hydrogen bonding network (**Scheme 2.3**). Thereby the functionalisation promotes immobilisation of AgNPs with hydrophilic coating onto the glass substrate. (Zhu *et al*. 2012) showed that APTES-derived layers prepared in solution are multilayers, forming a net of hydrogen bonding via the primary amine group. This activated substrate surface potentially is able to capture the AgNPs in the solution upon random glass-AgNP collisions. Furthermore, the primary amine group is known to have a strong affinity towards silver and gold surfaces, hence APTES can potentially strengthen the AgNP substrate binding**. Figure 6.7 Mid.** shows that after incubating an AgNP solution on the APTES functionalised coverslip for 10 mins, some AgNPs were able to settle onto the functionalised surface with even distribution. In comparison with the spin-coating technique, this settlement technique requires less AgNP concentration to achieve the same NP density on the substrate. In fact, the surface density can be controlled by the concentration of AgNP solution used in the incubation step. **Figure 6.7 Mid)** and **Right)** show that using a 20x more concentrated AgNP solution resulted an equivalent increase in the AgNP density on the substrate. Most importantly, the settled AgNPs were stable in both water and oil, i.e. detachment of AgNPs was not observed during the measurement period.

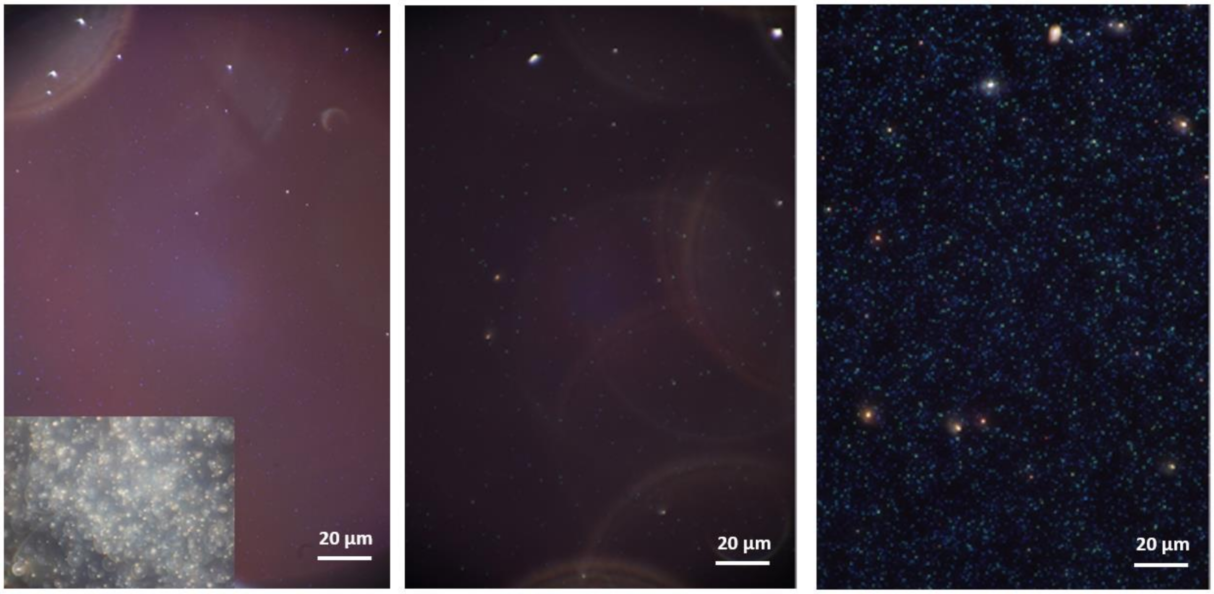

Figure 6.7. Dark field images of sample coverslips with different AgNP immobilisation techniques. **Left**): 20 µL AgNP solution ($OD_{400nm} = 8.3 \times 10^{-2}$, 1.9×10^{9} particles/mL) were used for spin-coating a Piranha etched glass coverslip, the sample coverslip was then mounted with deionised water for imaging. The **insert** at the lower left corner showed AgNP detachment (moving about) in some areas of the same coverslip. **Mid)** 300 µL of AgNP solution ($OD_{400nm} = 4.2 \times 10^{-3}$, 9.45×10^{7} particles/mL) were incubated on an APTES functionalised coverslip for 10 mins; the sample coverslip was then mounted with deionised water for imaging. **Right**) 300 µL of AgNP solution ($OD_{400nm} = 8.3 \times 10^{-2}$) were incubated on an APTES functionalised coverslip for 10 mins; the sample coverslip was then mounted with silicone oil for imaging.

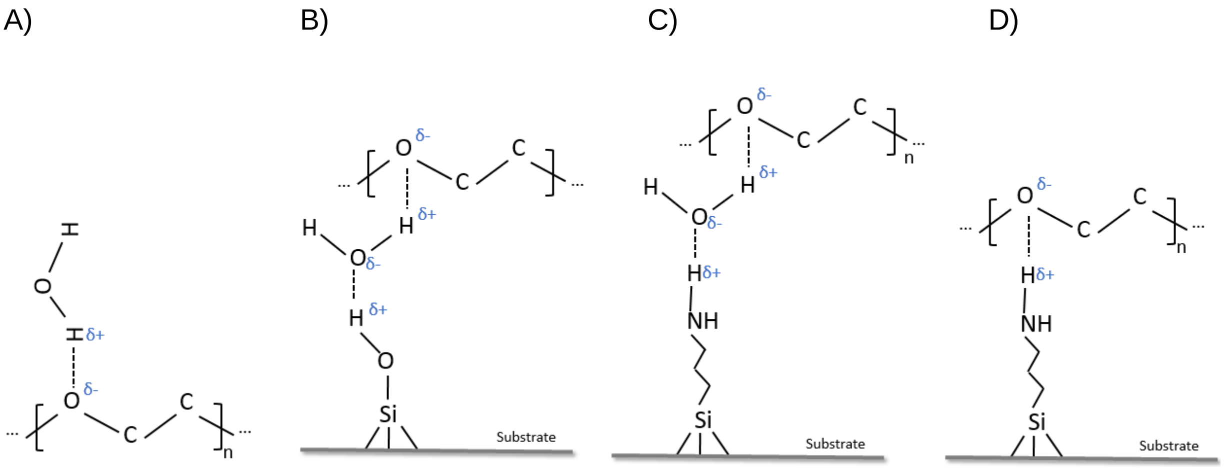

Scheme 6.8. A) Hydration on the backbone of a PEG molecule upon dissolving PEG into an aqueous solution. **B)** PEG interacts with an activated glass surface via water mediated hydrogen bonds. **C)** PEG interacts with an APTES functionalised glass surface via water mediated hydrogen bonds, there is also a host of more complicated interactions shown in **Scheme 2.3. D)** In the absence of water, PEG binds to an APTES functionalised glass surface via hydrogen bonds.

6.3 P1000DT mediated dimer formation, statistical analysis

A quantitative wide-field extinction microscopy method was developed in our lab (Payne *et al*. 2015; Payne *et al*. 2013; Payne *et al*. 2018), which allows us to measure the extinction cross-section of hundreds of individual NPs on a BF transmission image. The BF image can be taken with a monochrome camera, such as the PCO, and bandpass filters were used with the white-light illumination for wavelength selection (for details of the set-up see **Chapter 2**). For example, the extinction cross-section of a single NP calculated from the BF images taken with a bandpass filter Semrock 530/43 (43 nm bandwidth, centred at 530 nm) is the spectral average σ_{ext} within that filter bandwidth (in this case, 506 nm to 553 nm). A range of colour filters across the visible light spectrum were used to obtain σ_{ext} in the bandwidths of interest on the spectrum. Because each σ_{ext} value is calculated with absolute units from the BF images, by merging results using different colour filters, one can construct a coarse extinction spectrum of each NP measured in that wide-field within a short time. This technique has high sensitivity (a shot-noise limited sensitivity down to 0.4 nm^2 was demonstrated in Payne *et al*. 2018) and in turn can detect single 5 nm diameter AgNPs and AuNPs well above the noise limit (a 5 nm diameter AuNP has $\sigma_{ext} = 10$ nm^2 and was detected in Payne *et al*. 2018). Notably, an image processing programme (ExinctionSuite, written by Dr. Lukas Payne) was developed in-house for this technique. It calculates σ_{ext} from the acquired BF images (see Chapter 2), and selectively picks up the objects on the image that have an extinction cross-section within a user-defined range, and with a user-defined wavelength dependence (for example σ_{ext} in the green filter bandwidth larger than in the red), such that large aggregates and non-plasmonic debris can be rejected. The data generated from the resulting extinction image can then be used for statistical analysis of the sample, as well as for searching NPs with specific spectral features.

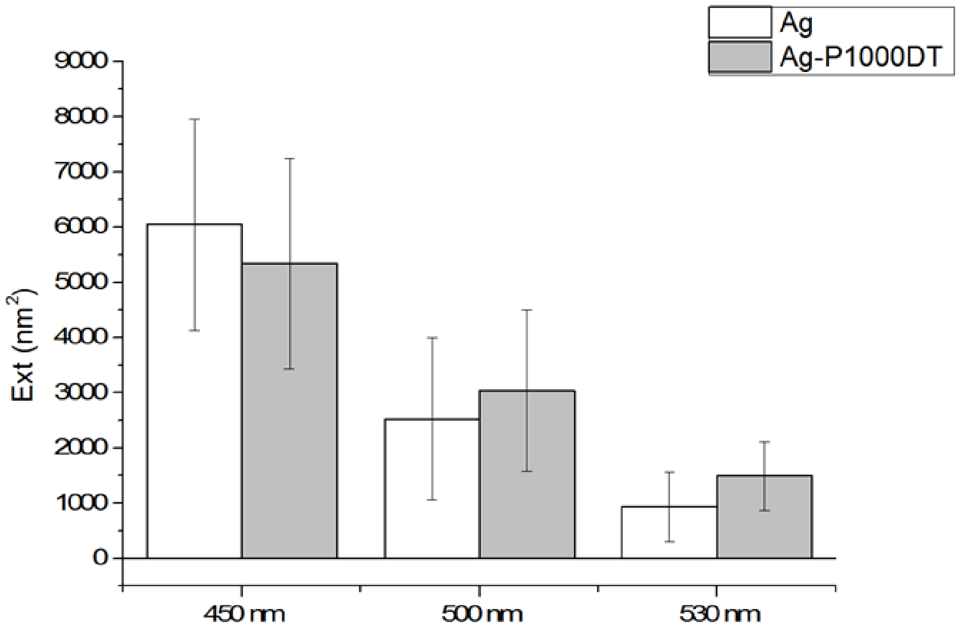

Figure 6.9. Measured extinction cross-sections of a control slide with untreated AgNPs (light bar) and a sample slide with P1000DT-AgNPs (shaded bar), prepared by spin-coating and mounted in silicone oil (n=1.52). On each slide, 3 extinction images (blue, green and red) were obtained with 3 bandpass filters (Thorlabs FB450/40, Thorlabs FB500/40 and Semrock 530/43) respectively. The average values of σ_{ext} in three different channels are presented in a bar chart, the error bar is the standard deviation of the population (120 NPs were analysed in each image).

An AgNP-P1000DT reaction solution (see **Section 6.1**) was diluted and spin-coated onto a piranha cleaned coverslip. The diluted AgNP solution was also spin-coated onto another cleaned coverslip that served as the negative control. Extinction images of the NPs mounted in silicon oil as surrounding medium were taken, and 120 NPs on each image were analysed using ExtinctionSuite. **Figure 6.9** shows the resulting average values of σ_{ext} in three different colour channels, centred at 450 nm, 500 nm and 550 nm, with ~40 nm bandwidth each (see caption). Consistent with the spectroscopy data shown in **Figure 6.2**, adding P1000DT into the AgNP solution caused an increase in the number of NPs with red shifted extinction spectra. It should be noted that most commercially available AgNP products from colloidal synthesis will inevitably have a size and shape distribution. For nominally spherical AgNPs, each NP in the solution has some asphericity. Since the first step of our correlative imaging technique relies on the scattering strength of the AgNPs on the grid to select the candidates for TEM, it is crucial to obtain the quantitative scattering spectrum of a single 40 nm AgNP that has a shape and size close to the average of the batch. To find such AgNP, we looked at the negative control coverslip. Among 120 NPs selected for extinction analysis, one of the AgNPs that has the σ_{ext} close to the calculated average value in all 3 channels was selected for quantitative microspectroscopy. This AgNP is likely to have the average size and shape of the batch. Its scattering spectrum is shown in **Figure. 6.10**. We find a maximum peak cross-section for 120 degrees polariser angle, accompanied with a slight red-shift (5-10 nm) compared to the minimum peak cross-section which is about 17% lower, observed for an orthogonal excitation polarisation, at 30 degrees polariser angle.

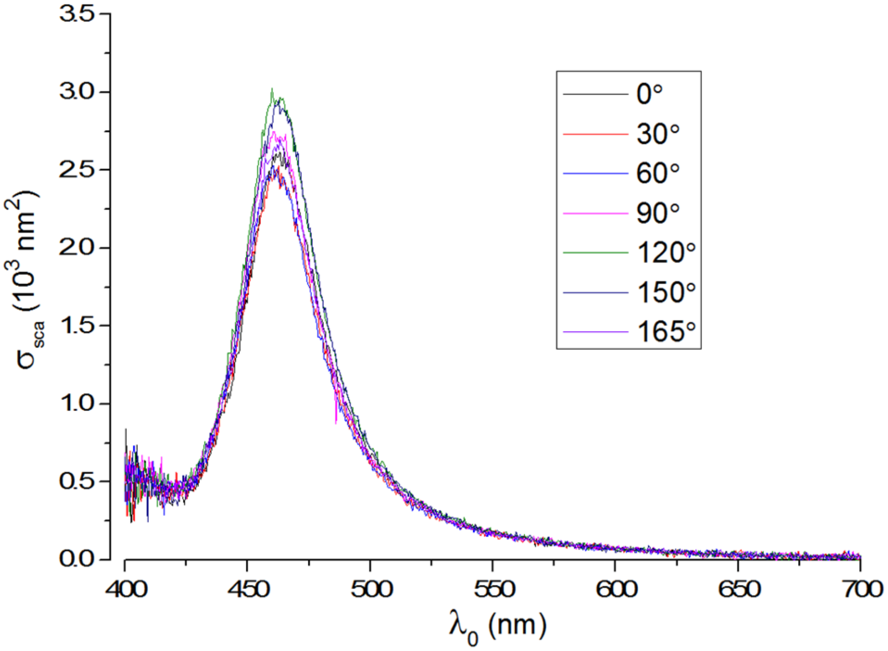

Figure 6.10. Polarisation resolved scattering cross-section spectra of a single 40 nm AgNP in a homogeneous n = 1.52 optical environment, acquired as described in **Section 2.2.4**. The spectra were calculated according to **Section 2.3.2.** The analysis parameters were computed analytically to be: ξ = 4.42, f_{BF} = 0.137, f_{DF} = 0.116 and ζ = 4.42. Different linear excitation polarisation angles as labelled.

The experiment shown in **Figure 6.11** was designed to examine the effect of P1000DT on the optical properties of individual AgNPs as well as on dimer formation in the reaction solution. A Piranha cleaned coverslip was functionalised with 1% APTES. A piece of Press-to-Seal silicone isolator with 4 wells (GraceTM, Bio-Labs) was mounted onto the functionalised side of the coverslip to create 4 compartments, named A to D. Diluted AgNPs (OD_{400nm} = 0.02) were settled in A, serving as a negative control: the immobilised AgNPs were incubated with deionised water before imaging. In B, the effect of P1000DT on the optical properties of individual AgNPs was examined: AgNPs (OD_{400nm} = 0.02) were settled on the coverslip, followed by 15 min incubation in 0.4 mM P1000DT before imaging. In C, the effect of P1000DT on AgNP dimer formation in the reaction solution was examined: 0.4 mM P1000DT was added to the AgNP solution (OD_{400nm} = 0.2); after 15 mins, the AgNPs reaction solution (1 in 10 dilution with water, hence at a similar concentration as for well A and B) were settled in C, then washed with deionised water before imaging.

In each well, one region with AgNPs was chosen, and DF and BF images of that region were acquired. In well A, most of the coloured dots on the DF image of the region (data not shown) were blue with more or less the same brightness, as expected from isolated single AgNPs. The scatter plots in **Figure 6.12** represent a combination of the extinction cross-sections measured for these NPs in the chosen region in the blue (450 nm), green (550 nm) and red (600 nm) channels. Plot A showing data from well A shows that there is only a single cluster of data on the plot, and the cluster is close to the average values of the population. All these data not only can be used as the negative control but also support that the settlement technique immobilised individual AgNP. The cloud plot B shows that incubation with 0.4 mM P1000DT had little effect on the optical properties of the immobilised AgNPs. In contrast, cloud plot C shows that adding P1000DT to the AgNP solution resulted in the formation of a population of AgNPs with red-shifted spectra, manifesting in a significant number of NPs with high values σ_{ext} Detected around 600 nm, indicating that those NPs (appearing as diffraction limited dots on the Extinction image) have a strong plasmon coupling effect, i.e. they were particles in close proximity (<20 nm). Notably this population has a similar σ_{ext} in the blue channel as the population of single AgNPs, consistent with having two NPs (a dimer) where only the transverse mode is detected in the blue due to plasmon coupling of the longitudinal mode. This experiment demonstrated that the formation of the red-shifted population was not caused by aggregation upon immobilisation or a P1000DT induced chemical alteration of individual AgNP, but was a result of P1000DT induced NP coupling via self-assembly in the reaction solution.

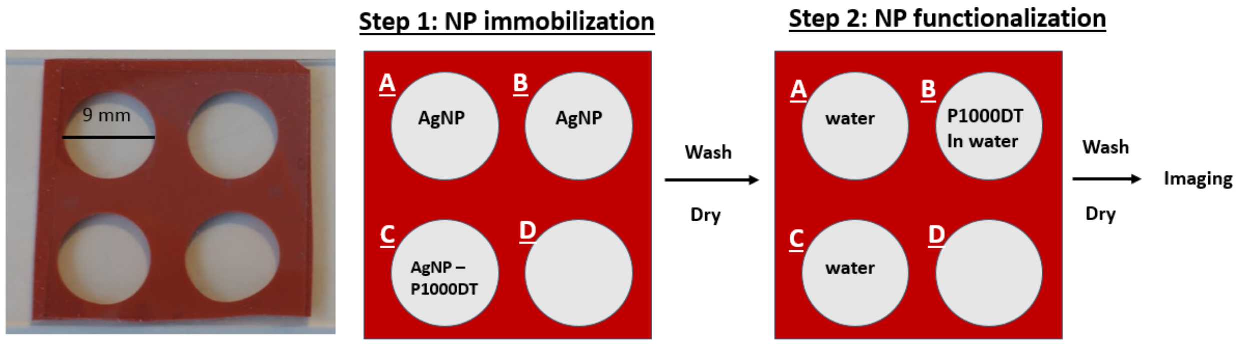

Figure 6.11. Left) Photograph of the sample slide showing wells created by a silica isolator, allowing compartmentalised chemical treatment of NPs in different regions of the same coverslip, prior to imaging. **Right**) Schematic drawing of the experimental steps. In **step 1**, a diluted AgNP solution (OD_{400nm} = 0.02) was settled in well A and well B, while a denser AgNP solution (OD_{400nm} = 0.2) was mixed with 0.4 mM P1000DT then diluted 1 in 10 and then settled on the well C. In **step 2**, NPs in well A and C were incubated in deionised water for 30 mins. NPs in well B were incubated in 0.4 mM P1000DT for 30 mins. Finally the coverslip was washed with deionised water, dried, and then mounted in silicone oil for optical measurements.

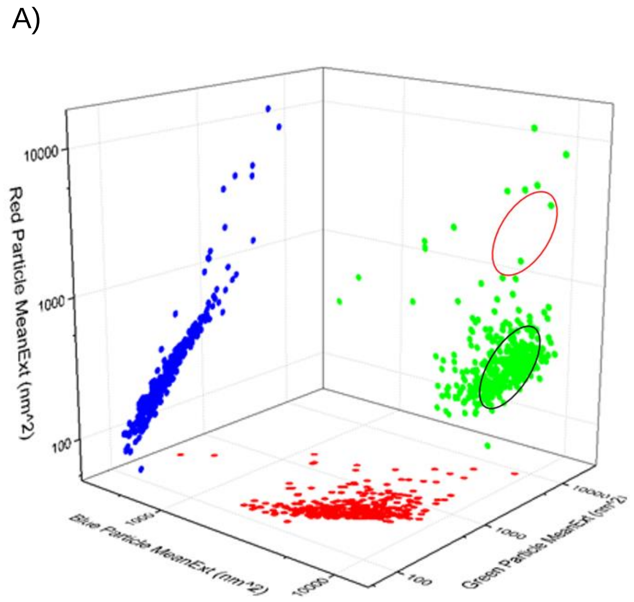

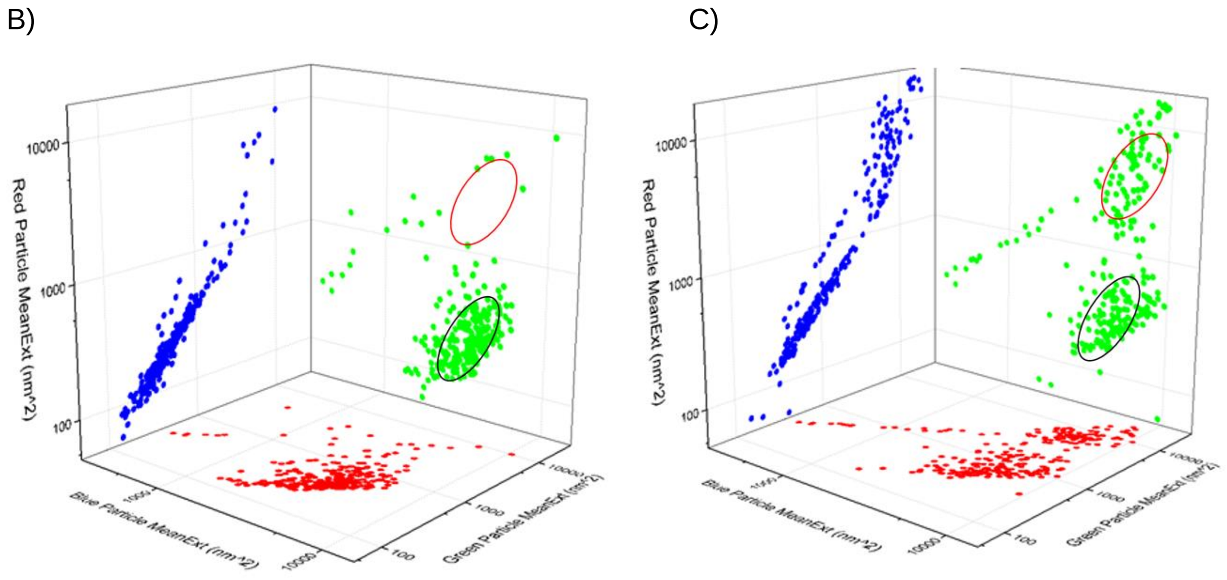

Figure 6.12. Cloud plots A to C representing the data from the extinction images taken from well A to C in figure 6.11 respectively, acquired using a PCO camera with 40x objective, bandpass filters (ThorLabs Visible Bandpass Filter Kit, 40 nm FWHM) centred at 450 nm (blue channel), 550 nm (green channel) or 600 nm (red channel), with 40 nm bandwidth. The measurements are shown as a 3D scatter plot using the cross section in each colour channel, called σ_B, σ_G and σ_R for blue, green, and red respectively, all on log scales. About 100 NPs in each well were selected for analysis. Circled areas are guide to the eyes to indicate different NP populations (see text).

6.4 Correlative imaging

With the aim to perform correlative light electron microscopy of AgNP dimers, we first developed a method to select single particles, likely to be dimers, by dark-field imaging. A single 40 nm diameter spherical AgNP has a sharp LSPR peak in the blue wavelength region (e.g. at 420 nm in water, see ‘control’ spectra in **Figure. 6.2** and **6.3**). Dimerisation and aggregation will cause a red-shift of the LSPR to various degrees (**Section 1.3.1**), depending on the inter-particle distance. We are interested in dimers with inter-particle distances between R/10 and R, with R being the NP radius (i.e. 2-20 nm, for R= 20 nm), which would result in a significant LSPR shift, as estimated by the ‘’plasmon ruler equation’’ (Yang *et al*. 2010), with a longitudinal mode shifting from 420 nm to about 600 nm in water. LSPR shifts within this wavelength range can easily be detected on the DF image taken by a colour camera, as 40 nm AgNPs scatter light strongly at their LSPR. Owing to the large LSPR shifts of silver dimers, one can simply change the polarisation angle of the incident light to observe colour changes going from the transverse to the longitudinal modes of the dimers "by eye". An automated linear polariser was placed in the illumination of the Ti-U lamp, above the condenser. As discussed in Chapter 2, the detection optics and colour camera allow us to observe a relative large number of NPs in a wide field of view, while providing enough spatial resolution to distinguish NPs that are only a few micrometres apart on the DF image. **Figure 6.13** shows a series of DF images of two AgNPs at polarisation angle from 0° to 165° in 12 incremental steps (15° increase for each step). The AgNP on the left always scatters blue light at various polarisation angles, whereas the AgNP on the right has a strong polarisation dependence. Two distinguishable plasmon modes were observed, one at 75° polarisation angle in the blue region of the spectrum (transverse mode), and the other at 165° in green region (longitudinal mode). Furthermore, at 75°, the coloured dot on the right scattered much more strongly than the dot on the left, indicating that there was significant more silver material in the dot on the right within the focal volume. These polarisation resolved DF images suggest that the blue dot on the left contained an isolated single AgNP, whereas the dot on the right contained a dimer with a strong plasmon coupling effect. This simple and fast technique allowed us to identify dimer candidates with 2 selection criteria i) they should appear to have a clear two-mode polarisation response; the transverse mode scatters blue light, the longitudinal mode should scatter green/red light with stronger intensity, and the two modes must be orthogonally polarised; ii) The transverse mode should be brighter (approximately twice) than the mode of a single NP on the DF image at the same polarisation angle. However, the TEM micrograph (**Figure 6.14**) provided by the manufacturer showed that the AgNP stock contains a number of NPs with significant asphericity. The egg-shaped and rod-shaped AgNPs might also satisfy our simple selection criteria. To make sure that AgNP dimers were picked, 12 to 15 candidates on each grid were selected for micro-spectroscopy. To select dimers with various separations, we selected candidates with various colours in the DF images, in order to study the distance dependent plasmon coupling effect.

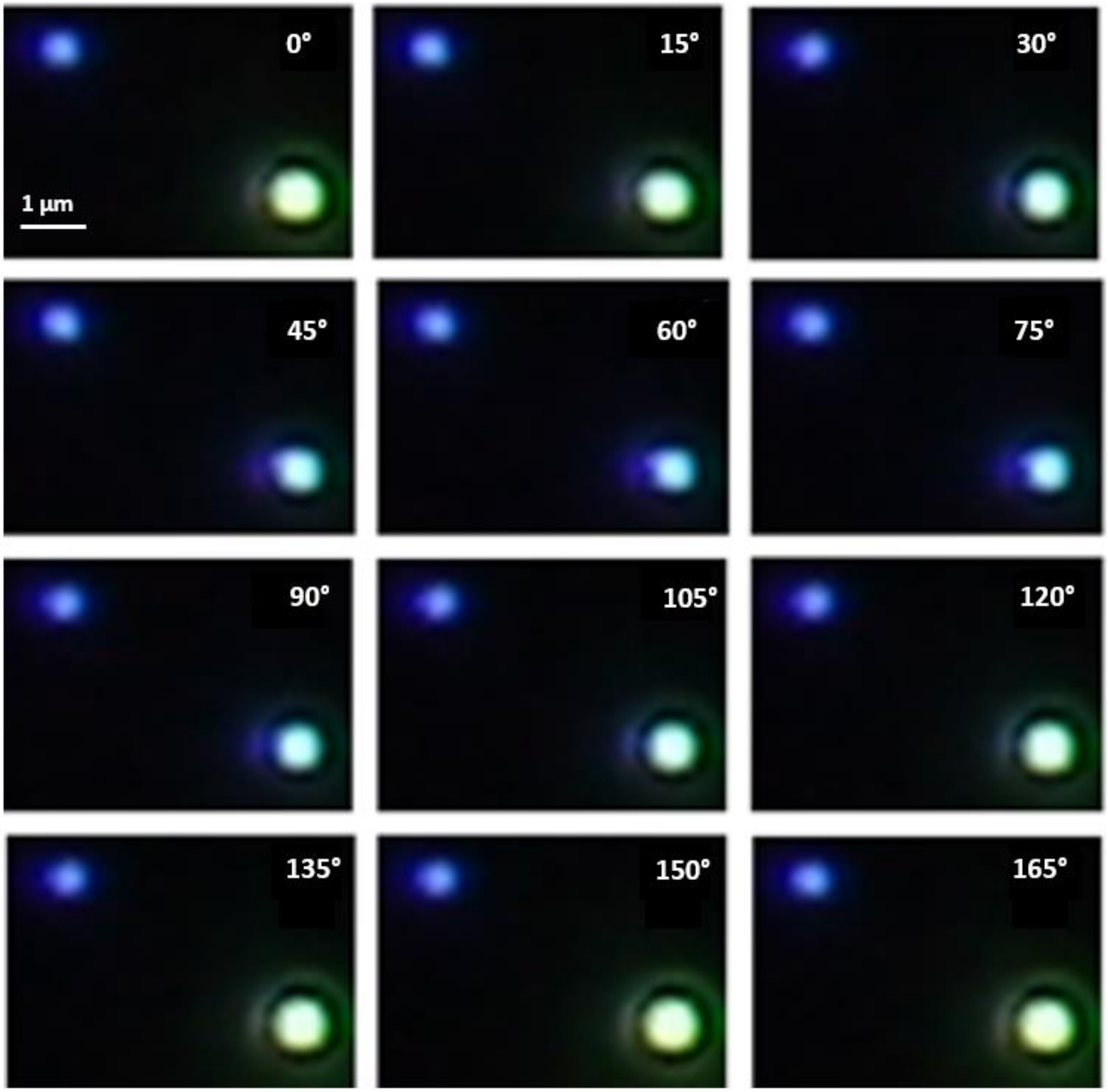

Figure 6.13. Candidate dimer selection by polarisation resolved colour DF imaging (**Section 2.2.3**). AgNP-P1000DT was drop-casted onto a coverslip, and mounted in silicone oil (n = 1.52) for DF imaging. A series of DF images of the same field of view were taken by the Canon colour camera at different polarisation angles from 0° to 165° with 15° for each step.

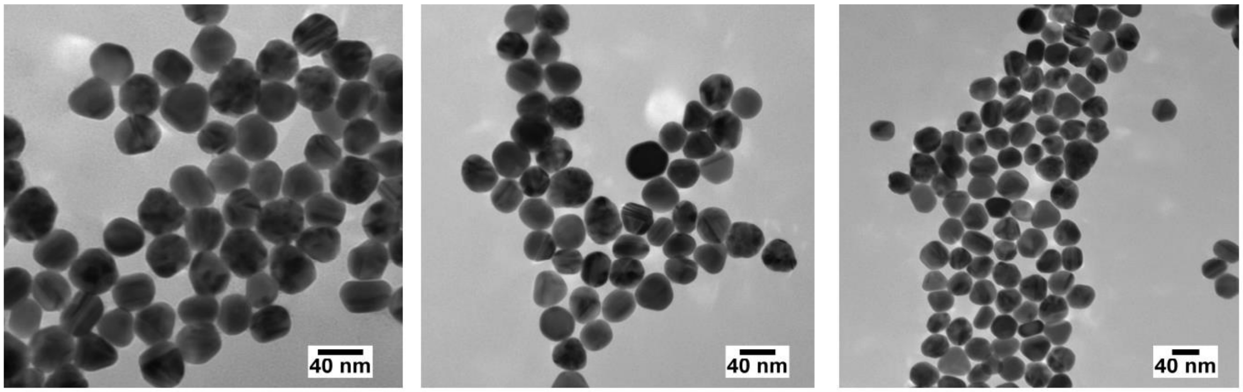

Figure 6.14. TEM data of the sample batch from nanoComposix.

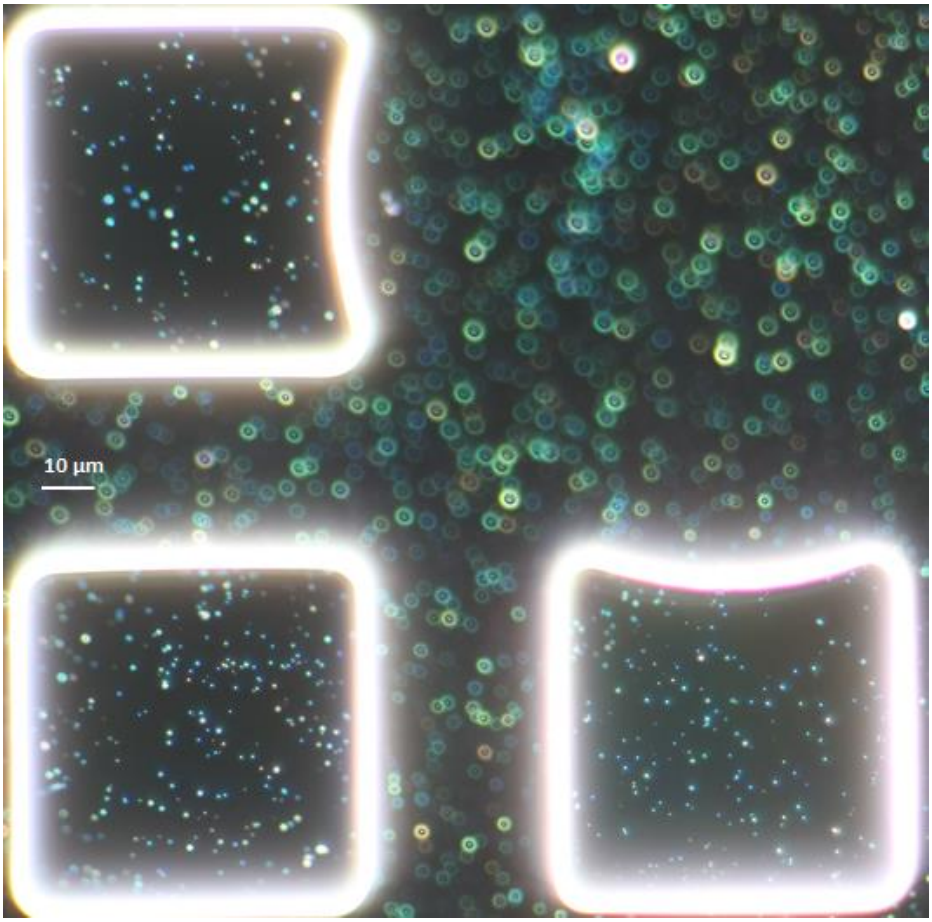

Figure 6.15. 9 µL of AgNP-P1000DT reaction solution (1 in 2 dilution) was dropped onto an APTES functionalised SiO_2 TEM grid and incubated in a humid environment for 15 mins. The DF image (**Section 2.2.3**) (130 x 130 µm^2) shows the settled NPs on the SiO_2 films.

Details on the development of the correlative imaging technique are described in Chapter 2 and 4. For Ag dimers, an AgNP solution (OD_{400nm} = 0.2) was mixed with 0.4 mM P1000DT for 10 mins, the reaction solution was then diluted and NPs in the solution were settled onto an APTES functionalised SiO_2 TEM grid. **Figure 6.15** shows that the settlement technique was able to produce a rather even distribution of NPs on the SiO_2 surface, and that the immobilised NPs were stable after TEM imaging as well as after mounting the sample grid in anisole for 2 or 3 imaging sections.

Among the 32 NPs candidates selected for correlative imaging, using their colour in DF scattering as described above, all of the red-coloured candidates turned out to be small aggregates (3 or more NPs in close proximity within the focal volume), all of the yellow/orange candidates were dimers with very small gap size (<2nm), and all of the green and cyan candidates were elongated single AgNPs, rather than AgNP dimers with large gap size. The latter were found occasionally during random search (without tracking the field of view of TEM with the DF image, for fast searching) and captured on some of TEM micrographs (**Figure 6.17**), but, due to low density, we were unable to find those dimers on the DF images. **Figure 6.16** shows correlative light TEM imaging for 2 single NPs and 3 dimers. Since the polarisation dependences of the NPs on the DF images were used as a guide for selecting all of the candidates, all of the spectra of the candidates shown here have 2 distinctive LSPR modes as expected. TEM micrograph shows that all of the single isolated AgNPs selected have some degree of asphericity. The optical properties of AgNP are highly sensitive to their size and shapes, and in turn also exhibit two LSPR modes as expected for an ellipsoid. The larger the NP is, the greater is the scattering peak amplitude (scaling as R^6 in the dipole limit). The larger the aspect ratio, the more red-shifted is the longitudinal mode. Notably, some elongated single AgNPs have spectra close to a dimer (**Figure 6.16 NP2**). The peak amplitude of the transverse mode of the dimers (NP3 to NP5) were also not significantly stronger than that of a single AgNP in **Figure 6.16**, despite the fact that there were two particles in the focal volume here, possibly due to the different size/shapes of the NPs. This observation is not reported in the literature, as there were no quantitative measurements on the scattering cross-section spectra available previously for such comparisons. In (Yang *et al*. 2010), despite the fact that the candidates were selected under TEM, there were still a variety of sizes and shapes of the AgNP monomers selected for optical measurement. This might explain the poor agreement of their simulations that assume the AgNP monomer to be perfect spherical with the experimental data of dimers with aspherical AgNP monomers. Therefore, the shape, size and the relative orientation of each AgNP monomer of the dimer must be taken into consideration for quantitative analysis and accurate modelling.

NP1

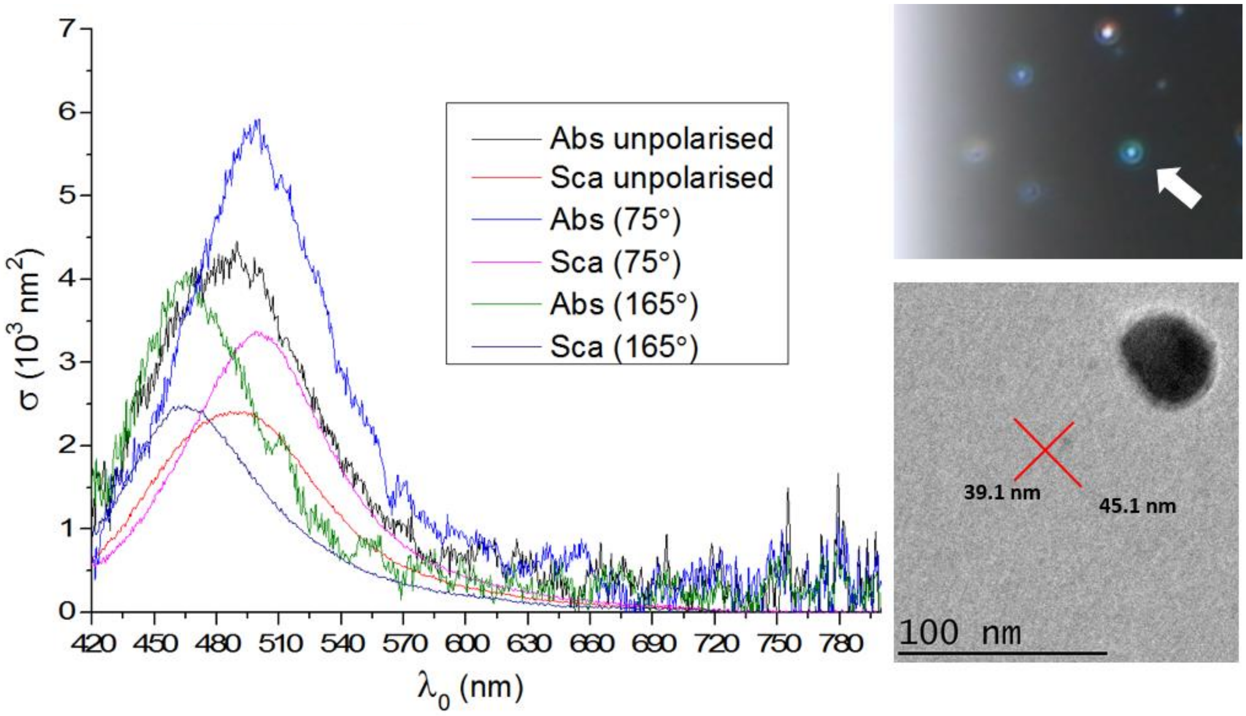

NP2

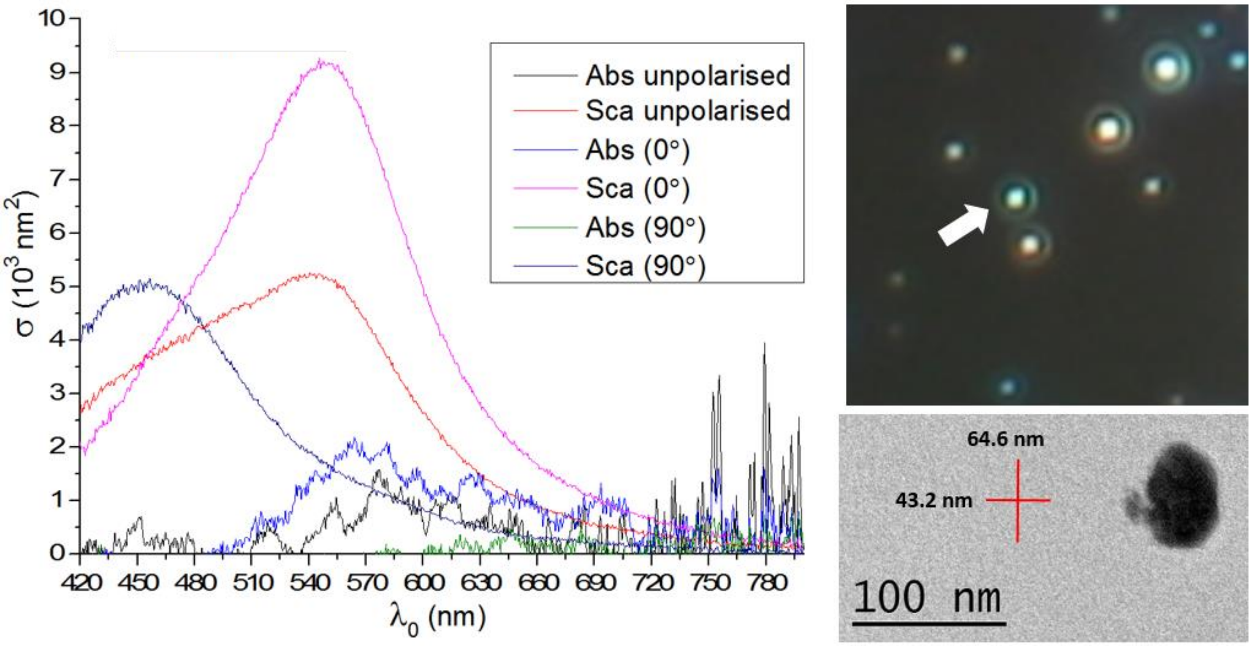

NP3

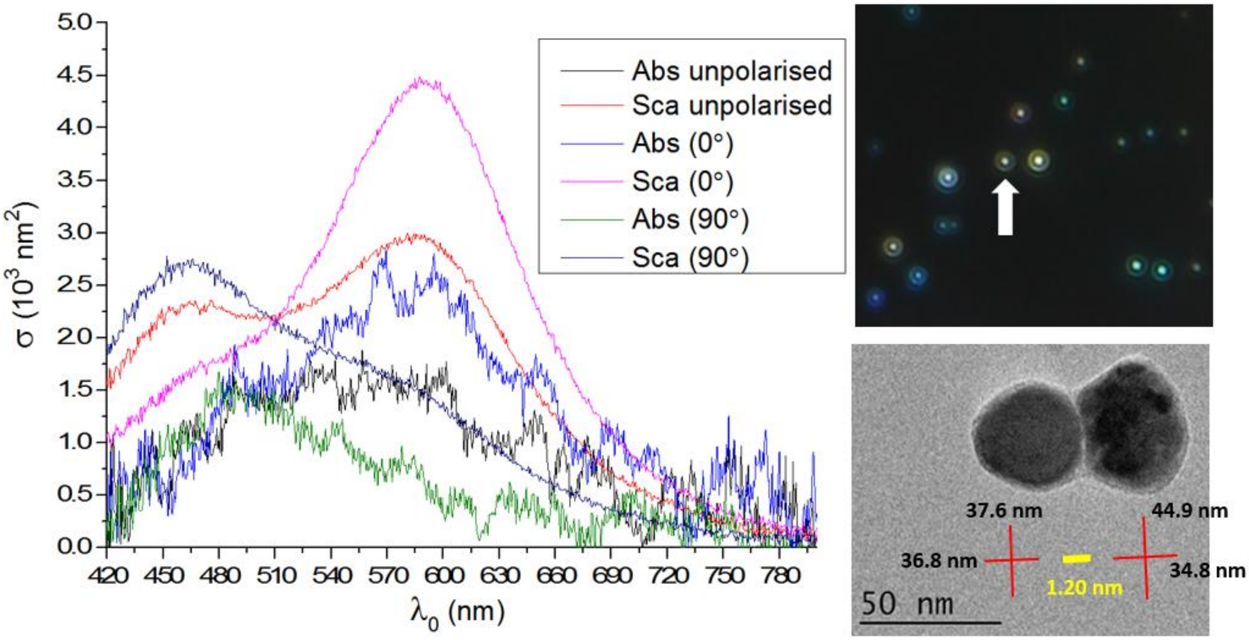

NP4

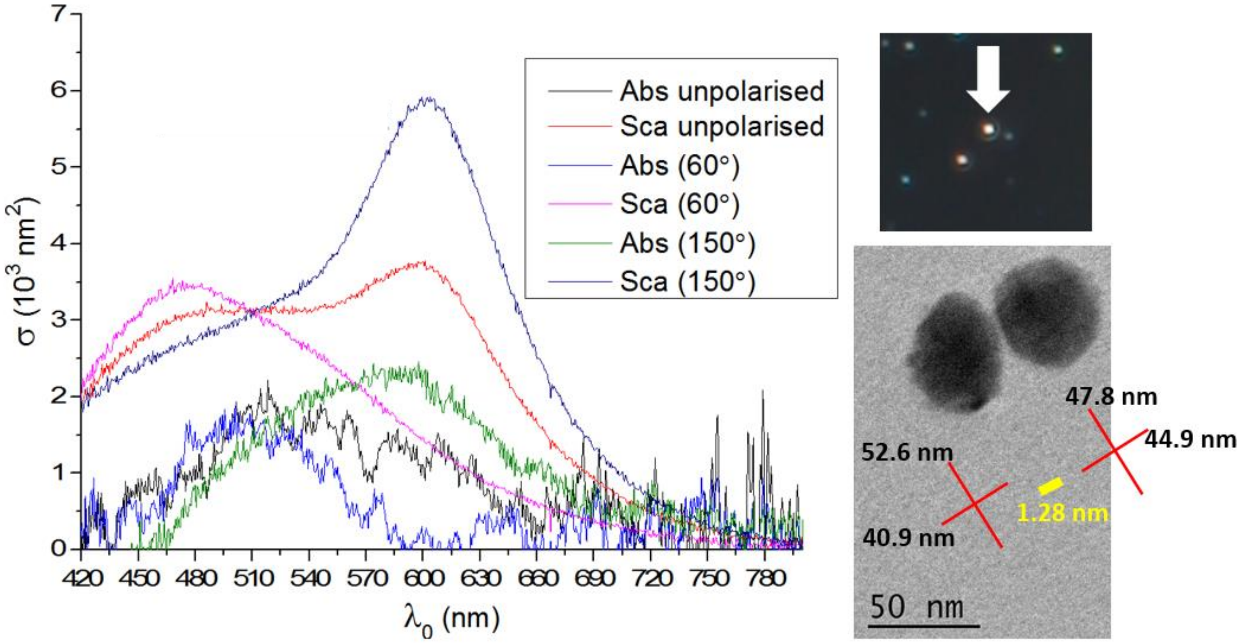

Figure 6.16 Correlative imaging results for AgNP-P1000DT dimers settled on the SiO_2 TEM grid (APTES functionalised). **Left Column** Absolute absorption σ_{abs} and scattering σ_{sca} cross-section spectra of each imaged NP (surrounded by anisole as medium). The spectra were calculated according to **Section 2.3.2**. The parameters for the calculation were ξ =4.42, f_{BF} = 0.137, f_{DF} = 0.116 and ζ = 4.42 for a single AgNP

and ξ = 4.42, f_{BF} = 0.148, f_{DF} = 0.148, ζ = 5.63 for an AgNP dimer. **Right Column** upper panel: DF images, with the investigated NP indicated by a white arrow. Lower panel: TEM micrograph of the NP. For the single NPs, the length of the longest dimension of the single NP as well as the dimension perpendicular (red lines) were measured (black numbers). For the dimers, the longest axis of the dimer and the axis that is perpendicular to the longest axis were used as reference directions. The diameter (red lines) of each AgNP monomers on each axis was measured (black numbers). The interparticle distances on the longest axis of the dimer (yellow lines) were measured (yellow numbers).

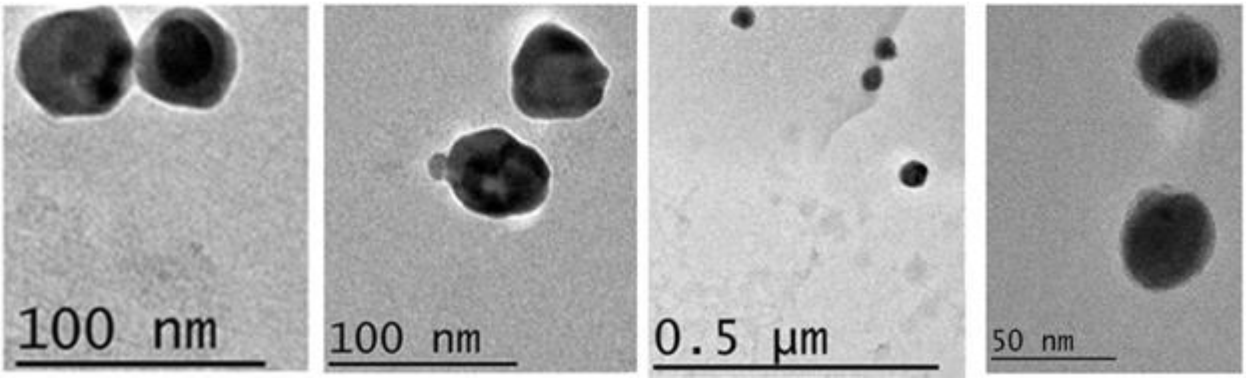

Figure 6.17. Dimers with various gap sizes were occasionally found on TEM micrographs of AgNP-P1000DT dimers.

6.5 Dimers in changing media

During a random search of dimers on the grid, there were only very few dimers with gap size larger than 2 nm. Since those few dimers were found during TEM (i.e. they were not in the optically selected candidate dimer pool) they could not be correlated with DF images. The spectral features of the imaged AgNPs were significantly altered after electron irradiation (**Figure 6.18**). Therefore post TEM optical correlation was deemed not meaningful. It is surprising that we could not find a significant number of dimers with gap >2nm considering the polymer length of the P1000DT (see **Table 6.5**) and the dimer peak measured in solution at around 480-500 nm (see **Figure 6.2**) indicating an average inter-particle length of s ~7 nm.

To understand this phenomenon, we investigated whether the immobilisation onto the TEM grid and the change of the surrounding medium from water (used in solution) to anisole (and eventually air and then vacuum for TEM) could be responsible for the change in inter-particle distance. It is well known that the LSPR peak of an AgNP red-shifts in media with higher refractive index (Ghosh *et al*. 2004. Stewart *et al*. 2008). For example, comparing figure 6.2 with figure 6.10, from water (n= 1.33) to silicone oil (n = 1.52), the LSPR peak of an average 40 nm AgNP red shifted by 30 nm. Interestingly, when AgNP-P1000DT were settled, then washed with water and mounted in water without the drying step, there were a large number of NPs observed in DF imaging with a polarisation dependence and scattering in the green and cyan colour, whereas NPs scattering in the yellow and red colour were hardly found, suggesting that most dimers had >2nm inter-particle distances. When the same samples were subsequently de-mounted and dried in air, then re-mounted in anisole for DF imaging, the number of NPs scattering in the red and yellow did drastically increase (data not shown). This supports the hypothesis that the optical properties of the AgNP dimers are altered during the media exchange procedure, notably involving a drying step, following deposition onto the sample surface.

A)

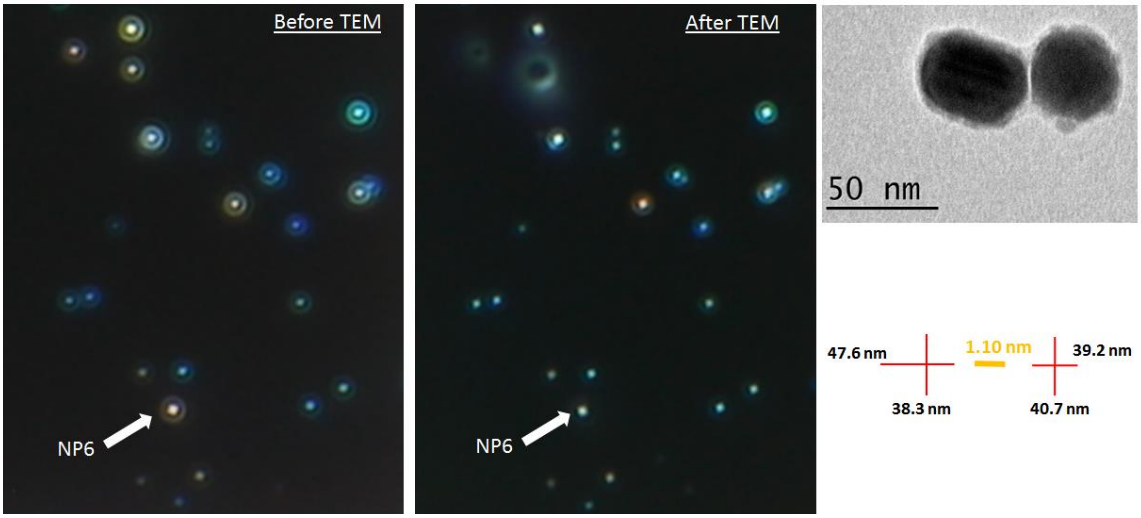

B)

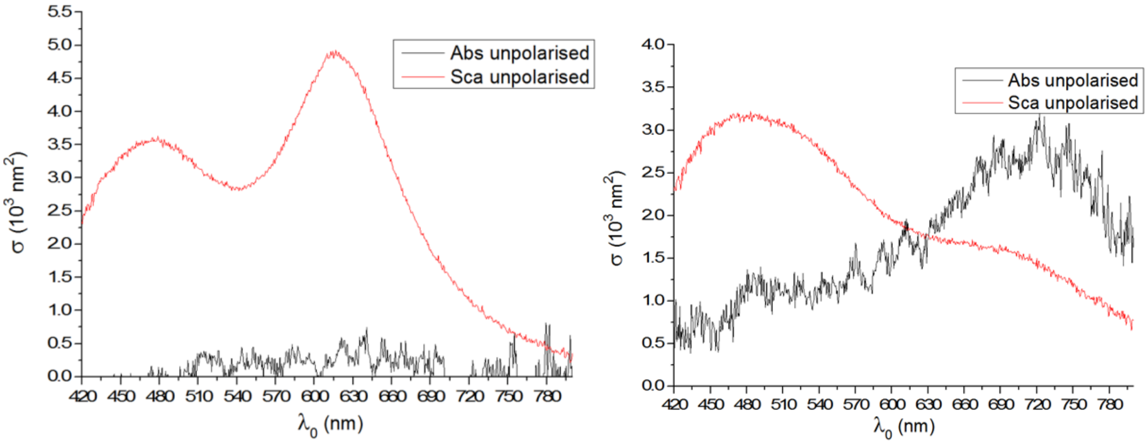

Figure 6.18 TEM induced modification on the optical properties of a NP. **A**) DF image (mounted in anisole) of dimer g7i6p2 (white arrow) before (left) and after (mid) TEM imaging (accelerating voltage 200 kV, beam current 101 μA, 50 to 150 pA/cm^2) (right). **B**) Absolute absorption σ_{abs} and scattering σ_{sca} cross-section spectra of dimer g7i6p2 before (left) and after (right) TEM imaging. The spectra were calculated according to **Section 2.3.2**. The parameters for the calculation were: $\xi = 4.42$, $f_{BF} = 0.148$, $f_{DF} = 0.148$, $\zeta = 5.63$ for AgNP dimers.

The experiment shown in **Figure 6.19** was designed to further investigate the effects of different mounting media as well as the mounting procedure on the optical properties of the immobilised dimers. The settlement technique and mounting procedure using a silicone isolator allowed us to image the same field of immobilised NPs in different mounting media. **Figure 6.20** exemplifies how all of the NPs scattering in the green and bright cyan/blue in step 1 are being red-shifted into yellow or red scattering NPs when transferred from water into anisole after drying in nitrogen in step 2. Notably, this red-shift in colour was not fully reversible after transferring the samples back into water again in step 4. In comparison, the weak blue NPs in step 1 only red-shifted into brighter blue or cyan NPs in step 2 and reversed back to the same colour in step 4. Statistical analysis of 120 NPs in the region confirmed this observation (**Figure 6.21**): a red-shifted population was generated after first transfer from water to anisole, via a drying step; this red-shifted population remained stable when transferred into air and back into water. This suggests that the irreversible red-shift of the dimers/aggregates must be the result of an alteration of the dimer/aggregates inter-particle distances themselves following the media exchange procedure, rather than a change of the surrounding refractive index.

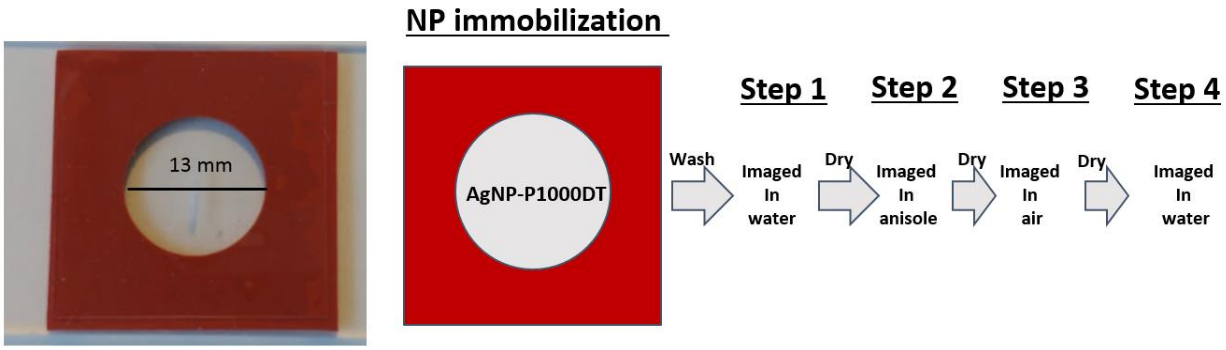

Figure 6.19. Left) Photograph of the sample slide. A single large sample well was created by a silica isolator; the coverslip was marked with a glass cutter on the outer side, so that the same field of view could be found in each experimental steps. **Right)** schematic drawing of the experimental steps: a solution of AgNP-P1000DT was settled onto the inner side of an APTES functionalised coverslip. In step

1 the sample coverslip was washed in deionised water for 3 times; then, without drying, the immobilised NPs were imaged in water. In step 2, 3 and 4, the coverslip was de-mounted and completely dried under nitrogen gas, and the same region of the coverslip was imaged in anisole, air and water respectively.

Figure 6.20 DF images of the same region on the sample coverslip were taken in the experimental steps shown in **figure 6.19** (except DF image of step 3 which is not available as the scattered light from the NP in air was hardly observable).

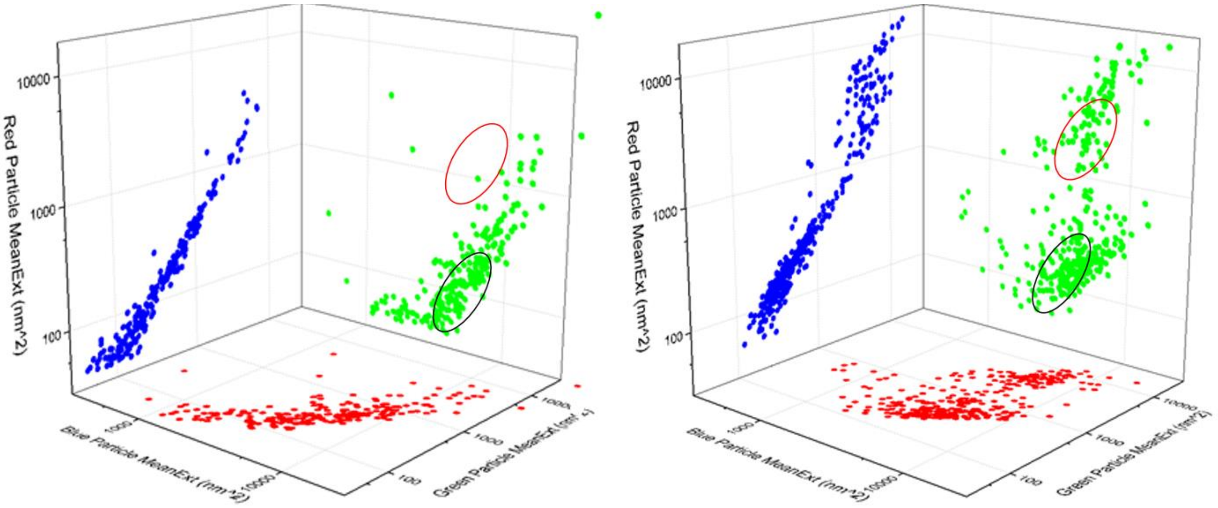
Step 1

Step 2

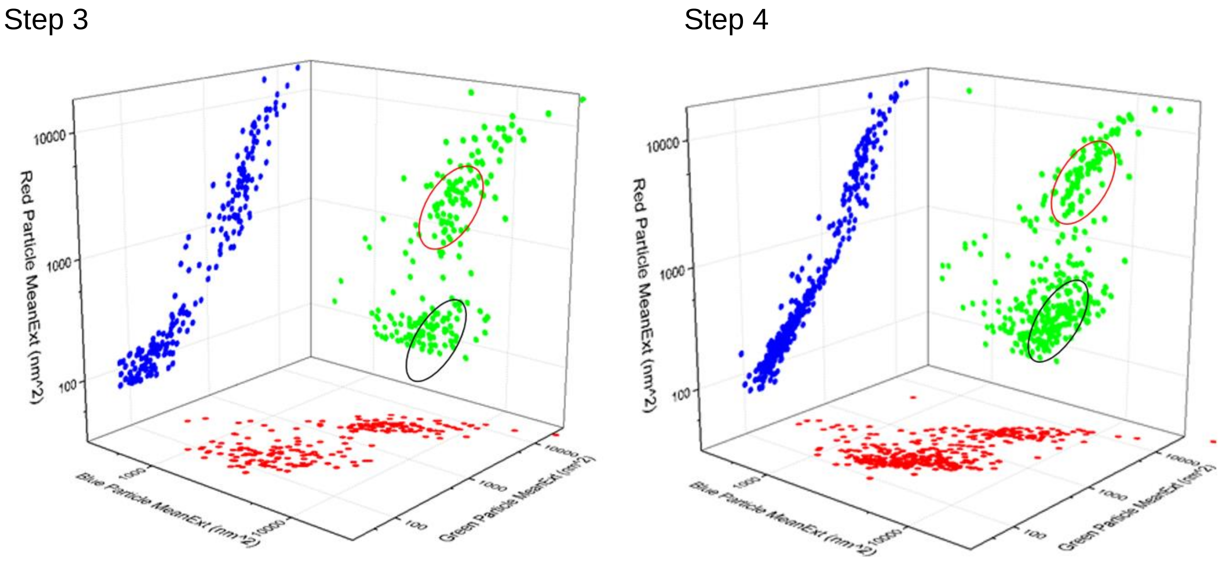

Figure 6.21. Extinction images were taken during experimental step 1 to 4 in **figure 6.19** by a PCO camera with bandpass filter 450 nm (blue channel), 550 nm (green channel) or 600 nm (red channel). 120 NPs on each extinction image were selected for analysis by Extinction-Suite. The results are shown in terms of the quantified cross section in each colour channel, called σ_B, σ_G and σ_R, on each axis of a 3D scatter plot, all on log scales.

Figure 6.22 shows the micro-spectroscopy data of the same single AgNP in different mounting media. The LSPR peak of this AgNP shifted from 430 nm to 450 nm when transferred from water to anisole. This red-shift was completely reversed when the AgNP was transferred back into water, as well as the peak amplitude and position on both σ_{sca} and σ_{abs} spectra after all the experimental steps. This indicates that anisole as well as the mounting procedure had no effects on optical properties of the immobilised *single* AgNP. In contrast, **Figure 6.23** shows the polarisation resolved micro-spectroscopy data in different mounting media of a NP scattering in the green and with a polarisation dependence (thus likely to be a dimer). The longitudinal mode of the NP has peak at λ_{long}. This peak red-shifted more than the resonance peak (at λ_{trans}) of the NP's transverse mode did when the NP was transferred from water to anisole ($\Delta\lambda_{anisole} > \Delta\lambda_{water}$ with $\Delta\lambda = \lambda_{long} - \lambda_{trans}$). The Δλ further increased when the NP was imaged in air ($\Delta\lambda_{air} > \Delta\lambda_{anisole} > \Delta\lambda_{water}$). When transferred back to water, the Δλ decreased, but did not reverse back to its original value. Since we have demonstrated that the experimental procedure and the mounting media had no chemical effect on the individual NPs (**Figure 6.22**), the changes in Δλ were likely due to the changes in the gap-size of the NP dimer.

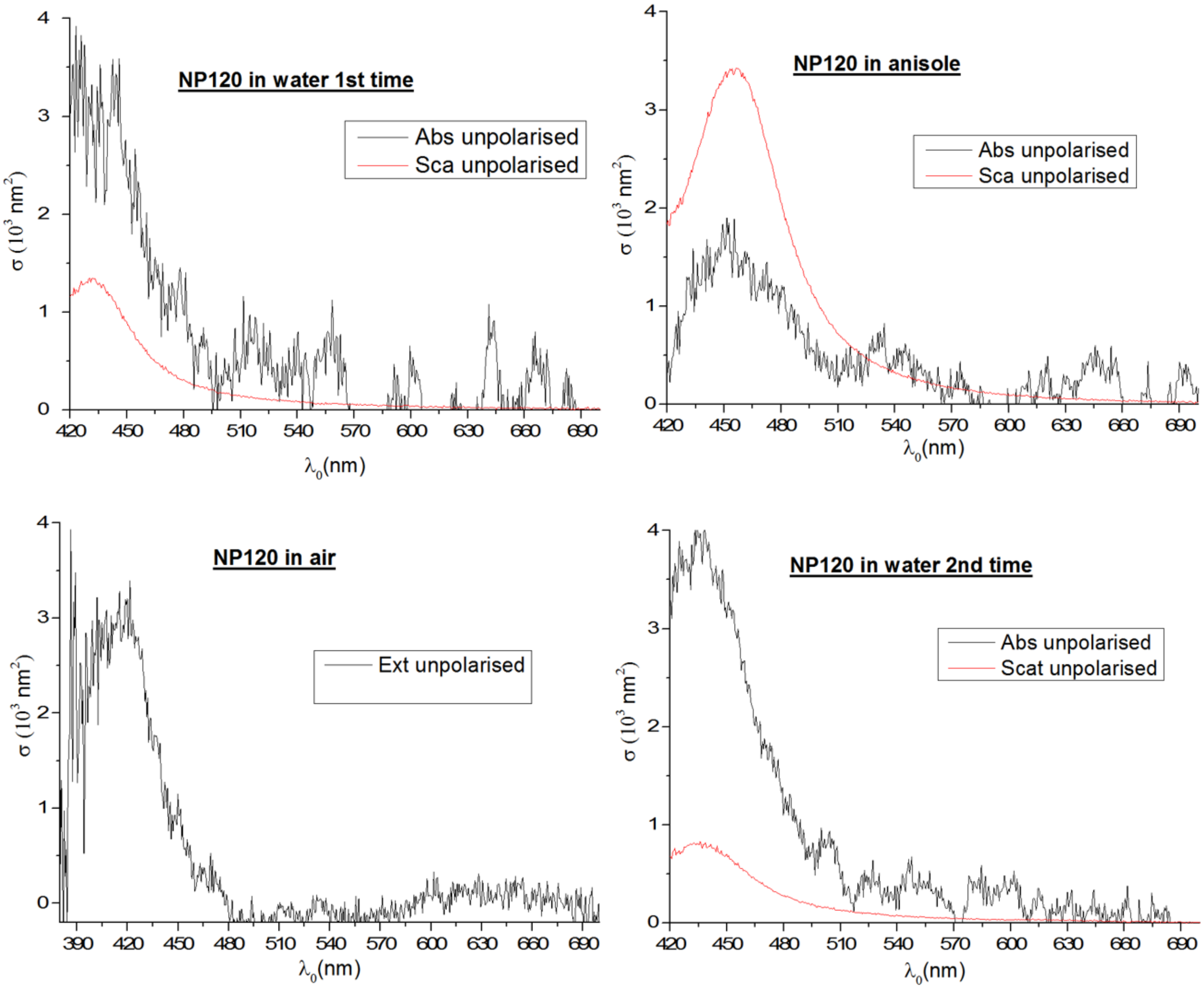

Figure 6.22 On the sample coverslip, a single NP scattering with blue colour without strong polarisation response was identified on the DF image in step 1. Microspectroscopy data of this NP are plotted, as indicated. They were collected in different experimental steps as shown in **Figure 6.19**. The spectra were calculated according to **Section 2.3.2**. The parameters for the calculation were ξ =4.42, f_{BF} = 0.137, f_{DF} = 0.116 and ζ = 4.42 (for spherical NPs).

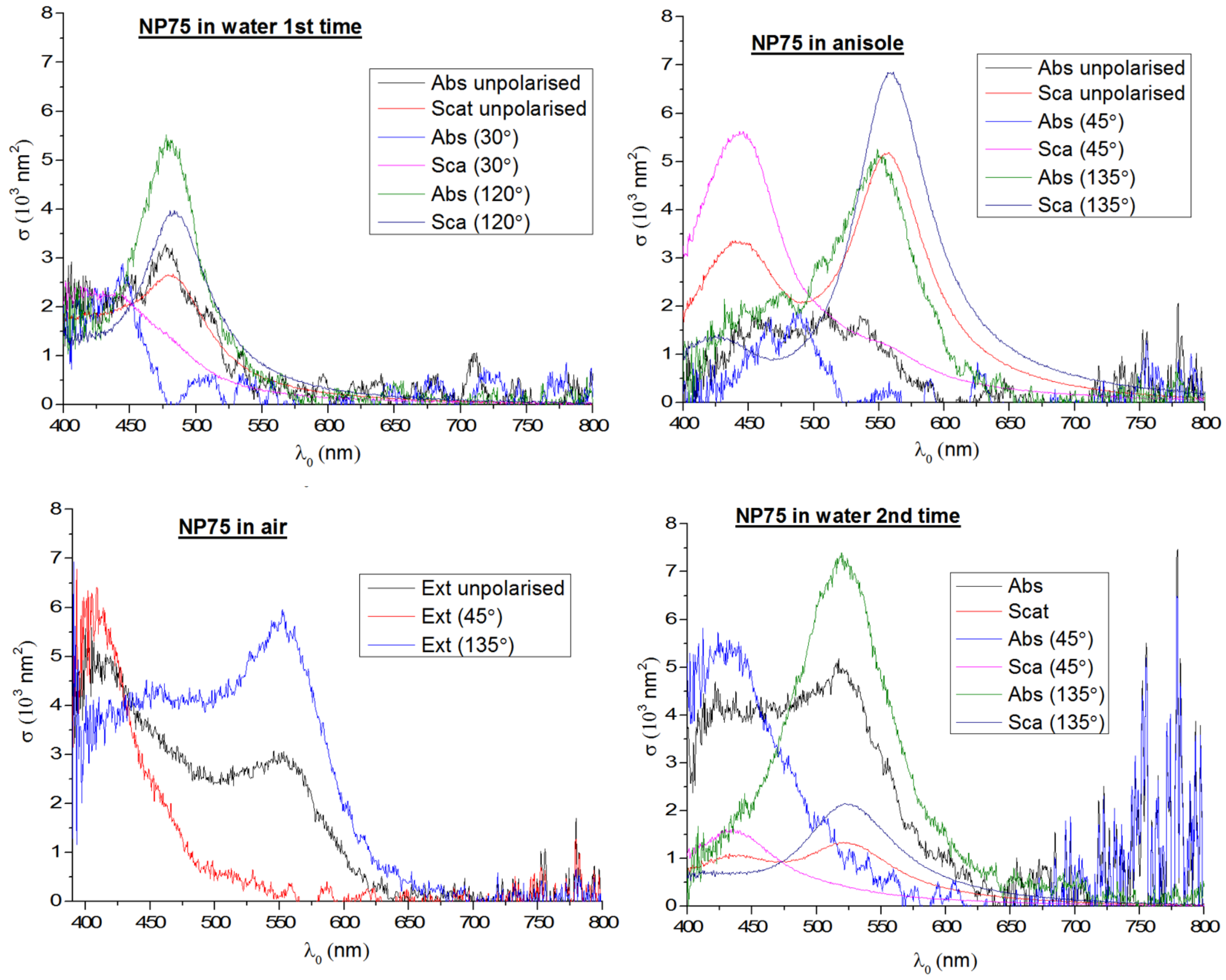

Figure 6.23. On the sample coverslip, a NP scattering with bright green colour and with strong polarisation response was identified on the DF image in step 1. Polarisation resolved microspectroscopy data of this NP are plotted as indicated. They were collected in different experimental steps as shown in **figure 6.19**. The spectra were calculated according to **Section 2.3.2**. The parameters for the calculation were: $\xi = 4.42$, $f_{BF} = 0.148$, $f_{DF} = 0.148$, $\zeta = 5.63$ for AgNP dimers.

A possible explanation for these observations is related to the behaviour of the polymer P1000DT in different media. PEG molecules, in general, are known to have 'infinite' solubility in water thanks to the large number of ethylene glycol units on the backbone (–CH_2–CH_2–O–). The nonbonding electron pairs on the oxygen atoms of the ether group allow each unit to form hydrogen bonding with a range of molecules. NMR studies and dynamic stimulations (Lusse and Arnold 1996. Tasaki 1996) show that, in aqueous solution, PEG (15 ethylene oxide units) molecules prefers trans-gauche-trans over all trans conformation, which allows one water molecule to form a hydrogen bonding bridge between two adjacent ether groups on the backbone of the PEG, and the whole PEG molecule prefers a helix structure. An extended network of PEG-water and water-water hydrogen bonds were found inside the helix that enhances the stability of the secondary structure. PEG with a longer chain will start to coil up. In a good solvent such as water, each PEG molecule forms expanded coils; the size of coil is measured as Flory radius, which can be calculated knowing its size (a) and number of the ethylene oxide unit (N) (Elbert and Hubbell 1996. Polymer Handbook 1966):

$$R_F = aN^{3/5} \qquad (\mathbf{6.1})$$

P1000DT has N=21 and each ethylene oxide unit has size a = 0.35 nm, therefore, P1000DT has R_F = 2.17 nm in aqueous solutions. The morphology of the grafted PEG molecules on the surface of AgNPs also depends on the PEG grafting density (Su *et al*. 1997). At lower grafting density, when the distance (D) between grafting terminals of the PEG chain is larger than the Flory radius of the polymer ($D > R_F$), the surface polymers will be predominantly in their mushroom conformations, so the coating of the AgNP is relatively thin with its thickness close to R_F. On the other hand, at higher grafting density ($D < R_F$), the surface polymers will be predominantly in their brush conformations, and the coating thickness is greater than $2{*}R_F$ (4.34 nm for P1000DT) (Damodaran *et al*. 2010). In our reaction solution, 420 μL of 40 nm AgNP with OD_{400nm} = 0.2, should contain 0.45 x 10^{10} particles/mL, which have 2.3 x 10^{13} nm^2 total surface area. 0.4 mM P1000DT in 420 μL should contain 10.12 x 10^{16} P1000DT molecules, thus, there were plenty of polymers in solution to fully cover the AgNP surface with maximum possible density. It is well known that thiol has high affinity toward silver and gold surfaces, and each P1000DT has 2 thiol groups. Furthermore, the polymers were adsorbed onto the surface of AgNPs soon after mixing (see the small red shift in the spectra of the reaction solution in **Figure 6.3**). Therefore, the grafted P1000DT is very likely to have $R_f > D$, and the polymers should adopt the brush conformation with the coating thickness (L) larger than $2{*}R_F$ (4.34 nm) and up to the contour length of 7.35 nm (see Table 6.5). This determines the possible range of interparticle distances in aqueous solution, and is consistent with the fact that the spectrum of a dimer in water had a relatively small $\Delta\lambda_{water}$ (**Figure 6.23**). This predicted range is also consistent with the observations reported in the literature: as described in Chapter 1, the ''plasmon ruler equation'' (**eq 1.6**) in (Yang *et al*. 2010) is a reasonable fitting of their measured spectroscopy data. According to this equation, the dimer with fractional shift $\Delta\lambda_{water}/\lambda_{monomer}$= 0.089 (**Figure 6.23**) should have an interparticle distance of about 8 nm.

Conversely, PEG molecules have very limited solubility in anisole. In a poor solvent, PEG molecules form collapsed coils, which have a reduced Flory radius (Elbert and Hubbell 1996. Polymer Handbook 1966):

$$R'_F = aN^{1/3} \qquad (\mathbf{6.2})$$

P1000DT has $R'_F = 0.98$ nm in anisole, which explains the TEM data in **Figure 6.16**, where the average gap size from all the dimers with small gap-size is about 1.4 nm. The small number of dimers with larger gaps found on the TEM micrograph might not be linked by P1000DT, but the result of monomers being close to each other randomly during the immobilisation steps. On the other hand, the conformational change of the grafted polymer in different media alone might not be sufficient to explain our results, especially considering that we observed irreversible changes. We believe that the shortening of interparticle distance was initiated during evaporation of water on the grid after step 1 (**Figure 6.19**), as we always observed a large number of NPs scattering in the red/yellow colour on the DF images when dimer samples were prepared after drying (data not showed). This is because the PEG coated NPs are immobilised on an APTES functionalised surface via a network of hydrogen bonding (**Scheme 6.8 C**) between the APTES on the substrate and the expanded PEG backbones, which were easily disrupted during evaporation. As the hydrogen bonds in the dry area started to break, new hydrogen bonds started to form in the wet area. The AgNP-P1000DT dimers only have a few nanometre gap-size (< 7.35 nm), and the PEG molecules in general have high affinity toward to water molecules, therefore, the water droplets were likely to be trapped around each dimers in the later stage of complete evaporation. Thereby the capillary action accompanied with the shifting hydrogen bonding network was able to pull the NPs closer to each other. After drying, the position of the NPs was stable on the grid when the NPs were imaged in different media as well as under the electron beam. The interaction between the NPs and the substrate in anisole and air might have changed from water mediated hydrogen network to a more stable, water free, hydrogen bonding between the ether groups of P1000DT and the amine group of APTES (**Scheme 6.8D**) as well as a strong amine-Ag bonding (the coating was reduced to about 1 nm). Notably, **Figure 6.23** shows that after the drying in step 1, $\Delta\lambda$ of the same dimer in each media were different ($\Delta\lambda_{air} > \Delta\lambda_{anisole} > \Delta\lambda_{water}$), which might at first suggest that the gap size of the dimer is different in each media. However, the ''plasmon ruler equation'' is insufficient for dimers with small gap-size: when the interparticle distance decreases below 2 nm, the λ_{long} does not further red-shift, instead, it becomes broadly distributed (Yang *et al*. 2010). Moreover, the effects of the surrounding environment on $\Delta\lambda$ of a dimer immobilised onto a surface have not yet been studied in the literature. Therefore, we need to confirm experimentally whether the gap-size of a dimer after immobilisation on the surface in our samples is stable or not in anisole and air. One simple way for such test will be to carry out the experiment in **figure 6.19** and repeat the step 2 and 3 for a number of times and compare the spectra of the dimer in each repeat; Δλ should be the same if the gap-size is stable. Work is also ongoing to simulate the experimental spectra, for example in Fig 6.16, with numerical models taking into account the dimer geometry from the TEM images. These simulations might confirm if the gap distances observed in air in TEM are indeed consistent with those deduced from the measured spectra in anisole.

As concluding remark, the spectroscopy results for the AgNP dimers in the reaction solution (**Figure 6.2 and 6.6**) have shown the potential to use PxDT for fabricating dimers with various gap size in aqueous solutions. However, since HR-TEM strictly require dried sample, our methodology described above is not suitable for fabricating dimers with large gap-size for correlative studies. From the discussion above, we believe this is mainly because the drying procedure irreversibly disrupts the NPs-substrate interaction and shortens the gap size. A possible solution is to immobilise NPs with stronger bonding. (Yang *et al*. 2010) functionalised the substrate with BSA-Biotin, and the NPs with Neutravidin. TEM images showed that the NPs position and gap-size were unchanged before and after optical measurements. To achieve that in our case, the amine group on APTES can be conjugated with the thiol group on P1000DT via succinimidyl trans-4-(maleimidylmethyl) cyclohexane -1 - carboxylate (SMCC).

A numerical simulation (FEM method) with COMSOL is currently being developed in the group (Dr Attilio Zilli and Dr. Samir Vartabi Kashanian) to better understand the correlative data obtained and the optical properties of the AgNP dimers.

Conclusion

The focus of this thesis was to investigate the optical properties of individual metallic nanoparticles of non-trivial shape (i.e. beyond quasi-spherical), which in turn have the potential to be exploited in innovative bioimaging and biosensing platforms. A significant effort was devoted both to fabricate novel particles, as well as to develop a quantitative correlative optical/TEM imaging method to study individual nanoparticles, for an in-depth understanding of how the morphology of a nanoparticle affects its optical properties.

In this thesis Ag bipyramids, tetrahedra, bi-tetrahedra, decahedra were fabricated by plasmon mediated photochemistry (Chapter 5), as well as Ag nanodimers from monomers using polymer mediated self-assembly (Chapter 6). For quantitative optical micro-spectroscopy, a method developed in our lab (Dr. Zilli PhD thesis and his unpublished work) was implemented which allows to measure the absolute optical cross-sections (absorption and scattering) of individual NPs on a solid substrate (Chapter 2). A correlative optical/TEM imaging method was developed for investigating the optical properties of AgNPs with different shapes and structure (Chapter 3), including commercially-available Ag-cubes (Chapter 4), as well as the in-house fabricated AgNPs of various shapes mentioned above. Importantly, the developed correlative imaging technique allow to directly compare the quantitative experimental measurements with EM simulations of the optical properties of AgNPs of a given shape/size using numerical modelling tools.

The NP settlement technique (**Section 3.1.3**) is essential for our correlative work. It not only produces a “clean” sample (without concentrating solutes onto the NP and substrate) but also evenly distributes NPs onto a glass substrate with surface density control. It has been demonstrated here that polymer-coated (PEG or PVP molecules) or sodium citrate coated AgNPs were immobilised onto APTES functionalised substrate via amine mediated hydrogen bonding (**Scheme 6.8**). This NP-substrate interaction was capable holding AgNPs in position after repetitive mounting of the sample in different media (both polar and non-polar solvents) and TEM imaging with large angle tilting (± 50°). Primary amine is one of the most commonly used functional groups in organic chemistry and biochemistry due to its reactivity in aqueous solution; this provides the possibilities of chemical modification of the substrate surface for different samples requirements. Amine group itself also have strong affinity toward gold and silver surfaces (Kumar *et al*. 2003. Poblete *et al*. 2017). Furthermore, various organosilicon compounds such as (3-Mercaptopropyl) trimethoxysilane are commercially available, which can be easily incorporated into our substrate modification protocol to suit different samples.

As shown in this thesis, the optical properties of MNPs can be significantly affected by TEM (**Figure 1.2** and **Figure 6.18**), thus for correlative studies the optical measurements should always be carried out before TEM, and the exposure during TEM should be minimised to image an unaltered NP shape. In this work, It has been proven that anisole is an excellent mounting medium for this purpose: it is chemical inert to silver, it is miscible with commonly used organic solvent (allows phase transfer) and it evaporates completely in a short time. Furthermore, anisole has a refractive index close to that of glass and silicon oil, meaning that the optical cross section of NP can be measured in an index-matched environment. Moreover, our sample mounting technique allows us to carry out optical measurements of the same sample in various media and, in turn, to study the NP response to different dielectric environments.

As proof of concept, the correlative optical/TEM studies were carried out on commercially available Ag-nanocubes. By combining our sample mounting techniques with our quantitative microspectroscopy data analysis, there were good agreements between the measured spectra and spectra calculated through numerical simulations (with COMSOL) using the size/shape information from TEM data of the same NP.

A plasmon mediated photochemistry method were developed, which was used to fabricate AgNPs with different shapes and sizes. TEM micrographs showed that the purified product solution from irradiation with a 447 nm LED contains Ag tetrahedra (14 %), bi-tetrahedra (6%), decahedra (75%) and irregular shapes (8%) with different sizes. Because our focus is on single NP studies, the polydispersity of the product solution came to our advantage, and correlative studies of those various AgNPs on the same sample grid was carried out. The experimental data here show how the size and edge rounding of the decahedra and bi-tetrahedra affect their LSPR peak position and amplitudes. The next steps in this work will be to use our wide field extinction analysis (Payne *et al*. 2018) to study the crystal evolution pathways during irradiation. The ensemble statistics from wide field extinction will allow us to track how the optical properties of the various seeds population change with irradiation time. This type of kinetics studies on a solid phase are possible, thanks to the settlement technique (clear sample and short preparation time). Combined with our quantitative micro-spectroscopy and correlative imaging methods, these future experiments will enable us to elucidate complex kinetic problems in colloid chemistry.

Polymer linkers (PxDT) were used to fabricate dimers with various interparticle distances. It was demonstrated that the linkers are able to induce self-assembly of AgNPs in aqueous solution, and this reaction can be quenched via a thiol capping agent. By using low concentration of AgNP (in pM) and high concentration of polymer linker (mM), the self-assembly process can be slowed down. Thanks to the short preparation time of the NP settlement techniques (5 to 10 mins), a large number of dimers in the reaction solution during the early stage of the self-assembly process were immobilised onto the substrate. The UV-Vis spectroscopy data of the reaction solution showed that the interparticle distance of the dimers can be controlled by using polymer linkers with different contour lengths. However, ensemble statistical wide field extinction analysis of samples settled on the substrate from different stages of our dimer preparation protocol showed that the interparticle distances of the dimers shortened irreversibly following a drying step. This was further corroborated by quantitative micro-spectroscopy of the same nanoparticle under different media, where the medium exchange involved a drying step. We believe, this is mainly due to the fact that the small (<8nm) interparticle gaps (filled with soft and hydrophilic polymers) are good sites for trapping water during the later stage of the evaporation. Therefore, the hydrogen bonding are disrupted unevenly as the water on the outer surface of the dimer dries out before doing so in the gap; this helps the capillary action to pull both AgNPs toward to the gap centre. Further chemical modification of the substrate and the AgNP surfaces are required to overcome the capillary action, which will be investigated in future studies.

Overall we believe this work has laid the foundation toward fabricating and charactering novel Ag nanoparticles with a much better understanding of the link between their morphology and optical properties, which could be a great use for future applications of these nanoparticles as novel optical bio-labels and/or bio-sensors.

Reference

Ajayan PM, Marks LD (1988) Quasimelting and Phases of Small Particles. Phys Rev Lett 60 (7):585-587. doi:DOI 10.1103/PhysRevLett.60.585

Ambjornsson T, Mukhopadhyay G, Apell SP, Kall M (2006) Resonant coupling between localized plasmons and anisotropic molecular coatings in ellipsoidal metal nanoparticles. Phys Rev B 73 (8). doi:ARTN 085412 10.1103/PhysRevB.73.085412

Baletto F, Ferrando R (2005) Structural properties of nanoclusters: Energetic, thermodynamic, and kinetic effects. Rev Mod Phys 77 (1):371-423. doi:DOI 10.1103/RevModPhys.77.371

Burda C, Chen X, Narayanan R, El-Sayed MA (2005) Chemistry and properties of nanocrystals of different shapes. Chemical reviews 105 (4):1025-1102. doi:10.1021/cr030063a

Corbierre MK, Beerens J, Lennox RB (2005) Gold nanoparticles generated by electron beam lithography of gold(I)-thiolate thin films. Chem Mater 17 (23):5774-5779. doi:10.1021/cm051085b

Cypryk M, Apeloig Y (2002) Mechanism of the acid-catalyzed Si-O bond cleavage in siloxanes and siloxanols. A theoretical study. Organometallics 21 (11):2165-2175. doi:10.1021/om011055s

Damodaran VB, Fee CJ, Ruckh T, Popat KC (2010) Conformational studies of covalently grafted poly(ethylene glycol) on modified solid matrices using X-ray photoelectron spectroscopy. Langmuir 26 (10):7299-7306. doi:10.1021/la9041502

Davletshin YR, Lombardi A, Cardinal MF, Juve V, Crut A, Maioli P, Liz-Marzan LM, Vallee F, Del Fatti N, Kumaradas JC (2012) A quantitative study of the environmental effects on the optical response of gold nanorods. Acs Nano 6 (9):8183-8193. doi:10.1021/nn302869v

Dienerowitz M, Mazilu M, Dholakia K (2008) Optical manipulation of nanoparticles: a review. J Nanophotonics 2. doi:Artn 021875 10.1117/1.2992045

Draine BT, Flatau PJ (1994) Discrete-Dipole Approximation for Scattering Calculations. J Opt Soc Am A 11 (4):1491-1499. doi:Doi 10.1364/Josaa.11.001491

El-Sayed MA (2001) Some interesting properties of metals confined in time and nanometer space of different shapes. Accounts Chem Res 34 (4):257-264. doi:10.1021/ar960016n

Elbert DL, Hubbell JA (1996) Surface treatments of polymers for biocompatibility. Annu Rev Mater Sci 26:365-394. doi:DOI 10.1146/annurev.ms.26.080196.002053

Fayet P, Granzer F, Hegenbart G, Moisar E, Pischel B, Woste L (1985) Latent-Image Generation by Deposition of Monodisperse Silver Clusters. Phys Rev Lett 55 (27):3002-3004. doi:DOI 10.1103/PhysRevLett.55.3002

Fuchs R (1975) Theory of the optical properties of ionic crystal cubes. Phys Rev B 11:1732

Gao Y, Hassanbhai AM, Lim J, Wang LH, Xu CJ (2017) Fabrication of a silver octahedral nanoparticle-containing polycaprolactone nanocomposite for antibacterial bone scaffolds. Rsc Adv 7 (17):10051-10056. doi:10.1039/c6ra26063b

Gao Y, Jiang P, Song L, Wang JX, Liu LF, Liu DF, Xiang YJ, Zhang ZX, Zhao XW, Dou XY, Luo SD, Zhou WY, Xie SS (2006) Studies on silver nanodecahedrons synthesized by PVP-assisted N,N-dimethylformamide (DMF) reduction. J Cryst Growth 289 (1):376-380. doi:10.1016/j.jcrysgro.2005.11.123

Genzel L, Martin TP, Kreibig U (1975) Dielectric Function and Plasma Resonances of Small Metal Particles. Z Phys B Con Mat 21 (4):339-346. doi:Doi 10.1007/Bf01325393

Ghosh SK, Nath S, Kundu S, Esumi K, Pal T (2004) Solvent and ligand effects on the localized surface plasmon resonance (LSPR) of gold colloids. J Phys Chem B 108 (37):13963-13971. doi:10.1021/jp047021q

Gonzalez AL, Noguez C, Beranek J, Barnard AS (2014) Size, Shape, Stability, and Color of Plasmonic Silver Nanoparticles. Journal of Physical Chemistry C 118 (17):9128-9136

Griffiths DJ, Owen RE (1983) Mass Renormalisation in Classical Electrodynamics. Am J Phys 51 (12):1120-1126. doi:Doi 10.1119/1.13349

Grillet N, Manchon D, Bertorelle F, Bonnet C, Broyer M, Cottancin E, Lerme J, Hillenkamp M, Pellarin M (2011) Plasmon Coupling in Silver Nanocube Dimers: Resonance Splitting Induced by Edge Rounding. Acs Nano 5 (12):9450-9462. doi:10.1021/nn2041329

Gunnarsson L, Rindzevicius T, Prikulis J, Kasemo B, Kall M, Zou SL, Schatz GC (2005) Confined plasmons in nanofabricated single silver particle pairs: Experimental observations of strong interparticle interactions. J Phys Chem B 109 (3):1079-1087. doi:10.1021/jp049084e

Haes AJ, Haynes CL, McFarland AD, Schatz GC, Van Duyne RR, Zou SL (2005) Plasmonic materials for surface-enhanced sensing and spectroscopy. Mrs Bull 30 (5):368-375. doi:DOI 10.1557/mrs2005.100

Hornstein BJ, Finke RG (2004) Transition-metal nanocluster kinetic and mechanistic studies emphasizing nanocluster agglomeration: Demonstration of a kinetic method that allows monitoring of all three phases of nanocluster formation and aging (vol 16, pg 139, 2004). Chem Mater 16 (20):3972-3972. doi:10.1021/cm0400637

Jain PK, Huang WY, El-Sayed MA (2007) On the universal scaling behaviour of the distance decay of plasmon coupling in metal nanoparticle pairs: A plasmon ruler equation. Nano Lett 7 (7):2080-2088. doi:10.1021/nl071008a

Jin J (2002) The finite element method in electromagnetics. A Wiley-Interscience publication, 2. edn. Wiley, New York

Jin J-M (2014) The Finite Element Method in Electromagnetics. Wiley-IEEE Press 1 (3rd edition)

Jin RC, Cao YC, Hao EC, Metraux GS, Schatz GC, Mirkin CA (2003) Controlling anisotropic nanoparticle growth through plasmon excitation. Nature 425 (6957):487-490. doi:10.1038/nature02020

Jin RC, Cao YW, Mirkin CA, Kelly KL, Schatz GC, Zheng JG (2001) Photoinduced conversion of silver nanospheres to nanoprisms. Science 294 (5548):1901-1903. doi:DOI 10.1126/science.1066541

Jin RC, Jureller JE, Kim HY, Scherer NF (2005) Correlating second harmonic optical responses of single Ag nanoparticles with morphology. J Am Chem Soc 127 (36):12482-12483. doi:10.1021/ja0537169

Kobayashi Y, Katakami H, Mine E, Nagao D, Konno M, Liz-Marzan LM (2005) Silica coating of silver nanoparticles using a modified Stober method. J Colloid Interf Sci 283 (2):392-396. doi:10.1016/j.jcis.2004.08.184

Konig TAF, Ledin PA, Kerszulis J, Mahmoud MA, El-Sayed MA, Reynolds JR, Tsukruk VV (2014) Electrically Tunable Plasmonic Behaviour of Nanocube-Polymer Nanomaterials Induced by a Redox-Active Electrochromic Polymer. Acs Nano 8 (6):6182-6192. doi:10.1021/nn501601e

Kostrewa D, Winkler FK (1995) Mg2+ Binding to the Active-Site of Ecorv Endonuclease - a Crystallographic Study of Complexes with Substrate and Product DNA at 2-Angstrom Resolution. Biochemistry-Us 34 (2):683-696. doi:DOI 10.1021/bi00002a036

Kottmann JP, Martin OJF, Smith DR, Schultz S (2001) Plasmon resonances of silver nanowires with a nonregular cross section. Phys Rev B 64 (23). doi:ARTN 235402. 10.1103/PhysRevB.64.235402

Kreibig U, Vollmer M (1995) Optical properties of metal clusters. Springer series in materials science, vol 25. Springer, Berlin; New York

Kumar A, Mandal S, Selvakannan PR, Pasricha R, Mandale AB, Sastry M (2003) Investigation into the interaction between surface-bound alkylamines and gold nanoparticles. Langmuir 19 (15):6277-6282. doi:10.1021/la034209c

Laczik Z (1996) Discrete-dipole-approximation-based light-scattering calculations for particles with a real refractive index smaller than unity. Appl Opt 35 (19):3736-3745. doi:10.1364/AO.35.003736

Langille MR, Personick ML, Mirkin CA (2013) Plasmon-Mediated Syntheses of Metallic Nanostructures. Angew Chem Int Edit 52 (52):13910-13940. doi:10.1002/anie.201301875

Langille MR, Zhang J, Personick ML, Li SY, Mirkin CA (2012) Stepwise Evolution of Spherical Seeds into 20-Fold Twinned Icosahedra. Science 337 (6097):954-957. doi:10.1126/science.1225653

Lindfors K, Kalkbrenner T, Stoller P, Sandoghdar V (2004) Detection and spectroscopy of gold nanoparticles using supercontinuum white light confocal microscopy. Phys Rev Lett 93 (3). doi:ARTN 037401
10.1103/PhysRevLett.93.037401

Lombardi A, Loumaigne M, Crut A, Maioli P, Del Fatti N, Vallee F, Spuch-Calvar M, Burgin J, Majimel J, Treguer-Delapierre M (2012) Surface Plasmon Resonance Properties of Single Elongated Nanoobjects: Gold Nanobipyramids and Nanorods. Langmuir 28 (24):9027-9033. doi:10.1021/la300210h

Lusse S, Arnold K (1996) The interaction of poly(ethylene glycol) with water studied by H-1 and H-2 NMR relaxation time measurements. Macromolecules 29 (12):4251-4257. doi:DOI 10.1021/ma9508616

Marques ME, Mansur AAP, Mansur HS (2013) Chemical functionalisation of surfaces for building three-dimensional engineered biosensors. Appl Surf Sci 275:347-360. doi:10.1016/j.apsusc.2012.12.099

McEachran M, Kitaev V (2008) Direct structural transformation of silver platelets into right bipyramids and twinned cube nanoparticles: morphology governed by defects. Chem Commun (44):5737-5739. doi:10.1039/b813519c

Michen B, Geers C, Vanhecke D, Endes C, Rothen-Rutishauser B, Balog S, Petri-Fink A (2015) Avoiding drying-artifacts in transmission electron microscopy: Characterizing the size and colloidal state of nanoparticles. Sci Rep 5:9793. doi:10.1038/srep09793

The MIE theory (2012). Springer, New York

Murphy DB, Davidson MW (2013) Fundamentals of light microscopy and electronic imaging. 2nd edn. Wiley-Blackwell, Hoboken, N.J.

Nehl CL, Grady NK, Goodrich GP, Tam F, Halas NJ, Hafner JH (2004) Scattering spectra of single gold nanoshells. Nano Lett 4 (12):2355-2359. doi:10.1021/nl048610a

Nordlander P, Oubre C, Prodan E, Li K, Stockman MI (2004) Plasmon hybridizaton in nanoparticle dimers. Nano Lett 4 (5):899-903. doi:10.1021/nl049681c

Ortega-Arroyo J, Kukura P (2012) Interferometric scattering microscopy (iSCAT): new frontiers in ultrafast and ultrasensitive optical microscopy. Phys Chem Chem Phys 14 (45):15625-15636. doi:10.1039/c2cp41013c

Payne L, Zoriniants G, Masia F, Arkill KP, Verkade P, Rowles D, Langbein W, Borri P (2015) Optical micro-spectroscopy of single metallic nanoparticles: quantitative extinction and transient resonant four-wave mixing. Faraday Discuss 184:305-320. doi:10.1039/c5fd00079c

Payne LM, Langbein W, Borri P (2013) Polarisation-resolved extinction and scattering cross-sections of individual gold nanoparticles measured by wide-field microscopy on a large ensemble. Appl Phys Lett 102 (13). doi:Artn 131107 10.1063/1.4800564

Payne LM, Langbein W, Borri P (2018) Wide-Field Imaging of Single-Nanoparticle Extinction with Sub-nm(2) Sensitivity. Phys Rev Appl 9 (3). doi:ARTN 034006 10.1103/PhysRevApplied.9.034006

Petryayeva E, Krull UJ (2011) Localized surface plasmon resonance: Nanostructures, bioassays and biosensing-A review. Anal Chim Acta 706 (1):8-24. doi:10.1016/j.aca.2011.08.020

Pietrobon B, Kitaev V (2008) Photochemical Synthesis of Monodisperse Size-Controlled Silver Decahedral Nanoparticles and Their Remarkable Optical Properties. Chem Mater 20 (16):5186-5190. doi:10.1021/cm800926u

Poblete H, Agarwal A, Thomas SS, Bohne C, Ravichandran R, Phospase J, Comer J, Alarcon EI (2016) New Insights into Peptide-Silver Nanoparticle Interaction: Deciphering the Role of Cysteine and Lysine in the Peptide Sequence. Langmuir 32 (1):265-273. doi:10.1021/acs.langmuir.5b03601

Polymer Handbook (1966). Rubber Age 98 (6):147-&

Pyatenko A, Yamaguchi M, Suzuki M (2007) Synthesis of spherical silver nanoparticles with controllable sizes in aqueous solutions. J Phys Chem C 111 (22):7910-7917. doi:10.1021/jp071080x

Quinten M (2001) Local fields close to the surface of nanoparticles and aggregates of nanoparticles. Appl Phys B-Lasers O 73 (3):245-255. doi:DOI 10.1007/s003400100650

Reinhard BM, Sheikholeslami S, Mastroianni A, Alivisatos AP, Liphardt J (2007) Use of plasmon coupling to reveal the dynamics of DNA bending and cleavage by single EcoRV restriction enzymes. P Natl Acad Sci USA 104 (8):2667-2672. doi:10.1073/pnas.0607826104

Reinhard BM, Siu M, Agarwal H, Alivisatos AP, Liphardt J (2005) Calibration of dynamic molecular rulers based on plasmon coupling between gold nanoparticles. Nano Lett 5 (11):2246-2252. doi:10.1021/nl051592s

Reichardt C, (2003) Solvents and Solvent Effects in Organic Chemistry, Wiley-VCH Publishers, 3rd ed., Rocha TCR, Winnischofer H, Westphal E, Zanchet D (2007) Formation kinetics of silver triangular nanoplates. J Phys Chem C 111 (7):2885-2891. doi:10.1021/jp0660637

Rong GX, Wang HY, Reinhard BM (2010) Insights from a Nanoparticle Minuet: Two-Dimensional Membrane Profiling through Silver Plasmon Ruler Tracking. Nano Lett 10 (1):230-238. doi:10.1021/nl903350f

Sanchez-Iglesias A, Pastoriza-Santos I, Perez-Juste J, Rodriguez-Gonzalez B, de Abajo FJG, Liz-Marzan LM (2006) Synthesis and optical properties of gold nanodecahedra with size control. Adv Mater 18 (19):2529-+. doi:10.1002/adma.200600475

Seo D, Park JC, Song H (2006) Polyhedral gold nanocrystals with O-h symmetry: From octahedra to cubes. J Am Chem Soc 128 (46):14863-14870. doi:10.1021/ja062892u

Sharma VK, Siskova KM, Zboril R, Gardea-Torresdey JL (2014) Organic-coated silver nanoparticles in biological and environmental conditions: fate, stability and toxicity. Adv Colloid Interface Sci 204:15-34. doi:10.1016/j.cis.2013.12.002

Sherry LJ, Chang SH, Schatz GC, Van Duyne RP, Wiley BJ, Xia YN (2005) Localized surface plasmon resonance spectroscopy of single silver nanocubes. Nano Lett 5 (10):2034-2038. doi:10.1021/nl0515753

Slaughter L, Chang WS, Link S (2011) Characterizing Plasmons in Nanoparticles and Their Assemblies with Single Particle Spectroscopy. J Phys Chem Lett 2 (16):2015-2023. doi:10.1021/jz200702m

Song YJ, Zhang ZS, Elsayed-Ali HE, Wang HN, Henry LL, Wang QQ, Zou SL, Zhang T (2011) Identification of single nanoparticles. Nanoscale 3 (1):31-44. doi:10.1039/c0nr00412j

Sonnichsen C, Alivisatos AP (2005) Gold nanorods as novel nonbleaching plasmon-based orientation sensors for polarised single-particle microscopy. Nano Lett 5 (2):301-304. doi:10.1021/nl048089k

Sonnichsen C, Reinhard BM, Liphardt J, Alivisatos AP (2005) A molecular ruler based on plasmon coupling of single gold and silver nanoparticles. Nat Biotechnol 23 (6):741-745. doi:10.1038/nbt1100

Stewart ME, Anderton CR, Thompson LB, Maria J, Gray SK, Rogers JA, Nuzzo RG (2008) Nanostructured plasmonic sensors. Chem Rev 108 (2):494-521. doi:10.1021/cr068126n

Su ZH, Wu DC, Hsu SL, McCarthy TJ (1997) Adsorption of end-functionalised poly(ethylene oxide)s to the poly(ethylene oxide)-air interface. Macromolecules 30 (4):840-845. doi:DOI 10.1021/ma961396v

Sun YG, Xia YN (2002) Shape-controlled synthesis of gold and silver nanoparticles. Science 298 (5601):2176-2179. doi:DOI 10.1126/science.1077229

Swarnavalli GCJ, Joseph V, Kannappan V, Roopsingh D (2011) A Simple Approach to the Synthesis of Hexagonal-Shaped Silver Nanoplates. J Nanomater. doi:Artn 825637 10.1155/2011/825637

Taflove A, Hagness SC (2005) Computational electrodynamics : the finite-difference time-domain method. Artech House antennas and propagation library, 3rd edn. Artech House, Boston

Tang B, Xu SP, Hou XL, Li JH, Sun L, Xu WQ, Wang XG (2013) Shape Evolution of Silver Nanoplates through Heating and Photoinduction. Acs Appl Mater Inter 5 (3):646-653. doi:10.1021/am302072u

van Dijk MA, Tchebotareva AL, Orrit M, Lippitz M, Berciaud S, Lasne D, Cognet L, Lounis B (2006) Absorption and scattering microscopy of single metal nanoparticles. Phys Chem Chem Phys 8 (30):3486-3495. doi:10.1039/b606090k

Washio I, Xiong YJ, Yin YD, Xia YN (2006) Reduction by the end groups of poly(vinyl pyrrolidone): A new and versatile route to the kinetically controlled synthesis of Ag triangular nanoplates. Adv Mater 18 (13):1745-+. doi:10.1002/adma.200600675

Willets KA, Van Duyne RP (2007) Localized surface plasmon resonance spectroscopy and sensing. Annual Review of Physical Chemistry 58:267-297

Wiley B, Herricks T, Sun YG, Xia YN (2004) Polyol synthesis of silver nanoparticles: Use of chloride and oxygen to promote the formation of single-crystal, truncated cubes and tetrahedrons (vol 4, pg 1734, 2004). Nano Lett 4 (10):2057-2057

Wiley BJ, Chen YC, McLellan JM, Xiong YJ, Li ZY, Ginger D, Xia YN (2007) Synthesis and optical properties of silver nanobars and nanorice. Nano Lett 7 (4):1032-1036. doi:10.1021/nl070214f

Wiley BJ, Im SH, Li ZY, McLellan J, Siekkinen A, Xia YN (2006a) Maneuvering the surface plasmon resonance of silver nanostructures through shape-controlled synthesis. J Phys Chem B 110 (32):15666-15675. doi:10.1021/jp0608628

Wiley BJ, Xiong YJ, Li ZY, Yin YD, Xia YN (2006b) Right bipyramids of silver: A new shape derived from single twinned seeds. Nano Lett 6 (4):765-768. doi:10.1021/nl060069q

Xia XH, Xie SF, Liu MC, Peng HC, Lu N, Wang JG, Kim MJ, Xia YN (2013) On the role of surface diffusion in determining the shape or morphology of noble-metal nanocrystals. P Natl Acad Sci USA 110 (17):6669-6673. doi:10.1073/pnas.1222109110

Xia YN, Xiong YJ, Lim B, Skrabalak SE (2009) Shape-Controlled Synthesis of Metal Nanocrystals: Simple Chemistry Meets Complex Physics? Angew Chem Int Edit 48 (1):60-103. doi:10.1002/anie.200802248

Xiong Y, Washio I, Chen J, Sadilek M, Xia YN (2007a) Trimeric clusters of silver in aqueous AgNO3 solutions and their role as nuclei in forming triangular nanoplates of silver. Angew Chem Int Edit 46 (26):4917-4921. doi:10.1002/anie.200700942

Xiong YJ, Siekkinen AR, Wang JG, Yin YD, Kim MJ, Xia YN (2007b) Synthesis of silver nanoplates at high yields by slowing down the polyol reduction of silver nitrate with polyacrylamide. J Mater Chem 17 (25):2600-2602. doi:10.1039/b705253g

Xue C, Metraux GS, Millstone JE, Mirkin CA (2008) Mechanistic study of photomediated triangular silver nanoprism growth. J Am Chem Soc 130 (26):8337-8344. doi:10.1021/ja8005258

Yang L, Yan B, Reinhard BM (2008) Correlated Optical Spectroscopy and Transmission Electron Microscopy of Individual Hollow Nanoparticles and their Dimers. J Phys Chem C Nanomater Interfaces 112 (41):15989-15996. doi:10.1021/jp804790p

Yang LL, Wang HY, Yan B, Reinhard BM (2010) Calibration of Silver Plasmon Rulers in the 1-25 nm Separation Range: Experimental Indications of Distinct

Plasmon Coupling Regimes. J Phys Chem C 114 (11):4901-4908. doi:10.1021/jp911858v

Yang WH, Schatz GC, Vanduyne RP (1995) Discrete Dipole Approximation for Calculating Extinction and Raman Intensities for Small Particles with Arbitrary Shapes. J Chem Phys 103 (3):869-875. doi:Doi 10.1063/1.469787

Ye S, Song J, Tian YL, Chen LC, Wang D, Niu HB, Qu JL (2015) Photochemically grown silver nanodecahedra with precise tuning of plasmonic resonance. Nanoscale 7 (29):12706-12712. doi:10.1039/c5nr03652f

Yguerabide J, Yguerabide EE (1998) Light-scattering submicroscopic particles as highly fluorescent analogs and their use as tracer labels in clinical and biological applications - II. Experimental characterisation. Anal Biochem 262 (2):157-176. doi:DOI 10.1006/abio.1998.2760

Zeng J, Zheng YQ, Rycenga M, Tao J, Li ZY, Zhang QA, Zhu YM, Xia YN (2010) Controlling the Shapes of Silver Nanocrystals with Different Capping Agents. J Am Chem Soc 132 (25):8552-+. doi:10.1021/ja103655f

Zhang J, Li SZ, Wu JS, Schatz GC, Mirkin CA (2009) Plasmon-Mediated Synthesis of Silver Triangular Bipyramids. Angew Chem Int Edit 48 (42):7787-7791. doi:10.1002/anie.200903380

Zhang JA, Langille MR, Mirkin CA (2010) Photomediated Synthesis of Silver Triangular Bipyramids and Prisms: The Effect of pH and BSPP. J Am Chem Soc 132 (35):12502-12510. doi:10.1021/ja106008b

Zheng XL, Xu WQ, Corredor C, Xu SP, An J, Zhao B, Lombardi JR (2007) Laser-induced growth of monodisperse silver nanoparticles with tunable surface plasmon resonance properties and a wavelength self-limiting effect. J Phys Chem C 111 (41):14962-14967. doi:10.1021/jp074583b

Zheng XL, Zhao XJ, Guo DW, Tang B, Xu SP, Zhao B, Xu WQ, Lombardi JR (2009) Photochemical Formation of Silver Nanodecahedra: Structural Selection by the Excitation Wavelength. Langmuir 25 (6):3802-3807. doi:10.1021/la803814j

Zhou F, Li ZY, Liu Y, Xia YN (2008a) Quantitative Analysis of Dipole and Quadrupole Excitation in the Surface Plasmon Resonance of Metal Nanoparticles. J Phys Chem C 112 (51):20233-20240. doi:10.1021/jp807075f

Zhou J, An J, Tang B, Xu SP, Cao YX, Zhao B, Xu WQ, Chang JJ, Lombardi JR (2008b) Growth of tetrahedral silver nanocrystals in aqueous solution and their SERS enhancement. Langmuir 24 (18):10407-10413. doi:10.1021/la800961j

Zhu MJ, Lerum MZ, Chen W (2012) How To Prepare Reproducible, Homogeneous, and Hydrolytically Stable Aminosilane-Derived Layers on Silica. Langmuir 28 (1):416-423. doi:10.1021/la203638g

Zuloaga J, Prodan E, Nordlander P (2009) Quantum Description of the Plasmon Resonances of a Nanoparticle Dimer. Nano Lett 9 (2):887-891. doi:10.1021/nl803811g